



UNIVERSITAT^{DE}
BARCELONA

GHz Magnetization Dynamics in X-ray PhotoEmission Electron Microscopy (XPEEM)

Muhammad Waqas Khaliq



Aquesta tesi doctoral està subjecta a la llicència **Reconeixement 4.0. Espanya de Creative Commons.**

Esta tesis doctoral está sujeta a la licencia **Reconocimiento 4.0. España de Creative Commons.**

This doctoral thesis is licensed under the **Creative Commons Attribution 4.0. Spain License.**

Tesi doctoral

**GHz Magnetization Dynamics in X-ray
PhotoEmission Electron Microscopy
(XPEEM)**

Muhammad Waqas Khaliq

Dr. Michael Foerster

Dr. Ferran Macià



**UNIVERSITAT DE
BARCELONA**

GHz Magnetization Dynamics in X-ray PhotoEmission Electron Microscopy (XPEEM)

Programa de doctorat en
Física

Autor: Muhammad Waqas Khaliq

Directors: Dr. Michael Foerster &
Dr. Ferran Macià

Tutor: Prof. Giancarlo Franzese

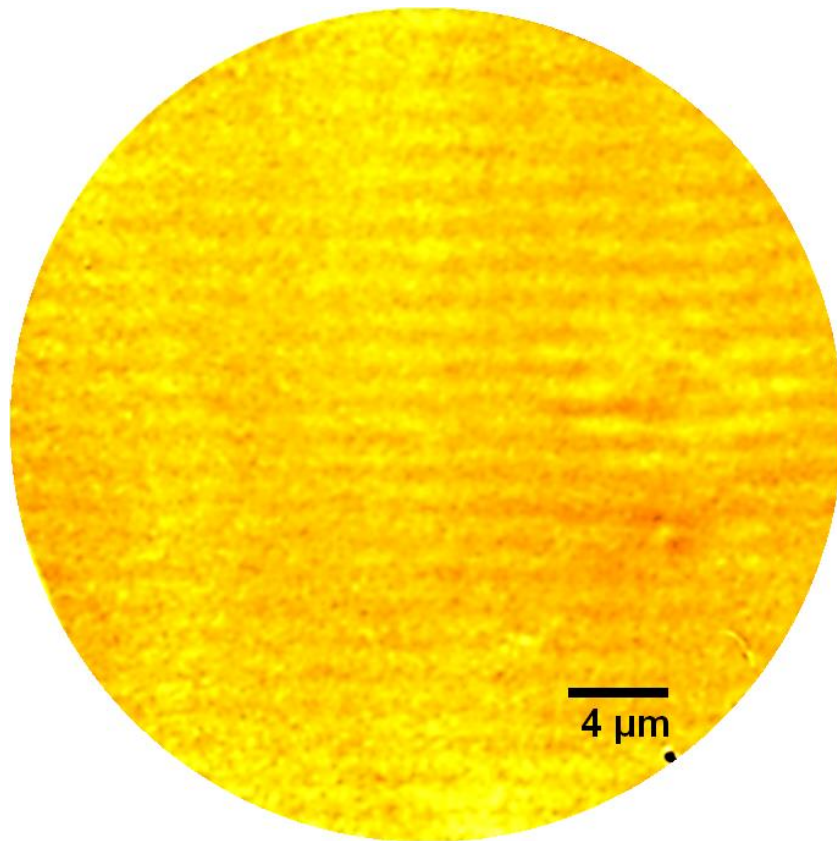


UNIVERSITAT DE
BARCELONA

PhD Thesis

GHz MAGNETIZATION DYNAMICS IN X-RAY
PHOTOEMISSION ELECTRON MICROSCOPY
(XPEEM)

Muhammad Waqas Khaliq



Magnetoacoustic Waves in Ni at 3 GHz



UNIVERSITAT DE
BARCELONA

CONTENTS

Dedication	iv
Acknowledgements	v
Summary	viii
Resum en Català	xi
Chapter 1	1
1 Introduction	2
1.1 Aims and Structure of this Dissertation	2
Chapter 2	4
2 General Concepts of Magnetism	5
2.1 Magnetic Moment	5
2.2 Ferromagnetism	6
2.3 Antiferromagnetism	7
2.4 Energies Related to Magnetism	9
2.4.1 Zeeman Energy	9
2.4.2 Exchange Energy	9

2.4.3	Magnetostatic (Dipolar) Energy	10
2.4.4	Magneto-Crystalline Anisotropy	10
2.5	Magnetic Configurations	11
2.5.1	Pinning of Domain Walls	13
2.6	Magnetization Dynamics	14
2.6.1	Magnetization Dynamics around the Field	14
2.6.2	Magnetoelastic Interactions	16
Chapter 3		19
3 X-ray PhotoEmission Electron Microscope (XPEEM)		20
3.1	Synchrotron and Synchrotron Radiation	21
3.1.1	Properties of Synchrotron Radiations	24
3.2	Photoemitted Electrons	27
3.3	X-ray Photoemission Electron Microscope (XPEEM)	28
3.3.1	Instrumentation	30
3.3.1.1	Principle of Operation	30
3.3.1.2	Lateral Resolution	31
3.3.2	Multi-Technique Surface Characterization in a LEEM- PEEM Instrument	32
3.3.2.1	XPEEM	33
3.3.2.2	X-ray Absorption Spectroscopy (XAS) with PEEM	33
3.3.2.3	XMCD and XMLD with PEEM	33
3.3.2.4	X-ray Photoemission Spectroscopy (XPS)	34
3.4	XPEEM Facility at the CIRCE Beamline – ALBA Synchrotron	35
3.4.1	The Experimental Station Layout and Microscope	36
3.4.2	Sample Holders at the CIRCE-PEEM	38
3.4.3	Sample Holders for GHz Frequencies	39
3.4.4	In-/Out-of-Plane Vector Magnet Sample Holder	40
Chapter 4		42
4 Magnetization Dynamics Driven by Surface Acoustic Waves (SAW)		43

4.1	Magnetization Dynamics	44
4.2	Magnetization Dynamics by SAW	45
4.2.1	Surface Acoustic Waves (SAWs)	45
4.2.2	Magnetization Dynamics by SAWs – State of the Art	47
4.3	Experiments with SAW in XPEEM	49
4.3.1	Excitation of SAW by IDTS	49
4.3.2	Sample Holder and Mounting	51
4.3.3	Synchronizing Electrical Excitations with X-rays	53
4.3.4	SAW Contrast and Amplitude in XPEEM	55
Chapter 5		57
5 Summary of Results		58
Chapter 6		69
6 Articles		70
6.1	Néel vector waves in antiferromagnetic CuMnAs excited by Surface Acoustic Waves	71
6.2	GHz sample excitation at the ALBA-PEEM	84
6.3	Study of the magnetoelastic effect in nickel and cobalt thin films at GHz range using X-ray microscopy	92
Chapter 7		102
Conclusions and Future Perspectives		103
Bibliography		106
List of Articles		124
List of Figures		127
List of Symbols and Abbreviations		129

DEDICATION

*My Late Parents,
Encouraging Advisors,
and Beloved Family*

ACKNOWLEDGEMENTS

I extend my earnest appreciation to all those people and organizations who contributed and supported me in accomplishing this effortful task of the PhD.

I would like to record my sincere thanks to the DOC-FAM that has received funding from the European Union's Horizon 2020 research and innovation program under the Marie Skłodowska-Curie grant agreement No. 754397, and the Spanish Ministry for funding from the MCIN through grant No. PID2021-1229800B-C54. Also, I am really indebted to the Alba Synchrotron Light Facility that provided me such a wonderful opportunity to pursue and develop my expertise in the field of Synchrotron science and condensed matter physics. I am also grateful to the University of Barcelona (UB) for accepting me as a PhD student and using the facilities available there.

My deepest and special gratitude to my principal advisor **Dr. Michael Foerster**, the beamline scientist at the Alba, for his invaluable advices, guidance, encouragement, and criticism during the course of this entire work, more like a friend than an advisor. I remember when I started my PhD, everything seemed to be impossible since my former experiences were not aligned with the upcoming studies. Whenever I had a problem in understanding anything,

despite of being occupied in beamtimes, he explained it to me in a very polite and elaborative way until I understand it. His guidance was not limited to science but to almost every field of life that helped me in developing my personality and shaping myself into what I am now. Our discussions have been always like a discussion among friends. His optimistic approach helped me in carrying out the experiments and activities in a confident manner.

My extreme appreciations to my co-supervisor **Dr. Ferran Macià**, professor at the UB, for his immense support in directing the thesis, improving my scientific concepts in the relevant field, and extraordinary guidance related with the administrative activities of the university. Regardless of his engagements in teaching and other activities at the university, he has always been available for the meetings. After having discussions with him, everything seemed to be resolved in an easy manner, which helped me a lot in keeping my nerves in control.

I would like to thank **Dr. Lucia Aballe**, interdisciplinary & multimodal responsible, and **Dr. Miguel Angel Niño**, beamline responsible, for their technical guidance and support towards operation of the microscope during absence of Dr. Michael. With Dr. Miguel, I never felt him as a colleague but more as a friend with whom I explored the city of Barcelona and had funny conversations over breakfast. Assistance of **Mr. Antonio Camps** and the electronics team of the Alba who stood up and tried to fix all the relevant issues at their earliest during the course of my thesis is greatly acknowledged. I would like to thank **Mr. Jordi Prat**, technician at the Alba, who helped me in developing my technical expertise and introduced me to the things which I cannot imagine to be done without his guidance and patience. I am grateful to **Dr. Sandra Ruiz-Gomez**, postdoctoral researcher, for the fun time we spent at the beamline as Batman and Robin during the pandemic times.

Special thanks to **Dr. Oliver Amin**, **Dr. Richard Campion**, **Dr. Kevin Edmonds**, and **Dr. Peter Wadley** from University of Nottingham and **Dr. Vít Novák** from Institute of Physics, Prague for providing the sample of antiferromagnetic CuMnAs. Also, **Dr. Alberto Hernández-Mínguez** and **Mr. Nicole Volkmer** from

Paul Drude Institute for depositing the IDTs on the samples. Their activities played core-level roles in conducting the presented studies successfully.

Sincere thanks to **Mr. Marc Rovirola**, PhD student at the UB, for his assistance to perform simulations and FMR measurements of the samples and beneficial discussions, as well as **Mr. Travis Gustafson**, PhD student at the NTNU, Trondheim, for his support during the beamtime. Also, I thank **Dr. Joan Manel Hernández**, assistant professor at the UB, for his support during the beamtimes and playing the music instruments in the laboratory, where I also discovered my skills of playing funny music.

Sincere appreciations to **Ms. Sílvia Boquer**, Secretary of the Faculty of Physics, whose immense guidance and kind behavior made the process of thesis submission very helpful and efficient. Last but not the least, I would like to pay my deepest and profound gratitude to my loving family whose emotional and constant support and prayers helped me a lot in achieving my goals.

SUMMARY

This thesis presents the recent results achieved during my Ph.D. This is a research project in the field of condensed matter physics, under the supervision of Dr. Michael Foerster of the ALBA Synchrotron and Dr. Ferran Macià from the University of Barcelona, during November 2020 to February 2024. This thesis is based on a collection of articles combined with an overview and a discussion.

In general, magnetic systems which are influenced by different energy factors, realize a final state that tries to minimize the total energy. This can produce diverse magnetic patterns that deviate from uniform alignment. Observing and controlling the evolution of magnetization is vital for the development of fast devices and often requires operations on sub-nanosecond time scales. The main objective of this thesis is to generate and observe magnetization dynamics at the micro/nano scale in different systems of thin magnetic layers from acoustic waves. This approach represents a low-energy method compared to other conventional approaches to induce dynamics in magnetic systems. X-ray photoemission electron microscopy (XPEEM) is used to observe the dynamics of magnetic systems under the effect of acoustic waves.

This work is structured in seven chapters. The first chapter consists of a brief introduction and the objectives of the thesis. Chapter 2 provides the general introduction into the field of magnetism that provides details on the origin of magnetism in a particular material. There are various energies present in magnetic materials, either intrinsic or extrinsic, that adjust the ground state of the material. The global magnetic behavior is governed by the balance between these energies, giving rise to various magnetic configurations in the system.

In the third chapter, knowledge about the synchrotron and synchrotron light is presented along with the different sections of the synchrotron that lead to the generation of X-rays. PEEM uses these X-rays to obtain images of the magnetic behavior of materials. This mechanism is discussed below, which includes the instrumentation of the PEEM configuration and the factors that affect its spatial resolution. Various characterization techniques can be performed using XPEEM, such as XAS, XMCD, XMLD, XPS, etc. to determine the occupation states in magnetic systems. In addition, since the thesis was mainly carried out in the Alba synchrotron light facility, several attributes related to this installation are also presented.

Chapter four discusses the importance of tuning magnetization in materials to improve their properties for various applications. It explores different methods to understand and optimize magnetization dynamics within materials. The chapter is divided into three parts. First, it provides an overview of the state of the art and the underlying physics of magnetization dynamics. Second, it analyzes the role of surface acoustic waves (SAW) in the manipulation of magnetization dynamics, including the most relevant studies. Finally, the experimental setup required to combine SAW generation in magnetic devices together with XPEEM imaging is explored, with the aim of observing and analyzing the magnetization dynamics, and how the magnetization is coupled to acoustic waves.

In the fifth chapter, a detailed summary of all the articles included in this thesis is presented, followed by the sixth chapter which includes all the articles. Among these papers, one has been published in the journal *Ultramicroscopy* and the other two have already been submitted and are under review in *Phys. Rev. Lett.* and *Phys. Rev. Research*. We have observed that the strain due to SAW induces magnetization dynamics in both ferromagnetic and antiferromagnetic systems and both systems exhibit comparable efficiency. We designed and built a high frequency connection for the XPEEM microscope system that allows studying excitations at higher frequencies (>1 GHz) and used it to study magneto-acoustic waves (combination of magnetic waves and acoustic waves) in ferromagnetic systems such as Ni and Co and to determine their magnetoelastic coupling in this regime.

Finally, the conclusions are summarized and the perspectives are added in the seventh chapter. This thesis presents a new approach to generate magnetoacoustic waves in magnetic thin layers based on the magnetoelastic interaction. On the one hand in antiferromagnetic materials, offering potential applications in data storage and on the other in ferromagnetic materials, where we observe the weakening of waves at frequencies above 1 GHz; suggesting that more work is needed to address this. Striking variations in wave amplitudes at specific frequencies in different ferromagnetic systems suggest diverse interactions between magnetization waves and acoustic waves. In addition, the new system designed for the XPEEM microscope at the ALBA offers opportunities to make measurements with time resolution, such as studies of magnetization dynamics, domain walls and skyrmion motion using ultra-short current pulses. These pathways promise to develop new nanomagnetic devices for future data storage applications, emphasizing the importance of continued exploration in both fundamental and technological areas.

RESUM EN CATALÀ

Aquesta tesi presenta els resultats recents realitzats durant el meu doctorat. Es tracta d'un treball de recerca en el camp de la física de la matèria condensada, sota la supervisió del Dr. Michael Foerster del Sincrotró ALBA i el Dr. Ferran Macià de la Universitat de Barcelona, durant el novembre de 2020 al febrer de 2024. Aquesta tesi es basa en una col·lecció d'articles combinat amb una visió general i una discussió.

En els sistemes magnètics, influenciats per diferents factors energètics, tenen un estat final que intenta minimitzar l'energia total. Això pot produir patrons magnètics diversos que disten d'una alineació uniforme. L'observació i el control de l'evolució de la magnetització és vital pel desenvolupament de dispositius ràpids i sovint requereix operacions a escales de temps inferiors al nanosegon. L'objectiu principal d'aquesta tesi és generar i observar dinàmiques de magnetització a la micro/nano escala en diferents sistemes de capes fines magnètiques a partir de ones acústiques. Aquest enfocament representa un mètode de baix consum d'energia en comparació amb altres enfocaments convencionals per induir la dinàmica en sistemes magnètics. S'utilitza la

microscopia electrònica de fotoemissió de raigs X (XPEEM) per observar la dinàmica i dels sistemes magnètics sota l'efecte de les ones acústiques.

Aquest treball s'estructura en set capítols. El primer capítol consta d'una breu introducció i dels objectius de la tesi. El capítol 2 ofereix la introducció general dins del camp del magnetisme que proporciona els detalls sobre l'origen del magnetisme en un material concret. Hi ha diverses energies presents als materials magnètics, ja siguin intrínseques o extrínseques, que ajusten l'estat fonamental del material. El comportament magnètic global es regeix per l'equilibri entre aquestes energies, donant lloc a diverses configuracions magnètiques en el sistema.

En el tercer capítol, es presenten coneixements sobre el sincrotró i la llum de sincrotró juntament amb les diferents seccions del sincrotró que condueixen a la generació de raigs X. PEEM utilitza aquests raigs X per obtenir imatges del comportament magnètic dels materials. Aquest mecanisme es discuteix més endavant, que inclou la instrumentació de la configuració del PEEM i els factors que afecten la seva resolució espacial. Es poden realitzar diverses tècniques de caracterització mitjançant XPEEM, com ara XAS, XMCD, XMLD, XPS, etc. per determinar els estats d'ocupació en els sistemes magnètics. A més, com que la tesi s'ha realitzat principalment a la instal·lació de Llum del Sincrotró Alba, també es presenten diversos atributs relacionats amb aquesta instal·lació.

El capítol quatre analitza la importància d'ajustar la magnetització en materials per millorar les seves propietats per a diverses aplicacions. Explora diferents mètodes per comprendre i optimitzar la dinàmica de magnetització dins dels materials. El capítol està dividit en tres parts. En primer lloc, ofereix una visió general de l'estat de l'art i la física subjacent de la dinàmica de magnetització. En segon lloc, analitza el paper de les ones acústiques superficials (SAW) en la manipulació de la dinàmica de magnetització, incloent els estudis més rellevants. Finalment, s'aprofundeix en la configuració experimental necessària per combinar la generació SAW en dispositius

magnètics juntament amb la presa d'imatges XPEEM, amb l'objectiu d'observar i analitzar la dinàmica de magnetització, i com la magnetització s'acobla a amb les ones acústiques.

En el cinquè capítol, es presenta un resum detallat de tots els articles inclosos en aquesta tesi, seguit del sisè capítol que inclou tots els articles. Entre aquests articles, un s'ha publicat a la revista d'Ultramicroscopy i els altres dos ja s'han enviat i estan en procés de revisió a Phys. Rev. Lett. i Phys. Rev. Research. Hem observat que la tensió deguda a SAW indueix dinàmiques de magnetització tant en sistemes ferromagnètics com en sistemes antiferromagnètics i ambdós sistemes presenten una eficiència comparable. Hem dissenyat i construït un sistema al microscopi XPEEM que permet estudiar excitacions a més altes freqüències ($>1\text{GHz}$) i ho hem utilitzat per estudiar les ones magnetoacústiques (combinació d'ones magnètiques i ones acústiques) en sistemes ferromagnètics com Ni i Co i de per determinar-ne l'acoblament magnetoelàstic.

Finalment, es resumeixen les conclusions i s'afegeixen les perspectives en el setè capítol. Aquesta tesi presenta un nou enfocament per generar ones magnetoacústiques en capes primes magnètiques a partir de la interacció magnetoelàstica. Per una banda en materials antiferromagnets, oferint aplicacions potencials en l'emmagatzematge de dades i per l'altra en materials ferromagnets, on observem el debilitament de les ones a freqüències per sobre de 1 GHz; fet que suggereix que més investigacions són necessàries. Les variacions sorprenents en les amplituds de les ones a freqüències específiques en diferents sistemes ferromagnètics suggereixen interaccions diverses entre les ones de magnetització i les ones acústiques. A més, el nou sistema dissenyat per al microscopi XPEEM a ALBA ofereix oportunitats per fer mesures amb resolució temporal, com són els estudis sobre la dinàmica de magnetització, les parets de domini i el moviment del skyrmions mitjançant polsos de corrent ultra curts. Aquestes vies prometen desenvolupar nous dispositius nanomagnètics per a futures aplicacions d'emmagatzematge de dades, posant èmfasi en la

importància de l'exploració continuada tant en els àmbits fonamentals com en els tecnològics.

CHAPTER 1

Chapter 1

INTRODUCTION

For many applications in the realm of telecommunications and information technology, like data storage, it is imperative to utilize magnetic materials that are as diminutive as possible. This downsizing enables enhanced storage capacity, reduced energy consumption, and reduced production costs (for emerging technologies). As novel materials and more compact devices are manufactured, they give rise to new phenomena, necessitating a fresh understanding of the underlying physics. The scale at which these emerging magnetic materials operate, typically on the order of nanometers, serves as the interface between the microcosmic quantum realm and the macroscopic classical world—known as the mesoscale. Magnetic thin films with nanoscale thicknesses represent mesoscopic systems that can be integrated into magnetic multilayers, patterns and 3D structures, with emerging novel properties. Although not limited to this area, nanomagnetic devices are mostly used in data storage applications like hard disk drives, (readout) sensors and magnetic random-access memory (MRAM).

1.1 Aims and Structure of this Dissertation

The configuration of a magnetic system is determined by the interplay or competition of various energy terms within the system. These systems naturally

progress towards a final state, which can either be dynamic or static, with the goal of minimizing the total energy. This can lead to the emergence of magnetic patterns distinct from the uniform state where all spins align in the same direction. The ability to manage the evolution of magnetization is a crucial process in the advancement of faster devices and technologies, often necessitating to work at timescales on the order of sub-nanoseconds. In this dissertation, I developed a new setup to investigate a novel method for controlling the magnetization through the dynamic application of strain as a surface acoustic wave (SAW) in ferro- and antiferromagnets. The setup is based on an X-ray PhotoEmission Electron Microscope (XPEEM) to which the capability of exciting the sample with GHz frequency signals has been added.

After the present introduction in [Chapter 1](#), the relevant basic principles of magnetism are elaborated in detail in the following [Chapter 2](#). [Chapter 3](#) is dedicated to explaining the experimental technique of the XPEEM. Exploring the synchrotron details, offer an understanding of how synchrotron radiation (X-rays) is generated and its inherent properties. This is followed by the operation principles of PEEM and the type of information which is obtained using different modes like e.g., XMCD. [Chapter 4](#) describes in more detail the field of magnetization dynamics, driven by time dependent fields, electrical currents and surface acoustic waves (SAW). This is followed by an explanation of the stroboscopic imaging of SAW in the XPEEM, including the synchronization scheme and the contrast formation based on the surface electrical potential oscillation. The following section is designated to providing a summary of the outcomes ([Chapter 5](#)), and a compilation of the main publications ([Chapter 6](#)). Ultimately, the conclusions are presented in [Chapter 7](#), along with the provision of insights regarding future prospects.

CHAPTER 2

Chapter 2

GENERAL CONCEPTS OF MAGNETISM

Magnetism, an enduring force of nature, has been a catalyst for a wide range of transformative technologies that shape our contemporary lives. This phenomenon originates from the intrinsic magnetic attributes of electrons within materials, influencing their behavior across various scales. At its core, magnetism is intricately tied to the alignment and motion of magnetic moments, which are predominantly borne by electrons. Magnetic materials, harnessed in a myriad of applications, have revolutionized modern technology, from the magnetic memories in our digital devices to the sensors that propel our automobiles and aircraft. The pervasive influence of magnetism on modern society is indisputable. Within the context of this chapter, we delve into the fundamental concepts of magnetism, with a particular focus on magnetic configurations and dynamics in nanoscale materials.

2.1 Magnetic Moment

Magnetic moment is a quantity which determines the torque exerted by magnetic field on a magnetic material. All of the following, loop of electric current, bar magnet, and electron possess magnetic moments. These magnetic moments interact in various ways, leading to the net magnetic moment of a body.

The magnetic moment in electrons arises due to two microscopic contributions: orbital motion, $\boldsymbol{\mu}_l = \gamma_e \hbar \mathbf{l}$ and spin, $\boldsymbol{\mu}_s = g_e \gamma_e \hbar \mathbf{s}$, where $\gamma_e = e/2m_e$ is gyromagnetic factor, e and m_e the charge and mass of an electron, respectively, $g_e \approx 2$ corresponds to electron spin- g -factor, l being the orbital momentum and s the spin quantum number. The overall electron moment is represented by $\mathbf{m} = \mathbf{l} + 2\mathbf{s}$. In an atom where many electrons interact, one can consider the overall spin moment \mathbf{S} and overall angular momentum \mathbf{L} giving to a quantity $\mathbf{J} = \mathbf{L} + \mathbf{S}$, that is again proportional to the overall atom or ion magnetic moment. These magnetic moments can interact with each other, leading to various magnetic ordering behaviors. The net magnetic moment of the material, often denoted as \mathbf{M} , results from the sum of the individual magnetic moments and its interactions [1].

The overall magnetic moment \mathbf{M} in a material is a spatially varying vector quantity which depends on the arrangement of atomic or molecular magnetic moments. It is expressed as $\mathbf{M}(\mathbf{r})$ and describes how magnetic properties change throughout the material. This is particularly crucial when studying ferromagnetic, antiferromagnetic, or ferrimagnetic materials with complex magnetic ordering. In summary, the classical magnetic moment $\mathbf{M}(\mathbf{r})$ accounts for all magnetic interactions in a material, portraying the overall magnetic behavior as a function of position.

2.2 Ferromagnetism

Ferromagnetism is a type of magnetism exhibited by certain materials, and it is characterized by the spontaneous alignment of atomic or molecular magnetic moments in the same direction, resulting in a strong and permanent magnetization. Ferromagnetic materials have a high magnetic susceptibility and can retain their magnetization even after the external magnetic field is removed. This property makes them particularly useful in various applications, including the manufacturing of permanent magnets and magnetic storage devices. The key characteristics of ferromagnetism include:

a) Spontaneous Alignment: In ferromagnetic materials, the magnetic moments of individual atoms or ions tend to align themselves in the same direction.

This alignment occurs without the need for an external magnetic field. It is the result of strong exchange interactions between neighboring magnetic moments.

- b) **Strong Magnetization:** Ferromagnetic materials can become strongly magnetized, producing a significant magnetic field. This property is responsible for their use in making permanent magnets, such as those found in refrigerator magnets and electric motors.
- c) **Hysteresis:** Ferromagnetic materials exhibit hysteresis, which means that their magnetization lags behind changes in the applied magnetic field. Even after the external field is removed, the material retains some of its magnetization, and it takes a certain level of demagnetizing field to reduce the magnetization to zero.
- d) **Curie Temperature:** Ferromagnetic materials have a critical temperature called the Curie temperature (T_c). Above this temperature, the material loses its ferromagnetic properties and becomes paramagnetic (magnetic moments are randomly oriented). Below the Curie temperature, it becomes ferromagnetic again.

Ferromagnetic materials are commonly used in the construction of transformers, electric motors, generators, and in particular in the data storage industry for making memory devices

2.3 Antiferromagnetism

Antiferromagnetism is a type of magnetic ordering exhibited by certain materials in which adjacent atomic or molecular magnetic moments align in opposite directions. In an antiferromagnetic material, the individual magnetic moments cancel each other out, resulting in a net zero magnetization. Antiferromagnetic materials are characterized by their unique magnetic properties, which are distinct from the behavior of ferromagnetic materials. The key characteristics of antiferromagnetism include:

- a) **Opposite Alignment:** In antiferromagnetic materials, neighboring atomic or molecular magnetic moments are aligned in opposite directions. This means

that for every magnetic moment pointing in one direction, there is an adjacent moment pointing in the opposite direction.

- b) **No Net Magnetization:** The opposing alignments of magnetic moments within the material result in a net magnetization of zero. Therefore, antiferromagnetic materials do not produce an external magnetic field.
- c) **No Hysteresis:** Unlike ferromagnetic materials, antiferromagnetic materials do not exhibit hysteresis in their magnetic properties. When an external magnetic field is applied, the atomic or molecular magnetic moments align with the field and then return to their original antiparallel alignment when the field is removed.
- d) **Néel Temperature:** Antiferromagnetic materials have a critical temperature called the Néel temperature (T_N), above which they lose their antiferromagnetic order and become paramagnetic. Below the Néel temperature, the antiferromagnetic order is maintained.

Antiferromagnetic materials are used in various scientific and technological applications, including research in condensed matter physics and the development of advanced magnetic materials for spintronics, which is a field of study focused on using the electron's spin for information processing and storage.

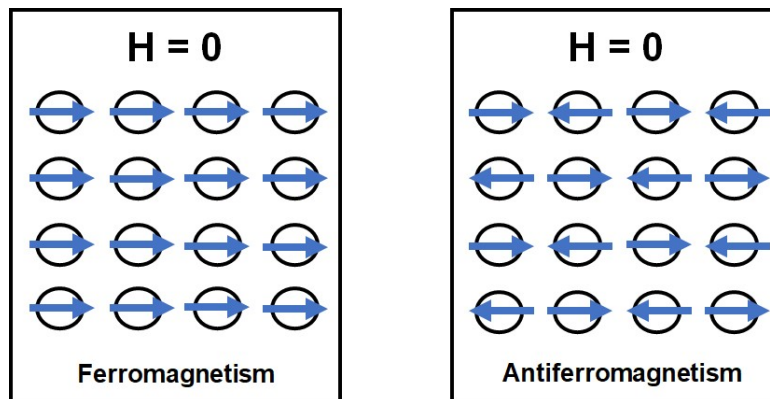


Figure 2.1. Schematic illustrating the arrangements of magnetic moments for ferromagnets and antiferromagnets materials in the absence of an external magnetic field.

2.4 Energies Related to Magnetism

There are various energies involved in magnetic systems. Most of the energies are intrinsic, whereas, some appear by other sources such as external magnetic field, different magnetic layers coupled, etc. The ground state of a magnetic system is governed by the balance between these energies. The following are the vital energies that determine the magnetic ground state of the system.

2.4.1 Zeeman Energy

This energy is associated with the application of magnetic field on the magnetic moment. Mathematically, it can be written as:

$$E = -\boldsymbol{\mu} \cdot \mathbf{B}_0. \quad (1)$$

The origin of the magnetic moment can be classical or quantum.

For the classical approximation,

$$E_{\text{Zeeman}} = -\mu_0 \int d^3r \mathbf{M}(\mathbf{r}) \cdot \mathbf{H}_0. \quad (2)$$

This equation depicts that when the magnetization and external field are parallel, the energy is minimum.

2.4.2 Exchange Energy

Exchange interaction is related to Pauli exclusion principle. When the unpaired outer valence electrons orbitals overlap, the parallel-spin state of electrons is more stable due to the reduction in electrostatic energy of these electron as compared to the energies when their spins are antiparallel. The difference between these two energies is known as exchange energy, given as:

$$E_{\text{ex}} = \sum_{n < m} J_{nm} \mathbf{s}_n \cdot \mathbf{s}_m.$$

In this equation, n and m denote the position, since the interaction is between spin \mathbf{s}_n and \mathbf{s}_m . J_{nm} is exchange constant that enumerates the energy variation between parallel and antiparallel orientation of electron spins. J_{nm} is positive in the case of ferromagnets and antiferromagnetic materials exhibit negative J_{nm} such that they possess minimum exchange energy when aligned antiparallel.

For an isotropic material, the common expression for exchange energy is given as:

$$E_{\text{ex}} = A_{\text{ex}} \int d^3r \nabla^2 \mathbf{M}, \quad (3)$$

in which $A_{\text{ex}} \left(= \frac{\mu_0 \alpha}{2} = \frac{2JS^2N}{a} \right)$ is exchange constant, N represents the number of sites in the unit cell, and a being the nearest neighboring distance, that corresponds to the cell size.

2.4.3 Magnetostatic (Dipolar) Energy

Spins, being considered as magnetic dipoles, interact via long range dipolar fields in a solid. Shape anisotropy, also known as magnetostatic energy or dipolar energy (E_d) is a type of Zeeman energy that occurs among all the moments within the magnetic entity due to their stray fields. In summary, the interaction between field and magnetization can be ascribed as the dipolar energy:

$$E_d = \frac{1}{2} \mu_0 \int d^3r \mathbf{M}(\mathbf{r}) \cdot \mathbf{H}_d(\mathbf{r}), \quad (4)$$

which is considered as Zeeman-related energy. This expression for dipole-dipole interaction energy quantifies how the magnetic moments of the dipoles align with each other and how the energy changes as the dipoles' separation distance and orientation with respect to each other change, giving rise to formation of magnetic domains in the case of ferromagnetic materials.

2.4.4 Magneto-crystalline Anisotropy Energy

Assuming zero Zeeman energy (no external magnetic field) in a magnet, the magnetization is refrained from any specific direction in the space. Nevertheless, the internal energy relies on the magnetization direction, in reality, with fundamental crystalline direction of the solids. This occurs due to the combined effect of crystal-field effects and spin-orbit effects. The former arises in response to the coupling of electron orbitals with the lattice and the

later as a result of orbital coupling with spin moments. This internal energy is termed as magneto-crystalline anisotropy energy, denoted as E_{MC} . Because of this energy, the magnetization tends to align along specific axis of the solid, referred as easy directions.

The energy, therefore, in classical approximation can be written as:

$$E_{MC} = -\frac{\mu_0}{2} \int d^3r \beta_{ij} \mathbf{M}_i \mathbf{M}_j, \quad (5)$$

where β_{ij} is the 2nd order anisotropy tensor. Under the uniaxial circumstance, the term along the easy axis for anisotropy is different from zero, therefore, the energy becomes:

$$E_{MC} = -\frac{\mu_0}{2} \beta \int d^3r (\mathbf{z} \cdot \mathbf{M})^2 = K_V \int d^3r \sin^2\theta(\mathbf{r}) + \text{constant}. \quad (6)$$

The K_V , anisotropy constant, represents the strength of anisotropy in terms of energy. The energy, in terms of field, can be written as:

$$E_{MC} = -\frac{\mu_0}{2} \int d^3r \mathbf{M}(\mathbf{r}) \cdot \mathbf{H}_K. \quad (7)$$

Magneto-crystalline anisotropy energy allows to control the magnetic properties of materials along specific crystallographic directions. Materials with high magneto-crystalline anisotropy energy can create energy barriers that prevent spontaneous changes in the orientation of their magnetic moments.

2.5 Magnetic Configurations

Due to the competition between exchange and dipolar energies in a magnetic material, a sample is broken into various regions possessing different magnetizations. These regions are called magnetic domains which are separated by boundaries or interfaces, referred as domain walls. The behavior of domain walls in a material is influenced by several factors, including anisotropy energy. The domain walls can form along crystallographic directions that are favorable in terms of anisotropy energy. The specific orientation and type of domain walls depend on the material's anisotropy energy landscape. In

a ferromagnetic material, this breaking down occurs in order to reduce the magnetostatic energy generated by dipolar field, depicted in Fig. 2.2.

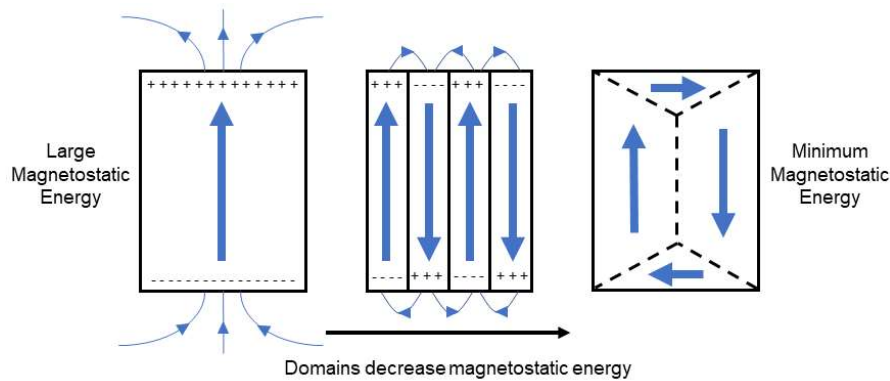


Figure 2.2. Breaking down of ferromagnetic material into magnetic domains. The extreme left state has the highest magnetostatic energy, however, introducing 180° domain walls minimizes the magnetostatic energy and increases the exchange energy (central). The extreme right with 90° closure domains raises the anisotropy energy.

The magnetic flux is confined within the magnetic material by the formation of magnetic domains that minimize the magnetostatic energy. Since the domain formation leads to the formation of domain walls where exists the magnetization rotation, these rotations can be of two types, namely Néel domain walls [2] and Bloch domain walls [3]. The former represents the rotation within the plane and the latter represents the rotation perpendicular to the plane. The difference among both is illustrated in the following figure.

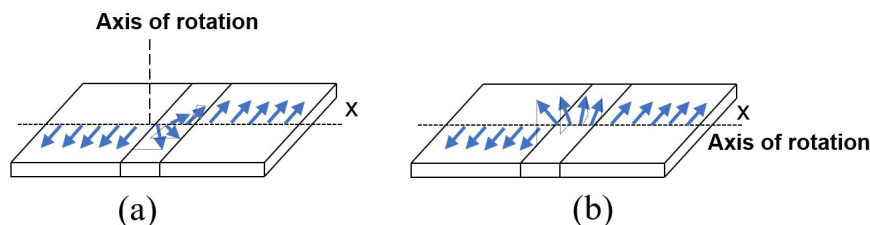


Figure 2.3. Configuration of domain walls with (a) in-plane magnetization (Néel wall) and (b) out-of-plane magnetization (Bloch wall).

The geometry of the magnetic material defines the domain structure, mainly due to exchange and magnetostatic energies, whereas, the width of domain wall is governed by the dominance among exchange and anisotropy energies. The energy barriers associated with moving a domain wall depend on the anisotropy energy landscape. Lower anisotropy energy barriers make it easier for domain walls to move, whereas higher energy barriers can inhibit their motion and pin domains.

2.5.1 Pinning of Domain Walls

Magnetization changes in magnetic materials take place due to two mechanisms, namely domain rotation and domain wall motion. Manifestation of domain wall motion can be in two ways: bowing of domain wall and translation. If the domain wall faces a pinning site, these both become irreversible. The possible types of pinning sites are illustrated below:

- a) Domain walls can pin due to magnetoelastic coupling (will be discussed in detail later) in response to strain that correspond to dislocations in the material. Thus, pinning will be stronger under the presence of higher density of dislocations, that will restrain the domain wall motion.
- b) There could exist different states in the material that behave magnetically different, i.e., non-magnetic or less magnetic in comparison to the nature of material as a whole. These inclusions reduce the magnetostatic energy of the domain walls at their interface with the magnetic material. Therefore, this energetically favorable region tends to pin the domain wall unless an external source is employed (higher magnetic field or current) to unpin it.

Domain wall pinning is caused by those defects mainly whose dimensions are in comparison with the size of domain wall thickness (tens of nanometers). In some magnetic materials, the grain boundaries and point defects play a critical role in pinning the domain walls due to their smaller widths. However, bigger precipitates and long-range strain fields are responsible for causing domain

wall pinning in materials that possess comparable thickness of domain walls, i.e. ≈ 100 nm.

2.6 Magnetization Dynamics

Magnetization dynamics refers to the time-dependent behavior of the magnetization in magnetic materials, particularly how it responds to external influences such as magnetic fields or temperature changes. Magnetization dynamics can be observed at various time scales, from extremely fast processes that occur within nanoseconds or even femtoseconds to slower processes that can take milliseconds or longer. The balancing of magnetic energies in a magnetic material determines the final state of material. The sum of all the energies can be termed as total energy, given as:

$$E_{\text{total}} = E_{\text{Zeeman}} + E_{\text{ex}} + E_{\text{MC}} + E_{\text{d}}, \quad (8)$$

that corresponds to total or effective field

$$\mu_0 \mathbf{H}_{\text{eff}} = - \frac{\delta E_{\text{total}}}{\delta \mathbf{M}}, \quad (9)$$

which results in an effective magnetic field that only vanishes when the magnetic system is at equilibrium.

The final state of magnetization of a material is determined by the initial state along with the entailed magnetic energies, leading to the static or dynamic equilibrium state. The magnetization dynamics usually occurs within the time scale of nanoseconds. An example of a static equilibrium state would be a magnetic domain configuration, whereas an example of a dynamic state would be spin-waves or magnetic-resonance states.

2.6.1 Magnetization Dynamics around the Field

Landau-Lifshitz (LL) equation of motion for magnetic moment in an external magnetic field is given as:

$$\frac{d\boldsymbol{\mu}(t)}{dt} = -\gamma \boldsymbol{\mu}(t) \times \mathbf{H}(t), \quad (10)$$

in which γ is the gyromagnetic ratio equals to $\gamma = \frac{ge}{2m}$, where g is the gyromagnetic splitting factor. For solid state, external magnetic field is replaced with effective magnetic field (Eq. 9), considering all the internal and external contributions and magnetic moment to be replaced by macroscopic magnetization [4]. Therefore, LL equation for macroscopic sample will take the form:

$$\frac{d\mathbf{M}(t)}{dt} = -\gamma\mu_0\mathbf{M}(t) \times \mathbf{H}_{\text{eff}}(t). \quad (11)$$

Eq. (11) describes the precession of magnetization around the effective field with a resulting frequency determined by the value of the field. It is to be noted here that magnetization does not align parallel to the external field, depicted in Fig. 2.4a, and instead it precesses infinitely. However, an additional term accounting for dissipation causes the magnetization motion to relax to a stable equilibrium, which can be seen in Fig. 2.4b. This effect accounting for the magnetic dissipation is referred to as magnetization damping, and is phenomenologically introduced in (11) as follows:

$$\mathbf{H}_{\text{diss}} = -\alpha \frac{1}{\gamma\mu_0 M_s} \frac{d\mathbf{M}}{dt}, \quad (12)$$

where α is the Gilbert damping parameter. Inserting (12) in Eq. (11) gives Landau-Lifshitz-Gilbert (LLG) equation for magnetization motion:

$$\frac{d\mathbf{M}(t)}{dt} = -\gamma\mu_0\mathbf{M}(t) \times \mathbf{H}_{\text{eff}}(t) + \frac{\alpha}{M_s} \left(\mathbf{M}(t) \times \frac{d\mathbf{M}(t)}{dt} \right). \quad (13)$$

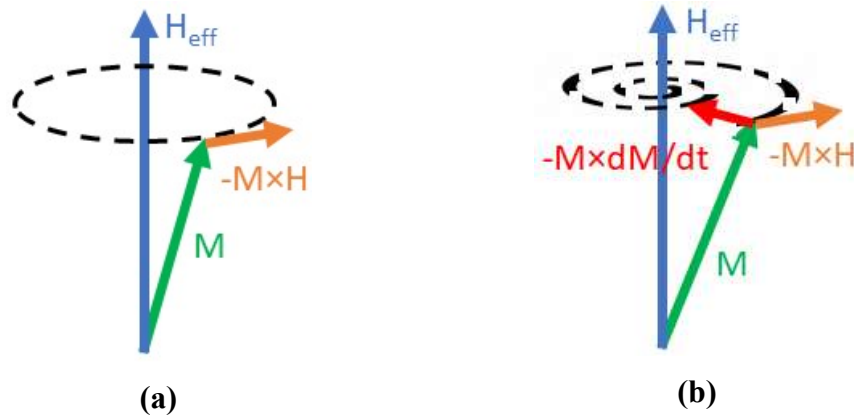


Figure 2.4. (a) Depiction of LL equation without damping. Magnetization rotating at constant radius around \mathbf{H}_{eff} (black dotted line). (b) The Gilbert damping leading to another component moving \mathbf{M} towards direction of \mathbf{H} in a spiral path.

In ferromagnetic materials, for each applied magnetic field, there is a resulting effective field from the collective contributions of all the magnetic moments that determines the precession frequency, which is called ferromagnetic resonance (FMR) frequency, and the phenomenon is termed as ferromagnetic resonance that was discovered by Griffiths [5]. When an external oscillating magnetic field is applied to a ferromagnetic material and sweeping the frequency of AC external field, ω_{ac} , the absorption of the signal is observed in the material, which corresponds to resonance when $\omega_{\text{ac}} = \omega_0$. The fit obtained with the absorption peak gives the ferromagnetic frequency at specific DC external field (Zeeman field) and the linewidth provides information related to damping of the material. Furthermore, dependence of ferromagnetic frequency can be found by sweeping the Zeeman field that leads to evaluate the effective field of the sample. Thus, quantities such as gyromagnetic ratio, exchange stiffness, damping constant, can be measured employing this FMR technique. It also gives the accurate measurements of the saturation magnetization and anisotropy for materials with special geometries such as thin films [6].

2.6.2 Magnetoelastic Interactions

Magnetoelastic interactions are divided into two types of effects, namely, the magnetostrictive effect which is the effect of magnetization direction on the

internal strain in magnetic material; and Villari effect which is the influence of strain on the magnetization state.

Magnetostriction is evident in magnetic materials that experience dimensional modifications when the magnetization states of the material undergo switching process. This implies that changing magnetization states results in distinct strain distributions within the material due to the magnetostrictive effect. In 1842, J. Joule observed the mechanical deformation of ferromagnetic rod after being magnetized. This phenomenon is termed as magnetostriction effect [7], and later, the inverse magnetostriction effect (or magnetoelastic effect) was observed by E. Villari in 1865 [8] when the magnetization of ferromagnetic material was altered under the stress. This effect takes place due to the spin moments coupling to lattice via orbital electrons [9]. Therefore, due to change in lattice parameter caused by strain, the magnetic ordering in a material is affected, leading to induced anisotropies. This results in change in magnetization of the material. The magnetoelastic anisotropy can be described as [10]:

$$K_{ME} = -\frac{3}{2}\lambda_s Y |\varepsilon_{xx} - \varepsilon_{yy}|, \quad (14)$$

where Y represents the Young's modulus of magnetostrictive material, and ε_{ii} denotes the strain applied along the i -th axis.

In the case of a crystal with cubic crystal symmetry, the magnetoelastic energy density, neglecting second-order effects, is expressed as follows [11, 12]:

$$\begin{aligned} \varepsilon_{mel} = & B_1 \left(\varepsilon_{xx} \left(m_x^2 - \frac{1}{3} \right) + \varepsilon_{yy} \left(m_y^2 - \frac{1}{3} \right) + \varepsilon_{zz} \left(m_z^2 - \frac{1}{3} \right) \right) \\ & + B_2 \left(\varepsilon_{xy} m_x m_y + \varepsilon_{yz} m_y m_z + \varepsilon_{zx} m_x m_z \right), \end{aligned} \quad (15)$$

in which B_1 and B_2 denote the linear isotropic and anisotropic magnetoelastic coupling constants, respectively. The strength of the interaction among strain and magnetization of the films is determined by these coupling constants. This is illustrated by few of the studies carried out earlier by inducing surface acoustic waves (SAW) in piezoelectric substrates deposited with magnetic films. For instance, inducing the SAW signal of different frequencies in LiNbO_3

substrates deposited with same thickness of ferromagnetic Ni thin films leads to various coupling constant values. For 500 MHz, the constant value was found to be 9 MJ/m³ [13], whereas for 1 GHz and 3 GHz, it is calculated to be 11 MJ/m³ and 0.5 MJ/m³, respectively, which is a clear indication that the strength of the interaction is non-linear. Using the same substrate with Co thin film being deposited, the coupling constant value was calculated to be 3 MJ/m³ at 1 GHz. The lower value in comparison with Ni at 1 GHz indicates the presence of stronger magnetic anisotropy in Co than in Ni. However, the coupling constant value for Heusler alloy (Fe₃Si) deposited on GaAs substrate at 500 MHz is obtained as 10 MJ/m³ [14]. The strength of this interaction leads to the estimation of the magnetization rotation in the thin films caused by the strain. Saturation magnetization's magnitude does not influence the magnetoelastic energy or strain state. Instead, these factors are determined by the orientation of the magnetization vector. Therefore, using Eq. (9) and (15), the influence of magnetoelastic field to the effective field is given by:

$$\mathbf{H}_{\text{mel}} = -\frac{1}{\mu_0 M_s} \begin{pmatrix} 2B_1 \epsilon_{xx} m_x + B_2 (\epsilon_{xy} m_y + \epsilon_{zx} m_z) \\ 2B_1 \epsilon_{yy} m_y + B_2 (\epsilon_{xy} m_x + \epsilon_{yz} m_z) \\ 2B_1 \epsilon_{zz} m_z + B_2 (\epsilon_{zx} m_x + \epsilon_{yz} m_y) \end{pmatrix}. \quad (16)$$

It is pertinent to mention that the magnetoelastic field is influenced by various elements of both the strain tensor and magnetization components. Consequently, if there is non-uniformity in either the strain or magnetization, the magnetoelastic field will also exhibit non-uniformity. Hence, the energy changes induced by these diverse fields are referred to as magnetoelastic energy. Since then, the field of straintronics [15] has been introduced and it is inferred that spintronics devices in which magnetization is switched by strain rather than other methods, such as magnetic field [16], ultrashort current pulses [17 – 19], ferroelectric switching [20], electric field, [21], and optically induced thermal gradients [22], may lead to significant energy dissipation reduction [23].

CHAPTER 3

Chapter 3

X-RAY PHOTOEMISSION ELECTRON MICROSCOPE (XPEEM)

The term "X-ray Photoemission Electron Microscope," often abbreviated as "XPEEM," refers to an advanced imaging and analytical instrument used in materials science and surface science. XPEEM combines the capabilities of X-ray photoemission spectroscopy (XPS) and X-ray absorption spectroscopy (XAS) and electron microscopy to provide detailed information about the composition, chemical states, and morphology of surfaces and thin films at the nanoscale. In XPEEM, a sample is irradiated with X-rays, which causes the emission of photoelectrons from the sample's surface. These emitted photoelectrons are collected, and their kinetic energy and angular distribution are measured. The resulting data can be used to create high-resolution images of the sample's surface and to determine the elemental composition and chemical states of the materials.

In this chapter, synchrotrons as advanced X-ray sources and the radiation properties are described. The X-rays are used to illuminate the sample in the XPEEM, whose design and operation principles are treated next. Finally, the specific endstation where this dissertation was conducted is introduced and special sample holders which were built during the thesis are shown.

3.1 Synchrotron and Synchrotron Radiation

Since the discovery of X-rays in 1895, they have been widely utilized as a versatile tool for research in almost every scientific field, including physical, chemical, biological, pharmaceutical, and archaeological analysis [24, 25]. Due to the broad spectrum and significant penetration depth of X-rays, scientists can uncover the structure of materials and study dynamics on the nanometer length and nanosecond timescales, which has played a crucial role in understanding a material's bulk properties and electronic structure [26].

Synchrotrons as used for X-ray generation (light sources) are electron accelerator complexes with storage rings which generate synchrotron radiation that features intense X-rays with variable and precise energy and polarization states. At the basis is the process of Bremsstrahlung, i.e. when electrons and other charged particles are accelerated and change their trajectories under the influence of a magnetic field, they emit electromagnetic radiation characterized as synchrotron radiations [27]. The schematic planar view of a synchrotron is shown in Fig. 3.1.

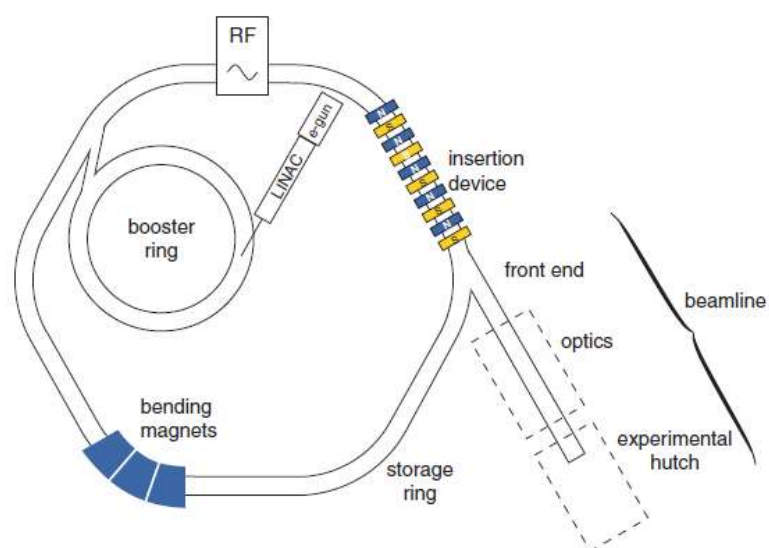


Figure 3.1. Schematic display of vital components of modern synchrotron source. Electrons are accelerated through LINAC and booster and injected into the storage ring. Radiation is emitted at the bending magnets and by the insertion devices. The emitted photons travel down the beamlines where they are employed for the experiments. The radio frequency (RF) supply helps to regain the energy which is lost by the radiation of synchrotron light by electrons [28].

A synchrotron consists of three main accelerator sections [5]. Electrons are extracted from an electron gun and transferred to a linear accelerator (LINAC), where they undergo acceleration until they reach energies of several million electron volts (MeV). Subsequently, they are injected into the booster ring, where they are further accelerated to reach energies of several giga-electron volts (GeV) before being introduced into the storage ring.

The booster ring periodically injects electrons in bunches to maintain the specified current level within the storage ring. This is necessary to replenish the storage ring with electrons when its current decreases due to loss of electrons, for example due to a collision with a rest gas molecule. Once inside the storage ring, the electrons pass through bending magnets strategically placed at circular points along the ring's path. These magnets keep the electrons on their racetrack orbit.

The first-generation synchrotrons were primarily used for particle physics-related experiments and were considered parasitic facilities. They operated with storage-ring energies which are efficient for photon production in the ultraviolet and soft X-ray regimes. The first dedicated facility designed to obtain synchrotron radiations marked the emergence of second-generation synchrotrons, achieved through the development of powerful electron storage ring systems incorporating bending magnets.

Subsequent advances aimed at enhancing X-ray beam brilliance, accomplished through the careful design of bending magnets and the installation of insertion devices (IDs), such as wigglers and undulators. These IDs are positioned along the longitudinal path of the storage ring, causing periodic perturbations in the electron's trajectory without affecting their average direction, resulting in the production of synchrotron radiations.

This system, with the inclusion of IDs, defines the 3rd generation synchrotron facility, renowned for its superior brilliance. The schematic view of a 3rd generation storage ring, depicting its main components, is illustrated in the following figure.

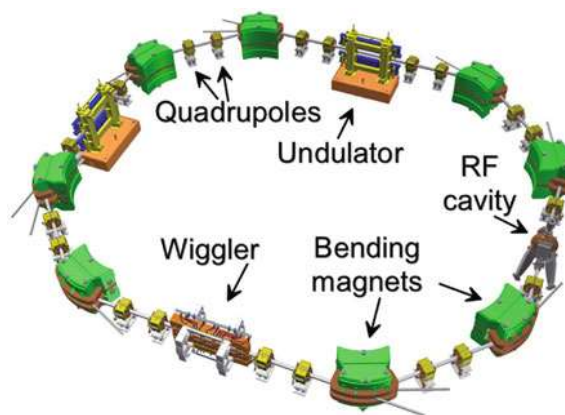


Figure 3.2. Schematic illustration of a storage ring depicting main components like bending magnets, undulators, wigglers, quadrupoles, and RF cavity [27].

The purpose of quadrupole magnets is to focus (CHECK) the beam during its motion. Wigglers are magnetic structures located in the straight sections of a storage ring. Magnetic fields applied by these wigglers cause electrons to follow a wiggling path, resulting in the emission of synchrotron radiations.

In third generation synchrotrons, undulators were introduced. Unlike wigglers and bending magnets, undulators provide spectra with narrow bands of radiations. These radiations interfere constructively, producing a spectrum with a fundamental frequency. As a result, the emittance and brightness of the radiation are significantly higher than what can be obtained from bending magnets and wigglers alone. A qualitative comparison between the wiggler spectrum and that of the undulator is shown below.

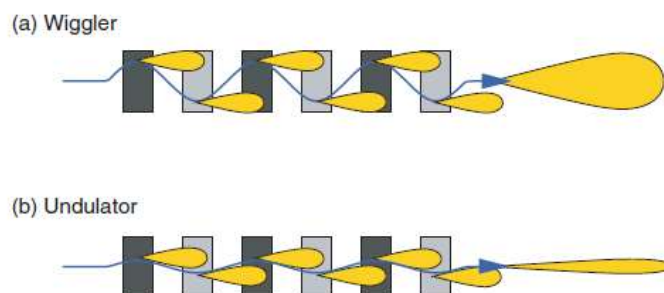


Figure 3.3. The main difference between wigglers and undulators is only the excursion size which electrons are forced to experience from straight path [28].

During the acceleration of electrons and the emission of electromagnetic radiations, electrons lose their energy. Without replenishing this energy, electrons would spiral toward the inner wall of the storage ring and be lost. To prevent this loss, radio frequency cavities are employed. Electrons enter these cavities and are accelerated by the electric field, thus regaining the lost energy.

The beamlines are located along the axes of the IDs and tangentially to the storage ring and bending magnets [28]. The initial section of the beamline is termed front end and has the following functions:

- a. It provides a separation between beamline vacuum and storage ring vacuum.
- b. It monitors the position of the photon beam.
- c. When required, it restrain the X-rays from reaching to the sections consisting of the optics and experimental hutches.
- d. The front end separates the low-energy tail of the synchrotron radiation spectrum, which can be absorbed by matter and potentially damage the optical components.

Before entering the experimental station, the beam passes through the optics section which typically consists of several mirrors controlling position and focus of the beam and a monochromator filtering the photon energy. The beam can be further shaped by apertures. Beamlines that use high-energy X-rays are shielded with lead-lined concrete walls to prevent user exposure to these rays. This protection is not only for X-rays but also for gamma rays that can result from collisions between gas particles and relativistic electrons in the storage ring. The energy of these gamma rays is on the order of GeV. As a result, experiments are conducted remotely within the experimental hutches, ensuring safety from radiation.

3.1.1 Properties of Synchrotron Radiation

The electromagnetic radiation emitted by synchrotron and used for experiments is mostly in the X-ray regime. X-rays are the type of electromagnetic radiations that exhibit wavelength in the range of 0.01 – 10 nm, which correspond to energies of 100 – 100 keV. This is illustrated in Fig. 3.4.

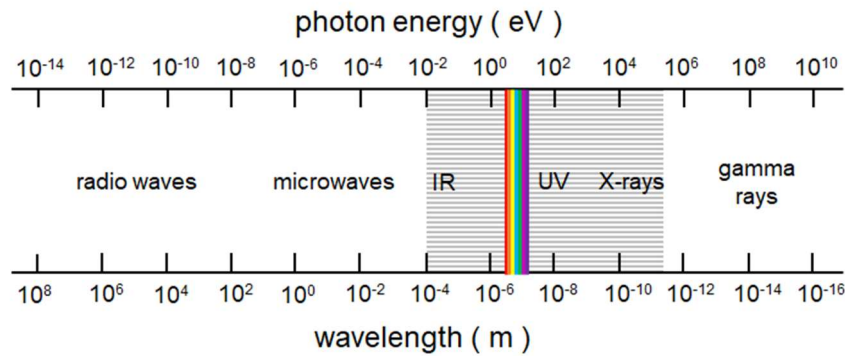


Figure 3.4. *The Spectrum of Electromagnetic radiations in which the grey-striped region depicts the synchrotron photon energies from 0.01 eV to 5×10^5 eV.*

Synchrotron radiation holds distinct properties which enables it to play a vital role in the scientific research. The most outstanding properties are elaborated below [28]:

a. Flux, Emittance, and Brilliance

3rd generation synchrotrons are equipped with storage rings that optimize the photon beam flux and brilliance required for advanced experiments. Flux is defined as the number of photons per second per unit bandwidth passing through a defined area, in practical terms, the total intensity for a given energy range. The flux emitted by electrons is proportional to the square of their acceleration, and the centripetal acceleration exerted in the storage ring is proportional to γ^2 , where, γ represents the Lorentz factor $\gamma = \frac{\epsilon}{mc^2}$, with mc^2 the rest mass energy of the electron. Therefore, the flux is proportional to γ^4 , and higher energy storage rings are in principle favorable for higher total flux.

Emittance describes the geometrical distribution of the emitted photons, defined as the product of the source size and the emission angle. A low emittance beam can be focused by optical method to a smaller spot size. Modern synchrotron light sources are optimized for low emittance values, i.e. small spot size (electron beam) and almost parallel emission angle.

Brilliance is basically flux divided by emittance, i.e. the total number of photons per energy bandwidth that can be focused into a given spot. To optimize brilliance, a high flux and low emittance are needed. Brilliance is the decisive quantity for many synchrotron experiments.

b. Coherence

Coherence is the capacity of the beam to interfere with itself. There are two main limits on the beam coherence. The longitudinal coherence time comes from the finite bandwidths of the source and is defined as the time it takes for the phase of two waves with different frequencies to change by 2π radians. It describes how various frequencies within the beam's bandwidth will gradually move out of phase with each other. In a beamline, the most important component for this longitudinal coherence is the monochromator. A second type of decoherence occurs when photons with the same frequency travel with slightly different angle. The transversal coherent length is dominated by the finite source size with divergence and can be affected by errors in the optical components.

c. Polarization

Synchrotron radiation, like any light can have different polarization of the electric field vector. The polarization of the synchrotron X-rays, as they exit the storage ring, depends on the line of sight, as depicted in Fig. 3.5, for a bending magnet source.

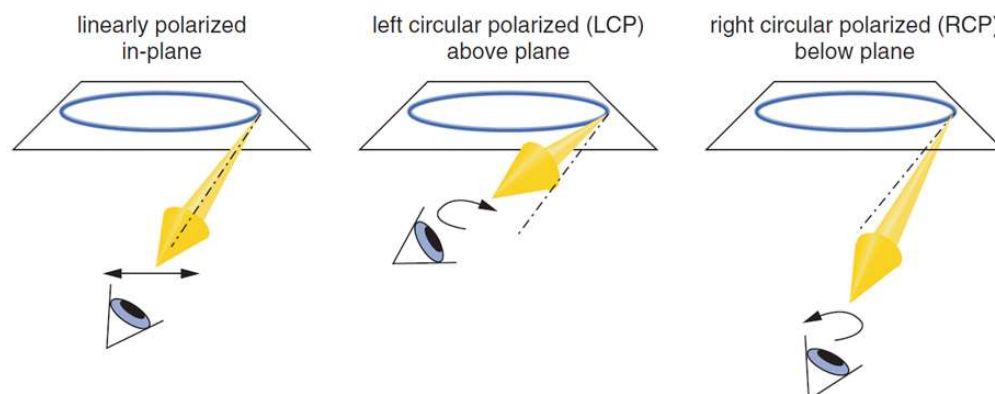


Figure 3.5. Depiction of polarization of synchrotron radiations with respect to viewer's frame of reference relative to the electron's orbital plane [28].

If observed within the plane of the electron's orbital, the polarization is linear within that specific plane due to the oscillation of electrons in the horizontal plane. When the line of sight is above the storage ring plane, the electrons appear to exhibit an elliptical orbit in a clockwise orientation. As a result, the angular momentum (\hbar) from the observer's reference is transferred to the emitted beam, making it left-circularly polarized (LCP). Conversely, if the observer's frame of reference is below the electron's orbital plane, the polarization is right-polarized (RCP). In the former case, photons carry a negative angular momentum of $-\hbar$ while in the latter, it's a positive $+\hbar$. Similar considerations apply to IDs like wigglers and undulators when the electron orbit in the ring is substituted by the electron path in the ID magnetic field.

The polarization of synchrotron light plays a crucial role for many experiments and techniques, for example, dichroic studies targeted at magnetism or other electronic phenomena, like orbitals.

3.2 Photoemitted Electrons

While in principle there are different ways of how X-rays can interact with matter (absorption, scattering), the process relevant for the PEEM technique is the emission of electrons upon absorption of X-rays by a material. Independent of the intensity of the incoming X-rays, if the frequency of the X-rays is greater than the binding energy of the electron in an atom, the electron can be emitted and is called photoelectron (or primary electrons), and the phenomena is known as Photoelectric effect. The electron kinetic energy is then given by [29]:

$$E_k = \hbar\omega - E_b - \Phi \quad (17)$$

where $\hbar\omega$ is the energy of X-rays which is fixed, Φ is the work function of the analyzer, and E_b is the binding energy of electron, and the analysis of Eq. (17) is the basis of X-ray photoemission spectroscopy (XPS).

If the initial electron undergoes scattering processes within the material, or another electron from an outer shell fills the vacancy, emitting another photon, additional electrons can be emitted from the sample. In general, those electrons

are emitted with a low kinetic energy. These secondary electrons, also called low-energy Auger, constitute the vast majority of electrons emitted and their number is proportional to the absorbed X-rays. The detection of all outgoing electrons or the measurement of the replacing electrical current (drain current) is one way to perform X-ray absorption spectroscopy measurements (XAS).

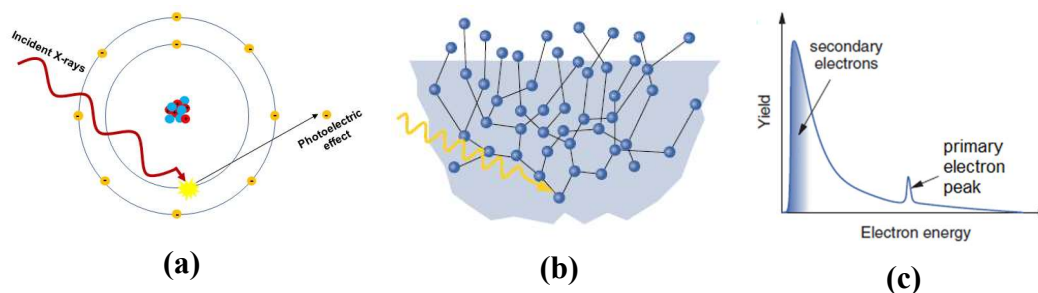


Figure 3.6. Type and process of emitted electrons by X-ray absorption in PEEM. **(a)** direct photoemission of an electron by X-ray absorption **(b)** Secondary electrons are produced due to cascade of events initiated by production of photoelectrons. As soon as the kinetic energy of electrons decreases, mean free path increases, which leads to **(c)** an intense peak in the generation of low energy electrons in comparison to Auger electron intensity at higher energies [30].

3.3 X-ray Photoemission Electron Microscopy (XPEEM)

Photoemission electron microscopy (PEEM) is a microscopic technique [31] first developed in 1933 by Ernst Brüche [32], who demonstrated that photoelectrons produced by UV light can be used to obtain an image of the sample. These photoelectrons can be exploited for high-quality imaging when accelerated with a high voltage towards the first (objective) lens. A related technique which uses a similar high voltage field between the sample and the objective lens is Low-energy electron microscopy (LEEM) [33–35] that investigates surfaces and interfaces of materials by elastically back-scattered electrons [36]. Many dynamic processes, including surface reconstruction, step dynamics, epitaxial growth, etc., can be monitored due to the large electron backscattering cross-section of materials, permitting video frame rate acquisition in LEEM. The idea of LEEM was first proposed by Ernst Bauer [37]

and first trials for this technique were carried out in the 1960s. A schematic display of this technique is presented in Fig. 3.7.

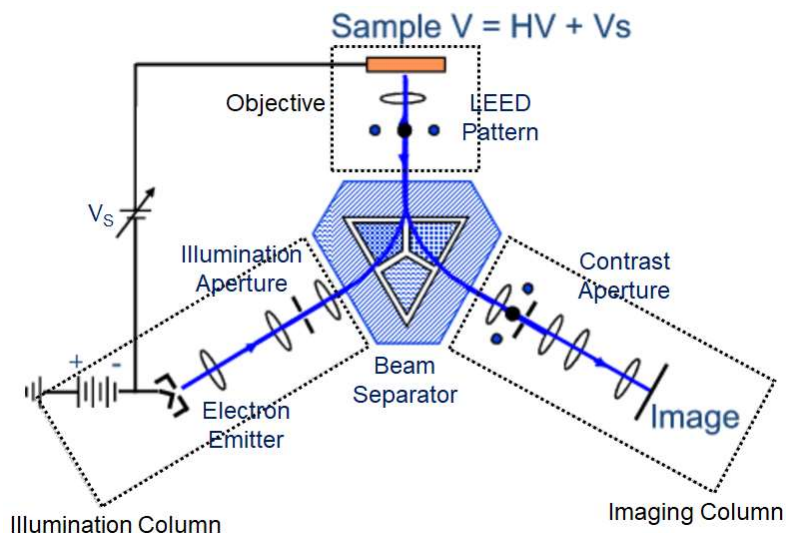


Figure 3.7. Simplified schematic demonstration of a LEEM setup [35].

Electrons are emitted from the emitter (often a LaB_6 crystal) and form a parallel beam in the illumination column. This parallel beam of electrons is deflected by a prism optic (beam separator) and falls orthogonally onto a flat surface. A biased potential is applied between the sample and the lens system to decelerate the electrons to lower energies. The backscattered electrons are deflected into the imaging column after acceleration from the sample. The electrons are then manipulated by multiple lenses to form an image on a two-dimensional imaging detector. Changing the lens settings, either a real space or a reciprocal image (LEED) can be focused on the detector. The size and spot of the electron beam falling onto the surface of the material can be defined by the illumination aperture. Given that the accelerating field and the lens system is already in place, by employing suitable light sources, a LEEM can also be used as PEEM [38]. With the advent of Synchrotron X-rays, it is possible to capture images depicting the spatial distribution of electrons emitted by samples via X-ray photoemission spectroscopy (XPS) and X-ray Absorption Near Edge Structure (XANES) [30]. Depending on the accepted electron energy, these are either primary or secondary electrons emitted upon the interaction with X-rays,

as shown in Fig. 3.6. When the mean free path between the electrons becomes longer due to low energy (a few eV), these electrons escape the material's surface and are collected by PEEM optics. A typical graph illustrating the relationship between yield and electron energy can be seen in Fig. 3.6c, showing a maximum yield above the work function and a decrease in yield with increasing energy.

X-rays emit a wide spectrum of electrons, encompassing energies from the material's illumination level to its work function. This results in a broader range of energies for image formation compared to UV radiation [39], which is addressed by the addition of an electron energy filter (analyzer).

3.3.1 Instrumentation

3.3.1.1 Principle of Operation

The schematic layout of the PEEM only microscope is depicted in the following figure, omitting the electron gun and adding the electron kinetic energy analyzer:

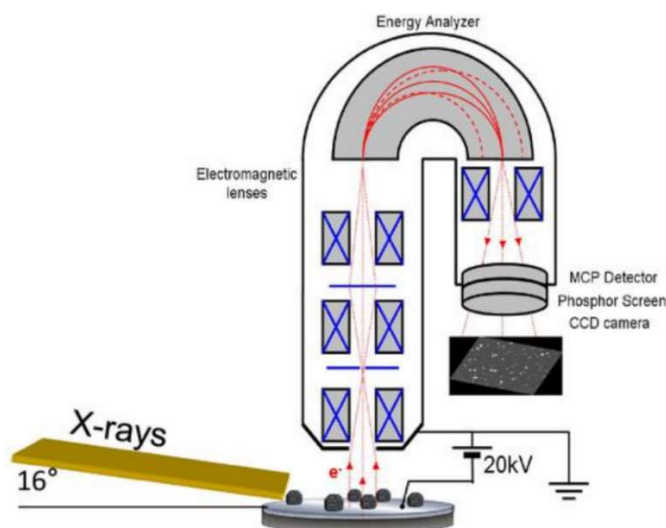


Figure 3.8. Schematic illustration of the XPEEM [40].

In XPEEM (X-ray Photoelectron Emission Microscopy), X-rays illuminate the sample's surface, leading to the emission of photoelectrons. These photoelectrons are then accelerated using a high voltage (typically 10 – 20 kV)

to maintain their local information. Electromagnetic lenses magnify the image, and the microscope includes deflectors and stigmators for optimizing the electron path. Finally, a multichannel plate, coupled to a phosphorous screen, detects the electrons, allowing sensitive CCD cameras to capture the image.

3.3.1.2 Lateral Resolution

The lateral resolution of the PEEM microscope depends on several factors, and can reach down to a few nanometers [31]. These factors are:

- The accelerating HV field
- The mechanical stability of the setup
- Quality of the detector
- Space charge (electrons inside the microscope travel in bunches and repel each other. This issue is particularly important with pulsed light sources, like synchrotron [41]).
- The geometrical and chromatic aberrations of the electron lens system

There are several ways to improve the electron optical system performance. An iris (contrast aperture), inserted in the back focal plane (BFP) of the objective lens, defines the angular reception of the microscope, reducing geometrical aberrations. The smallest useful contrast aperture size is reached when diffraction effects come into play. Chromatic aberrations (different optical characteristics for different electron energies) can be reduced by selecting a narrow pass energy band (electron analyzer) and by aberration correction (AC) of the objective lens by an electron mirror, which has become recently available. The use of AC not only increases the resolution but can also enhance transmission by allowing the use of larger contrast apertures [42]. As a general rule, however, improvements come with a reduction in intensity.

3.3.2 Multi-Technique Surface Characterization in a LEEM-PEEM Instrument

As mentioned before, PEEM is often used in conjunction with LEEM. Thanks to the adaptable electron optics a combined LEEM-PEEM instrument can be used in different modes to obtain complimentary characterization of samples. With the electron gun, LEEM offers high-resolution imaging and low-energy spectroscopy (LEEM-IV) and micro-spot diffraction (μ -LEED), and dark-field imaging with a selected LEED reflection. These measurements address mostly morphological and structural properties. When the incoming electron energy is varied around the threshold of reaching the sample, i.e. the MEM-LEEM transition (MEM = Mirror Electron Microscope), work function contrast and differences are resolved. The change between imaging and diffraction (LEED) is realized by adjusting the strength of the electron lenses. A third type of measurement is the dispersive mode where the dispersive plane of the electron analyzer is imaged onto the detector. A representation of these modes is shown in Fig. 3.9.

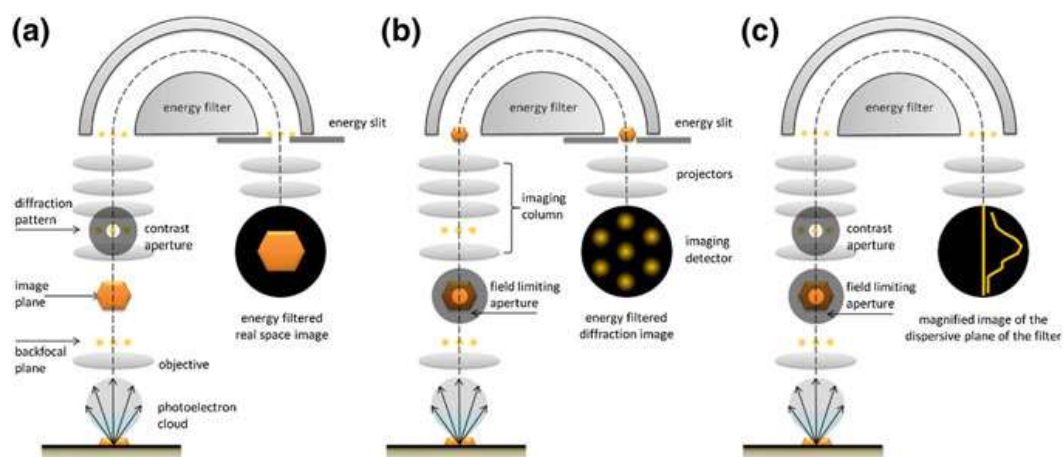


Figure 3.9. Various operation modes of LEEM-PEEM microscope with respective optical configurations, (a) spectroscopic imaging, (b) spectroscopic diffraction imaging, and (c) micro spectroscopy (dispersive) operation [43].

3.3.2.1 XPEEM

The term XPEEM is commonly used to refer to a PEEM instrument operated with synchrotron radiation in form of X-rays, which allows to extract additional information from the sample.

3.3.2.2 X-ray Absorption Spectroscopy (XAS) with PEEM

Spectroscopic imaging with X-ray absorption spectroscopy (XAS), was introduced by Tonner and Harp [44]. Transitions typically occur at the L, M, and N edges of metal and metal oxide materials, providing insights into the magnetic and chemical behavior of these substances. XAS is carried out using a laterally-resolved method, measuring the intensity of low-energy secondary emitted electrons as a function of photon energy. Therefore, the X-ray monochromator determines the energy resolution. The large inelastic mean free path of these photoelectron energies enables examination of concealed layers and interfaces within materials up to a few nanometers deep from the surface. When analyzing organic and carbon-related materials, the transition occurs at the C K-edge. However, the problem in this energy range is the typical contamination of the beamline optical elements with carbon residues, resulting in strong variations of incoming photon flux.

3.3.2.3 XMCD and XMLD with PEEM

Other than the photon energy, also, photon polarization can be exploited. The most common examples are X-ray magnetic circular dichroism (XMCD) and X-ray Linear Dichroism (XLD) which can be of magnetic (XMLD) or non-magnetic origin. When illuminating the sample with polarized X-rays, the absorption cross section and therefore the detected electron intensity depend for instance, on the relative orientation of the sample magnetization and the beam polarization. For the physical explanation of the XMCD effect, refer to [45].

Images with magnetic contrast are achieved by pixel-wise subtracting two images with different photon polarizations, such as circular right and left in XMCD, and linear horizontal and vertical in XMLD, and then normalizing the result by the sum of the two images, as in Eq. 18 [40]:

$$I_{\text{XMCD}} = \frac{\sigma^+ - \sigma^-}{\sigma^+ + \sigma^-} \quad (18)$$

where (σ^+) denotes the circular right polarization and (σ^-) denotes the circular left polarization. The XMCD is sensitive to the magnetization component projected onto the incoming beam, represented by an equation [46]:

$$I_{\text{XMCD}} \propto \hat{\mathbf{k}} \cdot \mathbf{M}, \quad (19)$$

in which \mathbf{M} corresponds to direction of the sample magnetization onto the helicity vector, which is along the incident beam projection $\hat{\mathbf{k}}$.

In most instruments, the XMCD-PEEM is preferentially sensitive to the in-plane component of the magnetization vector because of the grazing-incidence angle of the X-ray beam.

XMLD is the difference in XAS cross section for the electric field vector (\mathbf{E}) of linear polarized X-rays oriented parallel and perpendicular to spin axis [47], which can be written as:

$$I_{\text{XMLD}} = \mu_{\parallel} - \mu_{\perp}, \quad (20)$$

in which μ_{\parallel} and μ_{\perp} correspond to parallel and perpendicular polarization, respectively, of the X-rays. In XMLD, the contrast is proportional to the the square of the dot product of X-ray polarization (electric field vector \mathbf{E}) and local magnetization vector, as depicted in Eq. 21:

$$I_{\text{XMLD}} = |\mathbf{E} \cdot \langle \mathbf{M} \rangle|^2 \quad (21)$$

The XMLD is particularly useful for antiferromagnetic systems where the XMCD signal cancels (no net magnetization) but spins are still oriented as, for example, in collinear systems. Due to the square on the factor in Eq. 21, the XMLD signals from two neighboring antiparallel spins do not cancel, but add up, thus allowing the imaging of the antiferromagnetic domains.

3.3.2.4 X-ray Photoemission Spectroscopy (XPS)

When primary photoelectrons with comparatively high kinetic energy are selected with the analyzer, one refers to X-ray Photoemission Spectroscopy (XPS-PEEM).

By varying the detected electron kinetic energy E_k , e.g. by applying a bias voltage to the sample (V_{start}), spectral imaging is performed. The resulting image stacks allow to extract local XPS spectra. The energy resolution in this case is given by the combination of the incoming photons (beamline) and the

analyzer pass widths defined by an energy slit. Since count rate is typically low in these settings, an alternative way for measuring local spectra is to introduce an aperture in an image plane (field limiting aperture) and use the microscope in dispersive plane (Fig. 3.9c). With core-level and valence band photoemission PEEM, one can determine the local occupancy of the sample and map variations in composition and chemical environment. The same field limiting aperture is also used to define the area from which local angular resolved photoemission spectroscopy (μ -ARPES) measurements are obtained as $k_x - k_y$ maps when using the microscope in diffraction mode (Fig. 3.9b).

3.4 XPEEM Facility at the CIRCE Beamline – ALBA Synchrotron, Barcelona, Spain

ALBA is a 3rd generation synchrotron light source that incorporates a composite of electron accelerators for the generation of synchrotron radiation, enabling the understanding of atomic structuring of matter through the analysis of various properties. The energy of 3 GeV is currently achieved with a current of 250 mA and an emittance of 4.3 μm radians [48, 49]. The perimeter of the storage ring is 270 m, housing 12 state-of-the-art beamlines that cover the soft and hard X-ray range for various characterizations.

The XPEEM experimental station is based on an Elmitec GmbH commercial LEEM-III, and is utilized as Spectroscopic Photoemission and Low Energy Electron Microscopy techniques (SPELEEM). The X-ray source used at the beamline is an APPLE II helical undulator capable of operating with variable polarization. Soft X-ray photons, in the energy range of 0.1 – 2 keV, are directed through a plane-grating monochromator and delivered to two independent branches: PEEM and NAPP (Near Ambient Pressure Photoemission). Two toroidal mirrors are used after the monochromator chamber to focus the beam onto an exit slit, and a pair of deflecting mirrors guide the beam to either branch. Here, we present the details of the characteristics of the experimental station dedicated to the XPEEM facility.

3.4.1 The Experimental Station Layout and Microscope

The setup of the XPEEM, along with its various sections, is illustrated in Fig. 3.10. A detailed explanation of the setup and the microscope can be found in [50]. The system consists of several vacuum chambers, including the main chamber (microscope), a preparation chamber, a load-lock section, and an entrance chamber. To introduce a sample into the system, it is first inserted into the load-lock. Once a sufficient vacuum of 10^{-7} mbar is achieved, the sample is transferred into the entrance chamber. The entrance chamber contains multiple parking spaces for storing sample holders, which can be moved and stored using a linear manipulator. Following the entrance chamber is the preparation chamber, equipped with various tools for surface preparation, such as argon sputtering, oxygen treatment during heating, and degassing of the samples. The sample can then be moved to the main chamber, where imaging can be performed without breaking the vacuum between any chambers. Both the preparation and main chambers are equipped with several evaporators for performing molecular beam epitaxy deposition of thin films. Inside the main chamber, a six-fold manipulator is used to position the sample holder, allowing X-rays to illuminate the sample. This setup enables various characterization techniques, ranging from LEEM and LEED when using an electron source to synchrotron-related XPEEM, XAS, and XPS.

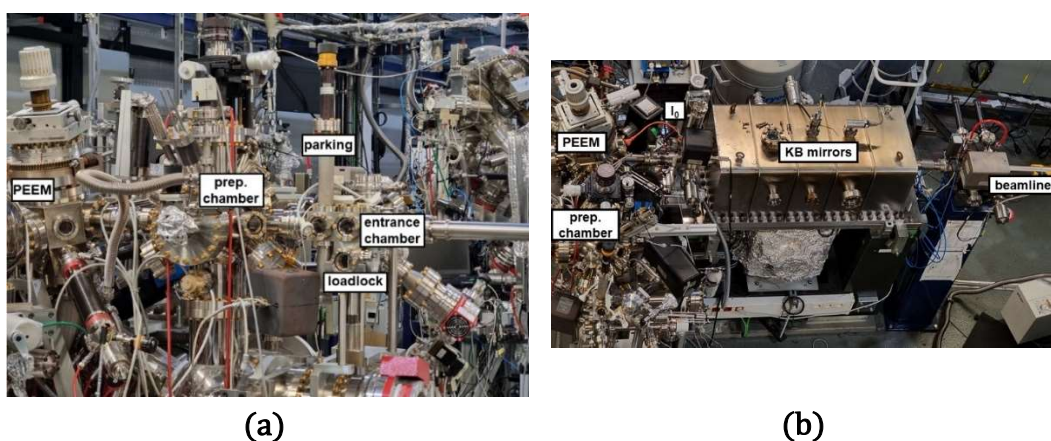


Figure 3.10. (a) Side-view of the XPEEM experimental station including main chamber (PEEM), preparation chamber, entrance chamber, parking, and prompt pumping load lock. (b) Top view of the experimental station and the last section of the beamline, I_0 and KB refocusing mirrors chamber.

Upstream of the microscope (Fig. 3.10b), there is an I_0 measuring chamber equipped with various components, including a gold mesh, gold foil, gold evaporator, fluorescent screen, and a calibrated photodiode. However, typically, the drain current of the last focusing mirror is used to obtain the normalization signal. The X-ray beam is incident on the sample at an angle of 16° degrees due to the tilted geometry of the chamber, with the sample surface facing downward. The photon beam emerging from the synchrotron is wider horizontally than vertically. As a result, the beam projection causes elongation across the surface along the narrow vertical dimension of the X-ray beam.

The microscope, I_0 , and refocusing mirrors chamber are all placed on the same synthetic granite support, designed to minimize external vibrations and increase rigidity. The demagnification of the photon beam achieved by the bendable Kirkpatrick-Baez (KB) refocusing mirrors [51] is 3.8:1 along the horizontal plane and 6.1:1 along the vertical plane. These mirrors enable precise control of the photon beam. The microscope is equipped with a LaB₆ electron gun for LEEM and LEED, as well as a mercury lamp for UV-PEEM characterizations, in addition to soft X-rays. As mentioned earlier, in the case of LEEM, a magnified image is formed by the backscattered electrons at the sample's surface with a lateral resolution of 10 nm in real-time. For PEEM, electrons are excited by the photon source and collected to create the image. In the most frequently used mode, i.e. XPEEM with low-energy secondary electrons, a spatial resolution of down to 20 nm, has been demonstrated [25].

For regular operational situations, the sample is maintained at 20 kV and positioned at a distance of 2.8 mm from the objective lens. However, in various situations, a reduced field setting (operating voltage of 10 kV, and increased working distance, up to 5 – 6 mm) can also be utilized. On the one hand, there are experimental circumstances that increase the risk of electrical arcs, like insulating samples or degassing samples or sample holders (electromagnets), exposed wire bonds. On the other hand, certain samples are extremely sensitive to arcs, e.g. contacted electrodes and devices which are typically destroyed by the very first arc. In the reduced electric field setting, experimental resolution of at least 56 nm can be achieved [52].

3.4.2 Sample Holders at the CIRCE-PEEM

The XPEEM beamline at the Alba Synchrotron is equipped with various types of sample holders designed for conducting different experiments, as illustrated in Fig. 3.11.

In Fig. 3.11a, a standard Elmitec sample holder is depicted. It includes a filament for heating and a W/Re thermocouple. The sample is positioned at the top of the central region and secured with a cap featuring a hole in the center, available in various diameters for imaging the sample. These sample holders allow for sample heating up to 2000 K using the filaments, which utilize two of the electrical connection points on the sample holder. These connections are insulated from the sample holder body, as the body serves as a reference potential for the photoelectrons, also known as the start voltage. Two of the electrical contacts are reserved for the thermocouple, and two additional spare contacts are available for other purposes, like applying multi-axial magnetic fields or electrical signals to the sample.

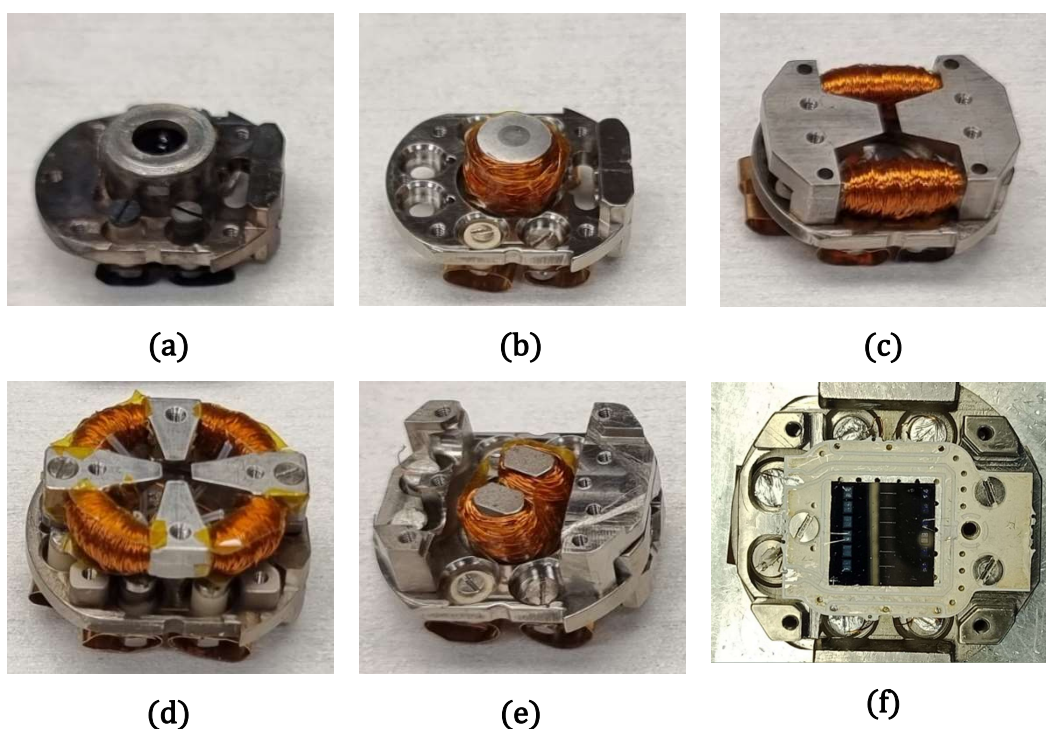


Figure 3.11. Types of sample holder the XPEEM beamline is equipped with. (a) Standard Elmitec sample holder for heating up to higher temperatures. (b) Sample

holder for applying the magnetic field in out-of-plane direction. (c) Uniaxial sample holder to apply the field along the sample axis. (d) Quadrupole sample holder capable to apply a vector magnetic field in the sample surface. (e) Sample holder compatible with the PCB to apply electrical signals as well as magnetic field within the plane of the sample. (f) Sample holder with PCB mounted to apply electrical signals.

Within the XPEEM chamber, magnetic fields can be applied to the sample using specific custom sample holders, as shown in Fig. 3.11(b-e). Fig. 3.11b demonstrates a sample holder that allows the application of an out-of-plane magnetic field. The field is generated by passing electrical current through a copper wire mounted on the Armco/Permendur yoke, with the length, diameter, and the number of windings determining the field strength at the sample.

Fig. 3.11c illustrates a uniaxial/in-plane sample holder, where the sample is positioned above the yoke, where the distance between the yoke elements is the most crucial quantity to achieve large magnetic fields. The drawback of small elements is a loss in spatial homogeneity of the field in the sample position. In Fig. 3.11d, a quadrupole sample holder is depicted, capable of applying a biaxial in-plane magnetic field, which can be swept through all angles when using suitable current values for each set of opposite coils.

Fig. 3.11e displays a sample holder that can carry a printed circuit board (PCB) for making connections to the sample surface to apply additional electrical signals. It also contains a small rotatable electromagnet to apply a magnetic field in any direction along the sample surface. In Fig. 3.11f, the assembly with PCB and sample is shown, where contacts are established via wire bonds to the PCB pads.

3.4.3. Sample Holders for GHz Frequencies

Within the scope of this thesis, a main objective was to reach and excite the sample with GHz electrical signals. A detailed description of the developed solution is shown in Chapter 6. In this section, only the modification for the sample holder and PCBs are shown. Two sub-miniature push-on (SMP)

connectors are soldered using UHV-compatible solders to a dedicated PCB for high frequency signals. The PCB is made like in previous versions from Rogers 4000 raw material, which provides adequate UHV compatibility (Fig. 3.12a).

The metal spacer under the PCB was machined to accommodate the additional SMP connectors. A new cap design has been proposed to allow for sufficient space for the SMP connectors which otherwise would collide with the end of the cap used previously (compare Fig. 3.12b). The modification was designed to keep the maximum possible cap-coverage of the sample and sample holder.

Fig. 3.12c illustrates the full assembly with the modified cap, the SMP-soldered PCB, and the sample mounted in the sample holder. Further details on PEEM measurements while applying signals to the samples are provided in Section 4.3.2.

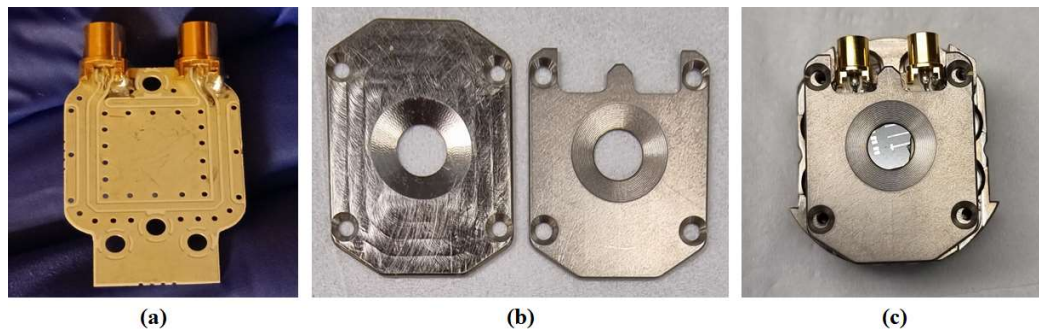


Figure 3.12. Display of modified parts to be employed for higher frequency signals. (a) PCB soldering to sub-miniature push-on (SMP) connectors. (b) Comparison in the geometry of standard (left) and modified (right) caps for the specific PCB. (c) Modified PCB together with the sample and cap mounted in the sample holder.

3.4.4 In-/Out-of-Plane Vector Magnet Sample Holder

Another activity, not directly linked with electrical signals, during this thesis, was the fabrication of a new special type of sample holder which can be used as a vector magnet combining in-plane and out-of-plane magnetic fields. It was

prepared and characterized, and is now being offered to regular users. It is shown in Fig. 3.13a.

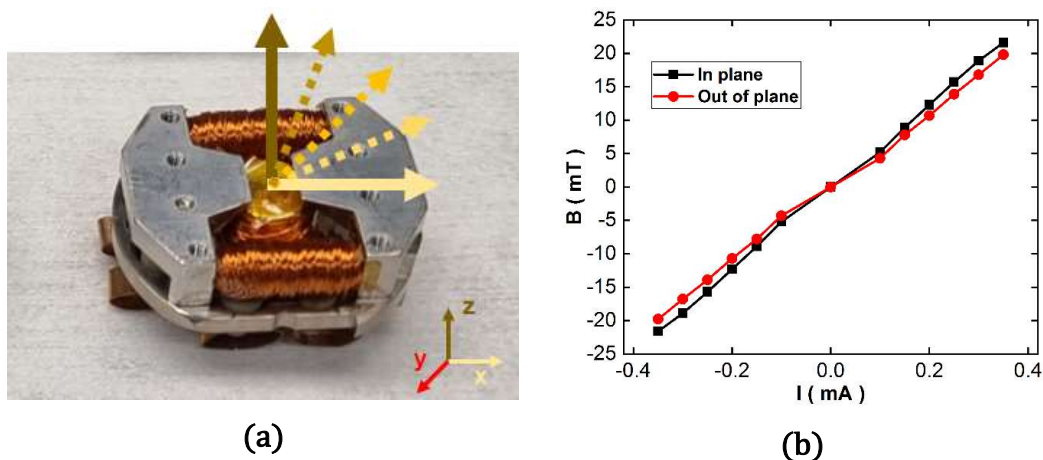


Figure 3.13. (a) Illustration of the new in-/out-of-plane sample holder. Different shades of yellow arrows depict the direction of the magnetic field from in-plane to out-of-plane of the sample. (b) Characterization of the sample holder in (a) showing the magnetic field as a function of applied current through both the coils. When using both coils in a suitable combination, any field angle in a plane containing the sample surface and normal can be achieved.

This sample holder, known as the in-/out-of-plane magnetic field sample holder, is capable of applying a magnetic field that can project either in-plane or out-of-plane relative to the sample. The geometry of the two yokes and the number of windings in each coil were designed to match the magnetic fields in both directions at equal current using three-dimensional OPERA simulation software suite of Dassault Systèmes (2018) [53]. This design allows the operation as vector magnet with the same two current sources in the Elmitec rack which are also used for the in-plane quadrupole sample holder. In our case, each side and the central cylinder have 400 turns, generating similar field strengths in both planes. The sample is positioned in the gap, supported by two edges of the spacer.

Fig. 3.13b displays a plot of magnetic field as a function of applied current, with the black and red lines representing the field along and out of the sample plane, respectively. The nearly identical values in both directions at similar current values validate our design.

CHAPTER 4

Chapter 4

MAGNETIZATION DYNAMICS DRIVEN BY SURFACE ACOUSTIC WAVES (SAW)

Tuning the magnetization in materials is considered to be an efficient way to enhance the properties of such materials for their applications in respective domains. Various methods are being investigated throughout the years in order to understand the mechanisms that take place within the materials during their optimizations. In this chapter of the thesis, various techniques have been presented that generate and control the magnetization dynamics in magnetic materials. Furthermore, an explanation towards imaging such dynamics is also presented in this chapter. This is divided into three parts. The first part is dedicated to the brief state of the art and the physics associated with different mechanisms causing dynamics in magnetization. In the second part, attention is drawn towards the understanding of the surface acoustic waves (SAWs) followed by the studies carried out to manipulate magnetization dynamics with the help of SAWs. The third part is focused on the experimental setup needed to combine SAW generation with X-ray photoemission electron microscope (XPEEM) imaging.

4.1 Magnetization Dynamics

One of the standard approaches for manipulating magnetization is the use of magnetic fields created by the flow of current through a coil. Nevertheless, in this case, a magnetic field tends to align the magnetization in the same direction as it results in a low-energy state of the system. However, low switching speed and higher consumption of energy are the vital issues that occur employing magnetic fields for magnetization manipulation. Therefore, for the last 20 years, attention has been devoted towards new methodologies and studies in order to manipulate magnetization and magnetic structures [54, 55]. An alternative to magnetic fields in manipulating magnetization is the spin of electrons in an electric current flowing through the magnetic material, and the mechanism is known as spin-transfer torque (STT) [56, 57]. In this mechanism, torque is produced by the spin-polarized conduction electrons into the magnetic layer due to the transfer process of angular momentum. With this, the magnetization of a ferromagnetic layer may be switched. Further, spin-orbit torque (SOT) [58, 59], consisting in an electrical current flowing through a bilayer made of a non-magnetic material with a strong spin-orbit coupling and a ferromagnet can produce a variation into the magnetization of the ferromagnet. A spin accumulation occurs at the interface layer caused by several spin dependent scattering (spin Hall effects [60]) in the non-magnetic material, thus causing the magnetization reversal at the ferromagnet. Some of the examples of exploiting SOT lead to develop MRAM [61], spin logic devices [62], and high-frequency microwave devices [63]. The switching process in both STT and SOT is governed by a precessional motion of magnetization described by the Landau-Lifshitz-Gilbert (LLG) equation [64]. Other means of controlling magnetization utilize ultra-short light pulses [65] and the thermal effects associated with it [66, 67].

Another promising approach to steer the magnetization in magnetic materials is by means of electrical fields which is dominant in developing energy-efficient spintronic devices [68]. Earlier studies have been carried out among ferromagnetic semiconductors among which magnetization has been altered due to carrier concentration modulated by electric field [69, 70]. Employing electric fields reduces power consumption and dissipation in

comparison with the use of magnetic fields. The effect of electrical fields on magnetic states are considerably weak in general but electrical fields may create strain and elastic deformations induce disturbances in the solid lattice, hence, resulting, in some cases, in the alteration of magnetic properties. Magnetostrictive systems are considered to be more encouraging in modifying magnetic states by non-magnetic means. Different studies have been carried out in which magnetic modifications have been induced by the elastic deformation due to electric fields in different material systems [71–75].

Magnetization dynamics can be probed using various techniques, including transport measurements with Anisotropic Magnetoresistance (AMR) [76], Magneto-Optical Kerr Effect (MOKE) [77], and X-ray-based methods. In transport measurements with AMR, changes in resistance due to magnetic field variations provide information about the magnetization dynamics. The AMR effect relies on the angular dependence of the resistance in a ferromagnetic material. Magneto-Optical Kerr Effect involves measuring the changes in the polarization of light reflected from a magnetic material as a function of the applied magnetic field, offering insights into the magnetization behavior. X-ray techniques, such as X-ray Magnetic Circular Dichroism (XMCD) [78] and X-ray Magnetic Linear Dichroism (XMLD) [75], utilize synchrotron radiation to study element-specific magnetic properties, providing a detailed understanding of the magnetic dynamics at the atomic level. These diverse approaches enable researchers to explore and characterize magnetization dynamics in a wide range of materials and conditions.

4.2 Magnetization Dynamics by SAW

4.2.1 Surface Acoustic Waves (SAWs)

SAWs are strain waves that propagate through the surface of material which exhibit elasticity (Fig. 4.1). The amplitude of these waves decays exponentially to the depth of the material, such that they are confined in height to about one wavelength [79].

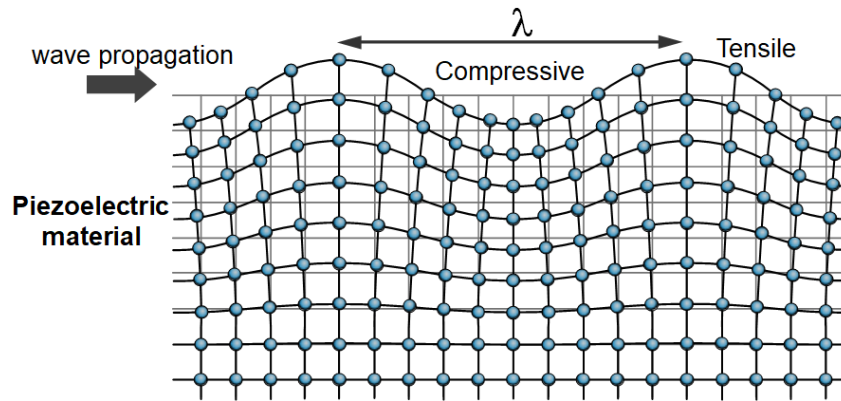


Figure 4.1. Schematic depiction with regions of compressive and tensile strain during propagation of a SAW through piezoelectric material [80].

The concept of SAW was initially explored by Lord Rayleigh in 1885, where he formulated its dispersion relation for isotropic elastic media [81]. However, practical applications did not emerge until 1965 when White and Voltmer showcased the generation and detection of SAW using interdigital transducers (IDTs) deposited on piezoelectric substrates like quartz or lithium niobate [82]. SAW can be categorized into various modes based on its polarization direction, including Rayleigh SAW (R-SAW) [83], shear-horizontal SAW (SH-SAW) [84], and Lamb wave [85]. In layered structures, additional waveforms such as Love waves, Sezawa waves, Stoneley waves, and others may exist [86].

Owing to its relatively low velocity (~ 3990 m/s for LiNbO_3) compared to electromagnetic waves and high sensitivity to frequency (up to the GHz range) [87], SAW devices initially found extensive use as filters and delay lines in telecommunication systems [88]. Subsequently, SAW technology evolved to serve as sensors for diverse physical quantities such as temperature, pressure, strain, and mass [89]. The functionality of the SAW devices depends on factors such as input power and frequency of electrical signals, geometry and material of SAW devices and substrates. SAW devices also find application as actuators, enabling the control of microfluids, microdroplets, and particles in fluids.

SAWs can be generated by depositing IDT electrodes on the surface of a piezoelectric material. These IDTs are excited by radio frequency electrical signals; hence, the electrical energy is converted to mechanical energy. This phenomenon is known as actuation [90]. The frequency of the waves is defined

by the spacing d between the fingers of the IDTs, corresponding to the formula $f_{SAW} = n \frac{v_{SAW}}{d}$, where “ n ” corresponds to different harmonics and “ v_{SAW} ” is the propagation velocity of SAW in specific material. The SAWs are generated if the radio frequency of the generator matches the resonance frequency of the IDT, thus, the waves are launched and may travel in distance up to millimeters. A piezoelectric voltage is also accompanied with these waves that propagate along the material’s surface. This will be illustrated in detail in the upcoming chapters. SAWs can be used in electronics due to their capability of transforming centimeter wave in free space to micrometer scale in a chip.

4.2.2 Magnetization Dynamics by SAWs – State of the Art

In magnetic systems, SAWs are considered to be a possible effective tool that induce magnetization dynamics with less power dissipation within the system. The coupling occurs by the phenomenon of inverse magnetostriction (Villari Effect), also known as magneto-elastic effect, i.e. the change in magnetic properties (mostly anisotropy) due to strain [13, 91–96]. Magnetization dynamics due to SAWs have been investigated for long time and clear modifications in the magnetic states have been observed [97–106]. Alternatively, there have been studies showing changes in the SAW propagation induced by magnetization dynamics [107–110]. In the context of the effect of the magnetization on the SAW transmission, a nonreciprocal behavior of the SAWs has been established in various ferromagnetic, semiconductor [111] and dielectrics heterostructures [112] as well as in synthetic antiferromagnets [113]. SAWs have also been used to modify static magnetic structures such as controlling magnetic domain walls in thin films with perpendicular magnetic anisotropy [114]. Other examples of the use of SAW for controlling dynamics of magnetic properties of materials include SAW-assisted skyrmion creation in asymmetric stack [115], their dynamics in ferromagnets [116], and antiferromagnets [117]. From the practical perspective, SAWs have been used to promote switching in ferromagnetic films [103] or nano-elements [118], to generate magnetization rotations in ferromagnetic bars [119], to assist in

magnetic recordings [120], and to modify exchange bias in magnetic field sensors [121].

Another promising approach is the generation of magnetization waves by SAW, also termed as magneto-acoustic waves, which provide a link to the field of magnonics [122]. Studies have been carried out to drive ferromagnetic resonances elastically due to SAWs [99], thus, reforming the usual mechanism of rf electromagnetic field-induced deformations. Recently, SAWs have been induced in the piezoelectric LiNbO₃ substrate that excited magneto-acoustic waves in ferromagnetic Ni thin film [94]. The long-range propagation of such waves directs towards the strong coupling of elastic deformations with the magnetization. In this study, not only SAWs but also the magneto-acoustic waves were imaged by employing the XPEEM.

Imaging of SAW can provide information about acoustic properties of materials. Amplitude and frequency response can be extracted from measurements studying conversion of electrical signals into acoustic vibrations. Information about the process of SAW excitation and propagation in solids can be assessed from direct imaging techniques such as X-ray diffraction [123], topography [124], the scanning electron microscopy method [125], or Transmission-Mode Microwave Impedance Microscopy [126]. By employing XPEEM, we can visualize SAW and quantify the associated electric signal, obtaining a value for the SAW-generated strain, both in time and space [127]. The methodology of imaging SAWs is explained in the next section of this chapter.

In a similar way, information about the interaction between acoustic waves and magnetization can be extracted from indirect measurements of either magnetic or acoustic properties of materials. An example would be the acoustic absorbed energy of an acoustic signal as a function of the magnetic state [98, 99]. Direct detection and imaging of magneto-acoustic signals is thus interesting and the available different techniques offer a variety of challenges and opportunities. Some of the used techniques are MOKE [95], MFM [128], XPEEM [13], and STXM [129].

4.3 Experiments with SAW in XPEEM

The main focus of this thesis is the measurement of magnetization dynamics driven by SAWs in XPEEM into the GHz regime. To start with, the following section explains how experiments with SAWs are performed in the PEEM microscope. The topics covered include the sample and sample holders, the timing method (synchronization), as well as the contrast mechanism of the SAW in the direct PEEM image.

4.3.1 Excitation of SAW by IDTs

For observing the magnetization dynamics in ferromagnetic Ni and Co, black-LiNbO₃ substrates (128° Y-cut) [130] were used, as they provide the best SAW properties. For antiferromagnetic CuMnAs films, GaAs, which is a weak piezoelectric in the [110] crystalline direction, was used as it allows epitaxial growth of the CuMnAs. IDTs, 10 nm Ti, 40 nm Al, 10 nm Ti, with fundamental frequencies from 125 MHz – 1 GHz were prepared by collaborators at the Paul Drude Institute in Berlin by optical and e-beam lithography (see Fig 4.2a for example). Using harmonics of the fundamental frequencies, different SAW frequencies can be synchronized with the synchrotron light. While all harmonics work equally efficient in the 100s of MHz regime, above 1 GHz, the IDTs are only tuned for one specific harmonic due to the non-linear dispersion relation of LiNbO₃, i.e. the change in the sound velocity. An adaptation to the XPEEM requirements is the increased distance (6 – 8 mm) between the IDTs which allows to keep the wire bond contacts far away from the region of measurement.

IDTs can be electrically characterized by network analyzer which measures the reflected electrical RF power at the device (S_{11}) or the transmitted electrical power (S_{12}) between two opposing IDTs when used in a two-port configuration. Fig. 4.2b depicts the characterization of a pair of IDTs. The IDTs are designed to have first harmonic at 125 MHz and show resonances at the multiples of 125 MHz. The firm contact of the IDTs is affirmed with the sharp peaks in S_{12} at harmonics of 125 MHz, demonstrated with the black curve in Fig. 4.2b.

This type of measurement can be performed when proper high frequency contacts are available to the sample. However, some XPEEM experiments are conducted with lower bandwidths cables or with only a single IDT. In this case, it is still useful to confirm the proper connection and operation of the device inside the microscope with the network analyzer. Typical data obtained in these conditions is shown in Fig. 4.2c. The black curve shows the transmitted signal through the IDTs and the blue curve depicts the reflecting signal. Although, the signals are missing strong peaks at resonance, the wiggles in both the curves in proximity to a resonance frequency indicate the working connection.

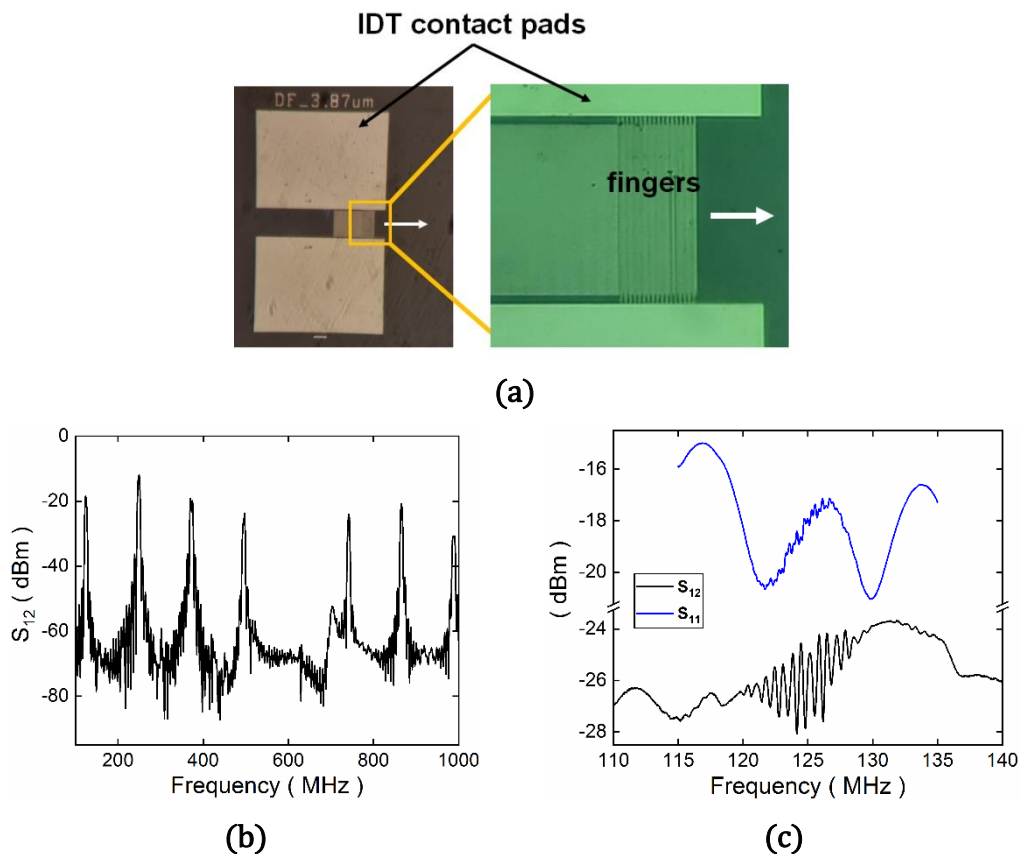


Figure 4.2. (a) The left side shows an IDT device with the contact pads. The right side displays the magnified area in the yellow box of the left side showing the fingers (antennas) which generate the SAWs, in the direction of white arrow. (b) Electrical characterization of IDTs on a LiNbO_3 substrate: Reflection in blue (S_{11}) and transmission in orange (S_{12}) as a function of frequency. The wiggles in both signals at 125 MHz shows the first harmonics of the resonant frequency. (c) Characterization of an IDT in transmission (S_{12}) inside the microscope depicting the proper and improper contacts in red and black, respectively.

4.3.2 Sample Holder and Mounting

For XPEEM imaging, samples are mounted in specific sample holder to be loaded in the microscope (Fig 4.3a). It includes a printed circuit board (PCB) that provides a platform to contact the IDTs with the wire bonds. The sample is covered with the cap, as shown in Fig. 4.3(b-c) to avoid the unnecessary part of the sample being exposed to the beam. The cap has a hole of diameter 3 – 8 mm that allows to image the sample. The cap has to be raised slightly above the sample to circumvent the wire bonds contacting the sample. Because of the raising of the cap, we face two experimental complications. The first is a region of shadow on the sample where X-rays are blocked by the cap, and therefore no electrons are emitted. The second is an imaging artifact due to an electrostatic lens effect which is illustrated in Fig. 4.3d. In practice, electrostatic lens effect proved to be more limiting than the shadow.

In Fig. 4.3d, the curved-red line depicts the wire bond which is being covered by the cap (blue line). The wire bond should be as low as possible to avoid a short-circuit with the cap. It is favorable to mount the cap as low as possible to minimize the electrostatic lens effect. When the X-rays fall on to the surface of the sample, the photoelectrons produce secondary electrons which leave the surface of the sample and follow various trajectories (light orange arrows). If the distance between the cap and sample is relatively higher, X-rays are blocked from reaching the sample and thus, shadow is formed on the sample. This is illustrated in Fig. 4.3d as black region on sample. The electrostatic lens effect occurs when the point of interest is not sufficiently centered inside the hole of the cap. The emitted secondary electrons from the sample surface are deviated from their normal path due to the edges of the cap, which form another ring electrode at the same potential like the sample. The raised cap distorts the electric field which normally is only defined by the sample and the objective lens and results in a tilt-like effect on the image, which can be too large to be corrected. This electrostatic effect can be minimized in the following way: mounting the sample with the region to be imaged (not the substrate) as centered as possible in the cap; reducing the loop of wire bonds to the least possible height that allows to lower the cap.

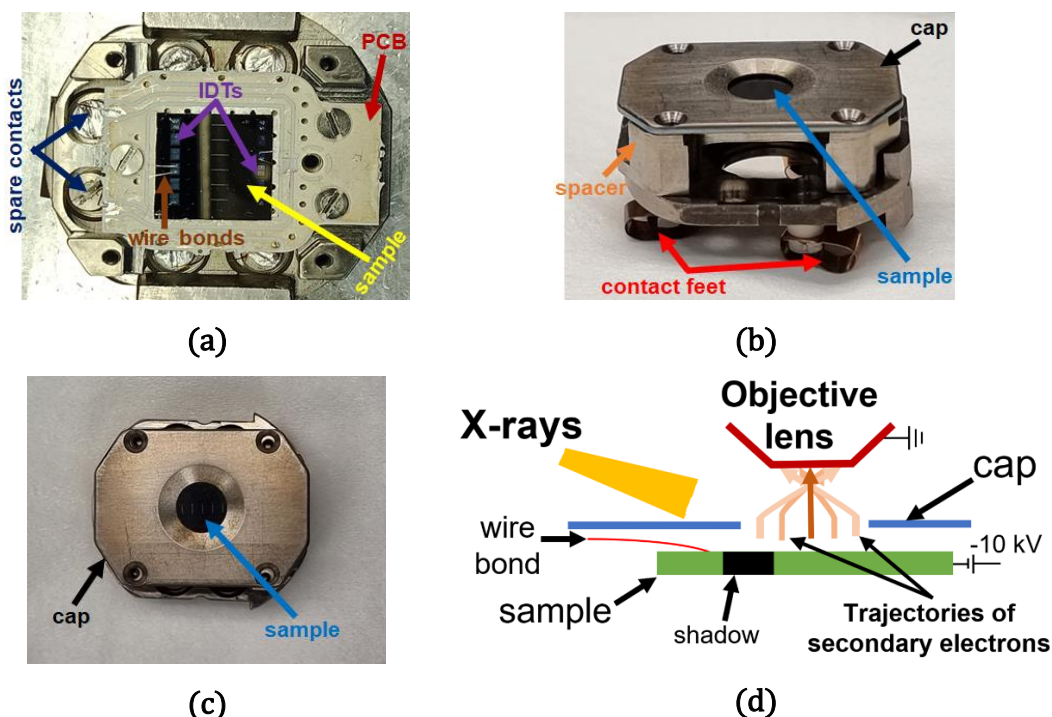


Fig. 4.3. (a) Depiction of sample mounted on PCB within sample holder. Purple arrows denote the IDTs whereas brown arrow specifies wire bonds. For the electrical connections up to 500 MHz, two standard electrical contacts at the top of the sample holder are used (“spares”). The airside cable from the PEEM to the main electronic rack has been modified to a coaxial standard while the UHV standard feed-throughs are kept. The improved version for GHz signal is discussed in detail in Chapter 6. (b) Side-view of the sample holder illustrating contact feet and spacer on which the PCB rests. (c) Top-view of the sample holder together with the cap covering the sample. (d) Schematic illustration of electrostatic lens effect which produces imaging artifacts due to the cap edges. The black area represents shadow which is formed when the cap limits the path of X-rays from illuminating the sample.

Another challenge for the SAW experiments in XPEEM is that the substrates are typically insulators and are charging under the X-ray beam. The measures to mitigate sample charging are the use of a reduced beam flux in comparison to usual operating conditions, adding additional ground electrodes on top of the sample, and working at negative sample bias voltages.

Since the operation of XPEEM microscope is performed with an accelerating voltage (10 – 20 kV), there exists a high possibility of arcs between the sample and the objective lens. These arcs can damage the sample, IDTs or the electronic

components connected to it. The probability of arcs is reduced by operation at relatively less accelerating voltage, i.e. 10 kV, together with an increased distance between the objective lens and the sample. This operation is performed at the expense of the spatial resolution of the microscope reducing from the benchmark 20 – 30 nm to about 50 – 60 nm, though, sustaining the safety of the sample. Additionally, samples are degassed in ultra-high vacuum at moderate temperatures for at least two hours using a conventional halogen lamp through a view-port before experiments.

4.3.3 Synchronizing Electrical Excitations with X-rays

The X-ray pulses obtained from the Alba Synchrotron are of approximately 20 – 30 ps length with the repetition rate of 2 ns in multi-bunch mode. At the origin of this time structure are the RF accelerating cavities for the electrons, which operate at 500 MHz. Even for more complex filling patterns, like hybrid mode, the necessary condition of any electron bunch to be in phase with the 2 ns repetition sequence remains. With the pulses of synchrotron, we can thus acquire time-resolved measurements (stroboscopic measurements) much faster than the typical time response of the microscope if the sample excitation is synchronized with the photon pulses.

In order to generate such oscillatory signals, a Keysight EXG Vector signal generator (RF generator) is utilized to capture the synchrotron master clock (phase-lock loop, PLL) from a digital signal distributed by optical fiber. The RF generator produces a phase-synchronized analog sinusoidal signals with adjustable phase and power between 1.115 MHz (ALBA orbit clock) and 1 GHz. The analog signal from the RF generator is then further transmitted via an optical fiber link, designed at ALBA [131], into the PEEM high-voltage rack where it is converted back to an electrical signal. Depending on the desired signal, different treatment such as pre-amplification, filtering and frequency multiplication is performed at low level before the final, universal high-power amplifier. Optical communication system is designed in such a way that transmission of the signal through the sample can be measured as well. The schematic illustration of the scheme is presented in Fig. 4.4.

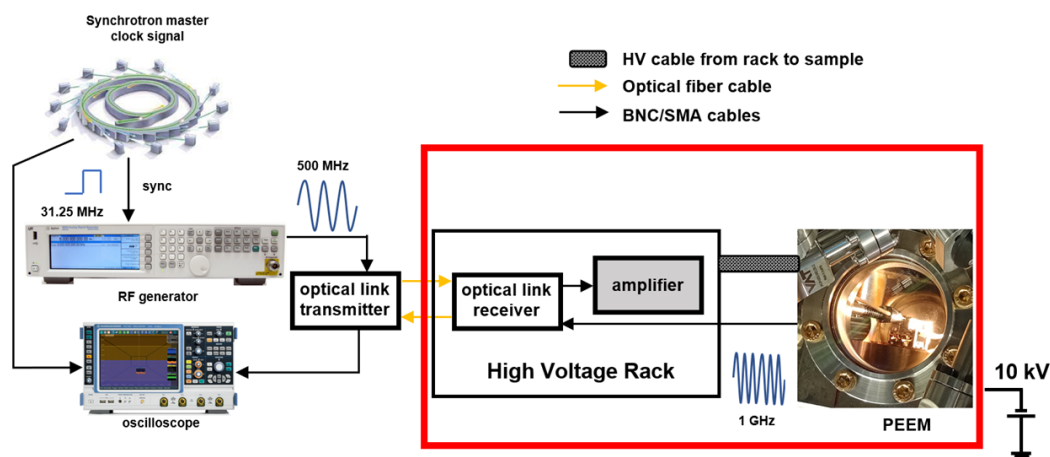


Figure 4.4. Illustration of the scheme to apply electrical excitation (SAW) to the samples in the XPEEM synchronized with X-rays beam.

The signal arrives to the sample via one of two possible coaxial cable systems. The first uses the standard DC-type feedthroughs connected to a coaxial cable and works with considerable losses until about 500 MHz. The second was designed, built and used during this thesis, and circumvent the standard feedthrough with a dedicated high frequency connection which allows operation until at least 4 GHz (Chapter 6).

To carry out the time resolved measurements, samples have to be excited at a specific phase with respect to the stroboscopic synchrotron light pulses. With the photon pulses at 500 MHz, excitations with $n \times 500$ MHz can be used, where “n” corresponds to integer values of 1, 2, 3.... Additionally, fractional frequencies can be used either with a custom hybrid mode filling pattern [132], or with a recently installed electron gating setup [133]. The gating consists in a small parallel-plate capacitor introduced in the photoelectron beam path in the imaging column which can deflect the photoelectrons with high speed. Deflected electrons are then blocked by the contrast aperture. With this technique, one can observe excitations at frequencies that follows the relation: $\frac{n}{m} \times 500$ where “n” denotes integer values and “m” corresponds to 2, 4, and 7, ... (dividers of the Alba bucket number 448). With this device, stroboscopic data collection is possible in the range of 1 MHz – 250 MHz with standard multi-bunch filling pattern.

4.3.4 SAW Contrast and Amplitude in XPEEM

In order to quantify the magnetoelastic effect driven by SAW, it is necessary to know the SAW mechanical amplitude and thus, the strain applied to an overlayer. The SAW amplitude can be determined in XPEEM from the surface potential variation. Fig. 4.5a shows the direct XPEEM image of the synchronized 1 GHz SAWs in LiNbO₃ at the bias voltage (V_b) of -2.8 V under the pulsed synchrotron X-ray illumination. A clear SAW contrast is evident in the form of stripes spaced by 4 μm in the sample when imaged with synchronization between SAW and the X-ray illumination. The dark region on the top shows the magnetic Ni where no contrast is visible. The dark and bright stripes reflect the SAW wavelengths. The obtained contrast is independent of the X-ray energy and polarization. Instead, it is dependent on the V_b applied to the sample which corresponds to the nominal (neglecting charging) secondary electron kinetic energy. By changing the V_b , a gradual change in the contrast is observed.

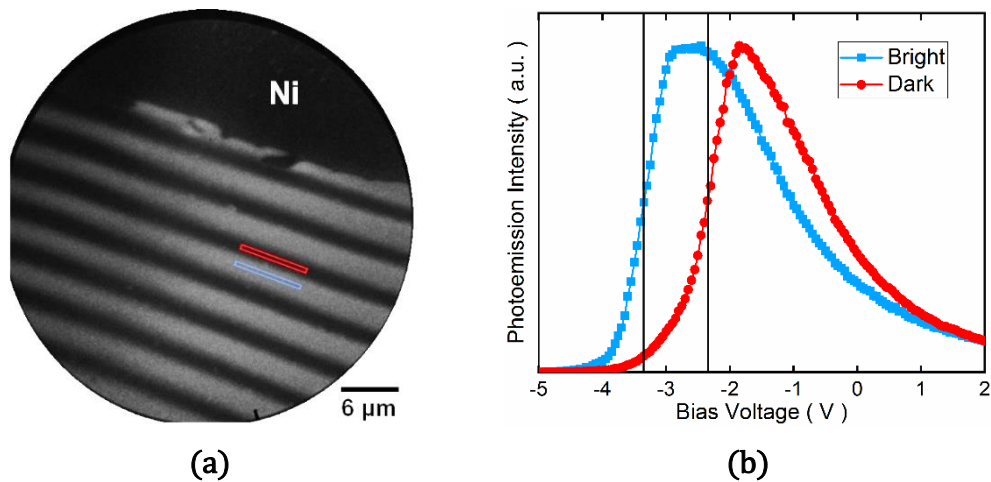


Figure 4.5. (a) XPEEM image of SAW in LiNbO₃ at 1 GHz at bias voltage -2.8 V. (b) Determination of the SAW electrical amplitude in the XPEEM field of view. The average intensity (emitted secondary electrons) of the blue and red boxes in (a) is shown as function of the sample bias voltage (nominal electron kinetic energy).

In Fig. 4.5b, we plot the profiles extracted from the Fig. 4.5a, which shows the spectra corresponding to blue and red boxes, and plot them as a function of V_b . Since all the parameters are similar in the measured region (photon flux, SAW

amplitude), we refer this shift of the emission spectrum to local SAW phase, which is the local piezoelectric surface potential accompanying the SAW deformation waves (Fig. 4.6). The shift of photoelectron spectra corresponds to the electrical amplitude of the SAWs, e.g. by comparing the midpoints of the onset (black lines on both the spectra (Fig. 4.5b)). The measured voltage difference in the field of view of the XPEEM is lower but proportional to the SAW excitation amplitude applied to the IDTs. This method does allow the determination of the real SAW amplitude to which the sample, for example, a magnetic layer, is exposed.

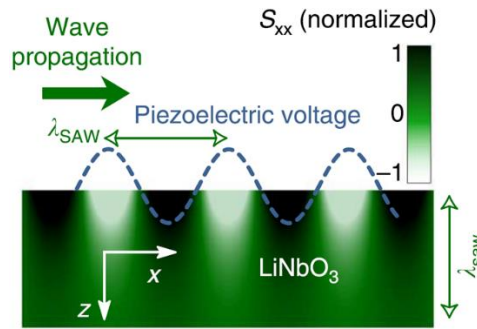


Figure 4.6. Schematic illustration of the in-plane strain induced modulation in the LiNbO_3 caused by the SAW. The blue dashed oscillations show the oscillating piezoelectric voltage modulation [13].

Starting from the electric amplitude, then the strain tensor components, can be determined through the numerical solution of the coupled differential equations governing the mechanical and electrical displacement, which is applied to an acoustic wave propagating in the x-direction of the LiNbO_3 substrate. The calculations have been performed by the collaborator at Paul Drude Institute, Berlin, Germany. In order to acquire surface modes, solutions are sought that are characterized by decay towards $z > 0$, while satisfying the stress and electric displacement boundary conditions at the surface ($z = 0$). Similar SAW wavelength, as in the experiment, is employed and power density is selected such that the amplitude of the simulated piezoelectric potential at $z = 0$ aligns with the measured value. In short, by measuring the surface potential induced by the SAWs locally, the local strain can be calculated precisely [134]. For the electrical amplitude of 1.0 V in the example of Fig. 4.5a, the corresponding strain value of the dominant component $\epsilon_{xx} = 14.3 \times 10^{-5}$.

CHAPTER 5

Chapter 5

SUMMARY OF RESULTS

Stroboscopic XPEEM measurements have been used to observe magnetization dynamics in thin magnetic films induced by surface acoustic waves (SAW) in the piezoelectric substrates. This work is based on previous reports of magneto-acoustic waves in Ni at 500 MHz [94]. The present work extends the method successfully to new domains of interest, i.e. new materials and higher frequency range. In [Paper 1](#), we excited and observed for the first time Néel vector waves in antiferromagnetic CuMnAs by generating SAW of 500 MHz in a GaAs substrate. The X-ray magnetic linear dichroism (XMLD-PEEM) was exploited to obtain the contrast. We were able to show that the efficiency of the magneto-acoustic wave excitation in the antiferromagnet is comparable to ferromagnetic systems (Ni). [Paper 2](#) is a technical work directed towards the instrumentation development of a new setup that is able to excite the samples with higher frequency signals and ultrashort-current pulses, overcoming the limitations which have been encountered in the old existing setup. In the [3rd Paper](#), we performed the successful operation of the setup that has been developed. We excited magneto-acoustic waves in ferromagnetic cobalt and nickel thin films at frequencies up to 3 GHz. From the induced XMCD wave patterns, we determine the magnetoelastic coupling constants. Due to the large Co magnetization creating dipolar fields, the magnetoacoustic wave amplitude is smaller than in Ni. A reduction of the coupling efficiency is observed for Ni at

3 GHz compared to 1 GHz which hints at the ultimate speed limit of the magneto-elastic coupling for this type of heterostructures.

Paper 1: The 45 nm thin epitaxial films of antiferromagnetic CuMnAs were grown on the lattice-matched GaAs substrate using molecular beam epitaxy [135] by the collaborators from University of Nottingham, UK. The IDTs for SAW generation were prepared through electron beam lithography and metal evaporation with a finger periodicity of 5.73 μm by collaborators from Paul Drude Institute, Berlin, Germany. The deposited thin CuMnAs film has been characterized using X-ray diffraction (XRD) which confirms the tetragonal crystal system (P4/nmm) of CuMnAs (Fig 5.1a). We performed the X-ray absorption spectroscopy (XAS) measurement of the thin film, at the temperature of $T \approx 235$ K, using XPEEM, and the X-ray magnetic linear dichroism spectrum (XMLD) was obtained by subtracting the spectra at linear horizontal and vertical polarization (Fig. 5.1b). The acquired XMLD spectrum at Mn $L_{3,2}$ edges is similar to the one obtained in [136] and the magnetic features are highlighted with the black boxes.

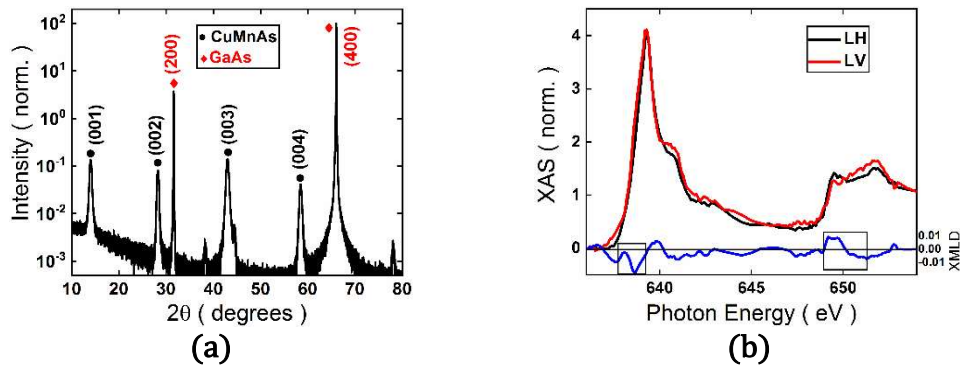


Figure 5.1. (a) XRD measurements of 45 nm thin film of CuMnAs on GaAs showing the film (black) and substrate (red) peaks (b) XAS and XMLD spectra of CuMnAs/GaAs at the Mn $L_{3,2}$ edges, obtained with horizontal (black) and vertical (red) linear polarization.

SAWs were generated at the frequency of 500 MHz in the GaAs substrate to observe the dynamics due to the magnetoelastic effect in the CuMnAs film. To detect changes in the domain configuration, we compared XMLD images at opposite phases of the SAW. Any significant contrast obtained by subtracting

those images would indicate a change of the domain configuration due to the magnetoelastic effect, which were negligible or below the detection limit in this study. This absence of changes is attributed to the presence of intrinsic pinning due to the film microstructure. However, small collective oscillations of the Néel vector, i.e. Neel vector waves, are observed and quantified at different temperatures. The maximum amplitude of the Néel vector waves was measured at room temperature (Fig. 5.2c) while being reduced at lower temperatures (223, and 233 K), which indicates an increase in the energy barrier for the spin axis rotation with lower temperatures.

We obtained an image of the Néel vector waves when directly averaging all the difference images after shifting them along the SAW propagation direction by the number of pixel corresponding to the nominal SAW phase ψ_i . Fig. 5.2d shows the resulting image for the data set at room temperature, which shows the largest rotation and contains most individual measurements for improved statistics.

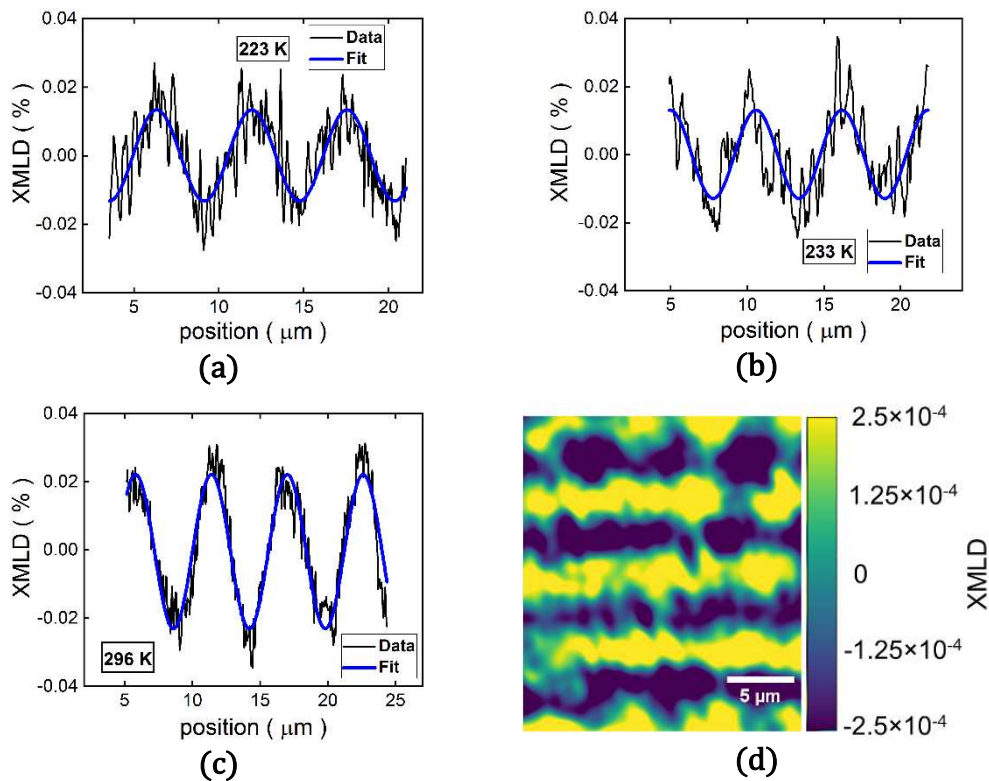


Figure 5.2. Néel vector wave (spin axis rotation wave) in CuMnAs observed by XMLD-PEEM. XMLD signal (in %) at $T \approx 223$ K in (a), $T \approx 233$ K, in (b) and $T \approx 296$ K in (c). The black line in each plot shows the data and the blue line is the

sinusoidal function curve fitted to the data points. (d) Visualization of the Néel vector wave in CuMnAs: average of all XMLD phase difference images at room temperature after shifting them along the SAW propagation direction to accommodate for the electronic phase shift of the SAW. Yellow and purple colors denote a positive or negative dynamic XMLD as indicated by the color scale.

The efficiency (Neel vector rotation in degrees/strain) has been calculated for all the cases and found to be maximum at room temperature, i.e. $3.26^\circ/\text{strain} \times 10^{-4}$. Studies on ferromagnetic materials Ni [94] and Heusler alloy Fe₃Si [14] found similar efficiencies of 2 – 4.5 (Ni) and 1.6 – 4.1 (Fe₃Si). Thus, the dynamic magnetoelastic effect in CuMnAs induced by SAW is sizable and comparable inefficiency to ferromagnetic materials. This is illustrated in Fig. 5.3. Note that since the applied magnetic field has a big influence on the magnetoacoustic wave amplitude in ferromagnets, ranges rather than single values are given.

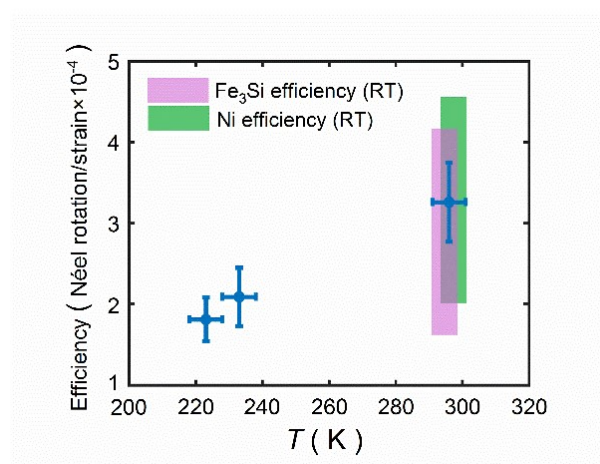


Figure 5.3. Efficiency of the wave excitation in CuMnAs as a function of temperature in comparison with all data at 500 MHz SAW. The area for ferromagnetic samples corresponds to Ni and Fe₃Si at room temperature (RT) and covers the range between zero external field and resonance.

Paper 2: The new high frequency (HF) setup is developed in such a way that it is being compatible with the existing XPEEM setup and the UHV system at the Alba synchrotron facility. The aim of this setup is to excite the samples up to GHz frequency range, e.g. to observe the dynamical effects at the intrinsic ferromagnetic resonance frequencies of the materials. This setup also extends to apply electric current pulses to the samples to visualize the ultrafast domain

wall velocities in magnetic nanowires and skyrmion motion. The HF setup is based on the sub-miniature push-on (SMP) connection scheme with the sample holder inside the XPEEM chamber, shown in Fig. 5.4. The design of the HF setup is a Y-shaped assembly having electrical vacuum feedthrough SMA (sub-miniature version A) and wobble stick to engage and disengage the plug inside the microscope with the sample holder. The connection between the plug and the feedthrough is made with the coaxial Teflon isolated cables that has better flexibility and mitigate the electrical losses in comparison to standard coaxial cables. Inside

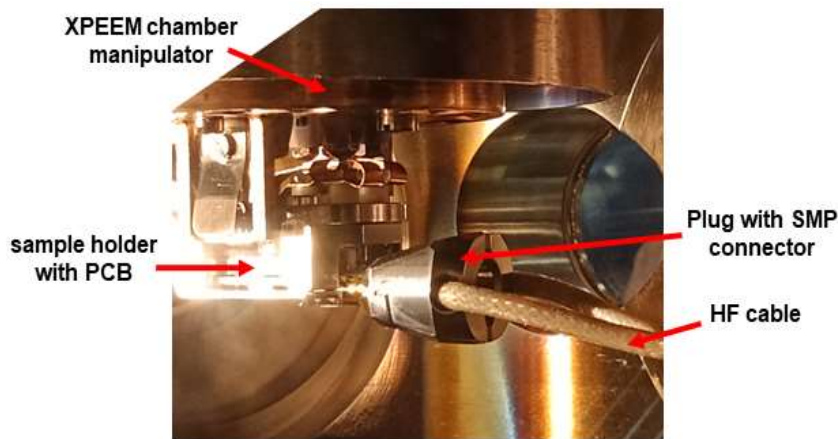


Figure 5.4. Connection scheme between the sample holder and the high frequency cable inside the XPEEM chamber. The cable provides a signal path to the sample through a plug that contains two SMP connectors [52].

the HF setup, a set of polyether ether keton (PEEK) insulators are located at different points to avoid any contact between the Teflon insulated cable and the inner metallic walls of the HF setup. The sample holder has also been modified to make it compatible with the new setup connection scheme. The printed circuit board (PCB), on which the sample lays and being contacted, is soldered with the SMP connectors that enable the plug to make a connection with the sample. With this, the cap design to cover the unnecessary region on the sample has been also modified to compensate the SMP contacts on the PCB.

The electrical characterization of the HF setup is performed for both the types of excitation schemes that will be employed. Fig. 5.5a depicts the electrical transmission (S_{12}) vs frequency measured with the network analyzer.

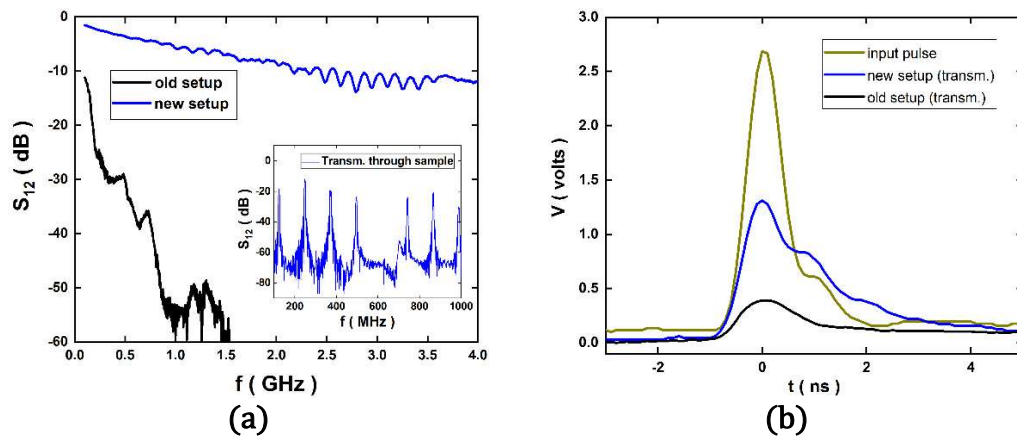


Figure 5.5. (a) HF signal transmission through the new (blue) and old (black) setup. Inset: characterization of a LiNbO_3 sample SAW transmission filter inside the PEEM sample stage. (b) Output comparison of transmitted nanosecond current pulses through a 50 Ohm load for both setups [52].

The black line shows the S_{12} signal employing the old setup (standard coaxial connection scheme) which portrays significant signal attenuation from comparatively low frequencies on. In contrast, the blue line represents the transmitted signal using the new HF setup, which clearly illustrates the enhancement in the signal efficiency arriving to the sample. The inset of Fig. 5.5a shows the S_{12} signal through a sample of lithium niobate (LiNbO_3) with a SAW transmission line as used in our experiment. The sharp peaks at the resonance frequencies of the IDTs are clearly visible which were completely diminished while measuring in the old setup. In Fig. 5.5b, short electrical current pulses transmitted through the new and old setup are compared. For a pulse of 1 ns duration, some broadening with respect to the original signal but a clearly improved amplitude (blue line) is obtained compared to the old setup (black line). To apply the electrical excitation signals (sinusoidal or short pulses), different electronic setups have been developed from modules.

This work also characterizes the performance of a new setup in terms of the spatial resolution in XPEEM, which has been reported in the 30 nm range under optimum conditions [50]. Various factors such as electron optics quality, apertures and alignment, sample mechanical stability, detector sensitivity, and space charge can limit the resolution. However, for experiments involving electrical contacts on the sample surface, such as electrodes or IDTs, a reduced

accelerating field (about factor 3-4) is typically used. It is achieved by reducing the high voltage to 10 kV and increasing the sample distance from the objective lens. This setting compromises between image quality and the reduction of arcs which can destroy the electrode structures on the sample. Arcs are more likely to occur due to non-flat surfaces, insulating regions, and degassing elements. Contacted electrode structures on the sample are often destroyed by the first arc event, possibly due to transient potential difference between different areas of the sample. The spatial resolution for the new setup with the reduced field setting was measured by imaging a defect in a Co layer grown on Si substrate (Fig. 5.6a). The spatial resolution defined as 15-85% edge jump was determined to be 56 nm from the line profile (Fig. 5.6b), which is equivalent to the standard manipulator under these conditions, i.e. showing no reduction due to the HF connection including lateral cables.

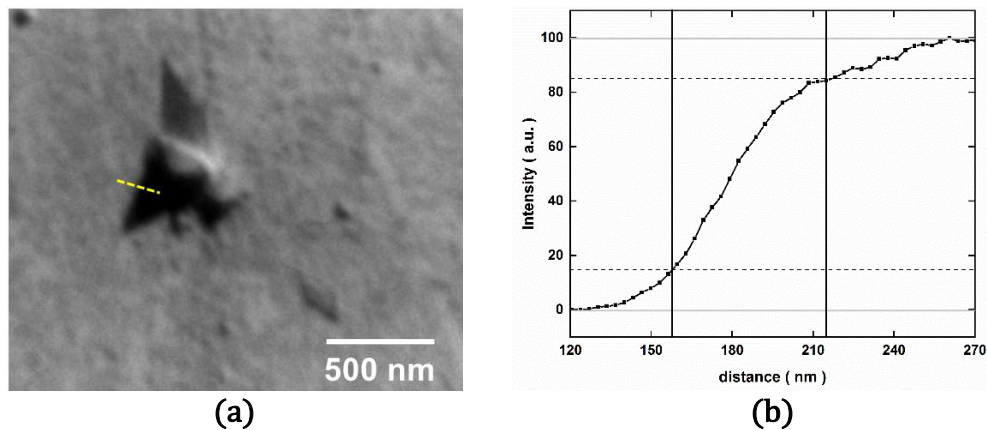


Figure 5.6 (a) XPEEM image, obtained with HF cable connected, of a defect on a Co/Si sample at reduced acceleration voltage (10 kV) and increased sample objective distance; typical for experiments with injected electrical signals, taken at 777.8 eV photon energy and 1 V start voltage. **(b)** Profile along the dashed yellow line in (a). The width of the grey box is 56 nm [52].

Paper 3: This work deals with the investigation of the magnetoelastic effect (ME) by X-ray photoemission electron microscopy (XPEEM) at higher frequencies (1-3 GHz) in hybrid piezoelectric-magnetic systems. For this purpose, 20 nm thin films of Ni and Co were grown on the 128° Y-cut piezoelectric LiNbO₃ substrate by e-beam evaporation. These films were grown within the acoustic path of the interdigital transducers (IDTs), which have been

designed to generate surface acoustic waves (SAWs) at 1 and 3 GHz in the case of Ni and 1 GHz in the case of Co. The coupling of the SAW with the magnetization of the films at various angles was characterized by acoustic-ferromagnetic resonance (a-FMR) using a network analyzer. In contrast to conventional ferromagnetic resonance, here the transmitted signal (S_{12}) attenuation varies due to the magnetization precession driven by the strain field of the SAW. This implies that more energy is absorbed by the magnetic system in the resonance condition when the SAW frequency matches the intrinsic FMR adjusted by the external magnetic field. Fig. 5.7 shows the attenuation of SAW in both the samples at 1 GHz. In Ni (Fig. 5.7a), the maximum attenuation is observed at $\pm 45^\circ$ angle between SAW and the external magnetic field (2–3 mT) where the ME torque is largest. With the decrease or increase of the angle, the ME torque reduces and reaches minimum values at 0° and 90° . However, the attenuation in Co is observed to be maximum at the angles of $\pm 30^\circ$, and declines promptly above these angles, as depicted in Fig. 5.7b.

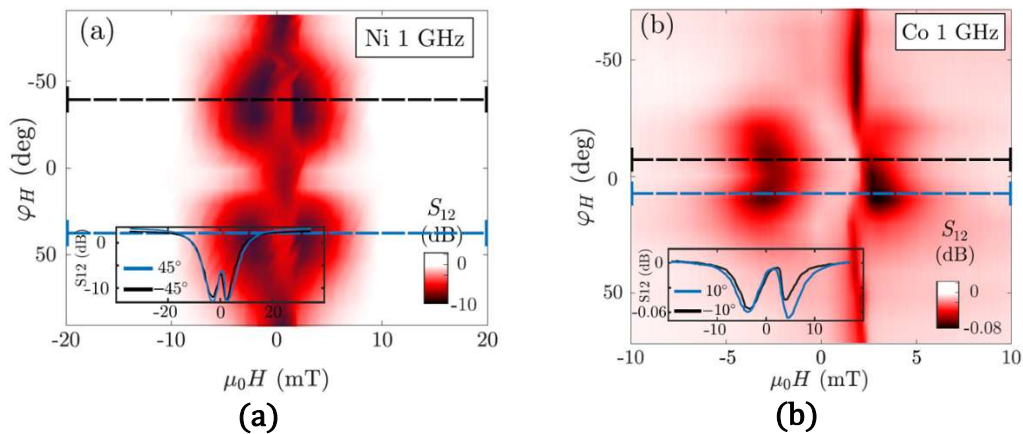


Figure 5.7. (a) Ni S_{12} attenuation at 1 GHz for several angles between the SAW and the magnetic field showing different absorption values with a maximum close to 45° and minimums at 0° and above 60° . The inset shows a horizontal cut of S_{12} attenuation for $\varphi_H = 40^\circ$ (black curve) and $\varphi_H = 30^\circ$ (blue curve). (b) Co S_{12} attenuation at 1 GHz for several angles between the SAW and the magnetic field. Co shows absorption when the SAW and the magnetic field are at an angle between -30° and 30° . The insets show a horizontal cut of S_{12} for $\varphi_H = 40^\circ$ (black curve) and $\varphi_H = 30^\circ$ (blue curve).

Imaging of the magnetoacoustic waves (MAW) was performed in the XPEEM by subtracting XMCD images for opposite SAW phases. With such technique, the magnetization dynamics due to SAWs can be observed more clearly, as the static contrast is eliminated and the dynamic contrast enhanced. The amplitude of MAWs is measured in the obtained images. In order to determine the SAW strain amplitude, the secondary electron energy in LiNbO₃ is used to measure the associated electrical oscillation which allows to calculate the strain components by solving the coupled elastic and electromagnetic equations which were comparable for all three cases discussed in the following. In the case of Ni, the SAW was excited by 1 and 3 GHz frequency signals. An example of SAW together with MAWs in Ni at both the excited frequencies is illustrated in Fig. 5.8a. The amplitude of MAW normalized to the full XMCD contrast (thus to M_s) as a function of the magnetic field is presented in Fig. 5.8b which clearly shows that the overall magnetization amplitude at 3 GHz is 1 order of magnitude lower than the one at 1 GHz. Also, in the case of Co at 1 GHz (Fig. 5.8d), the normalized amplitude signal is relatively smaller (two orders of magnitude) than for Ni at the same frequency.

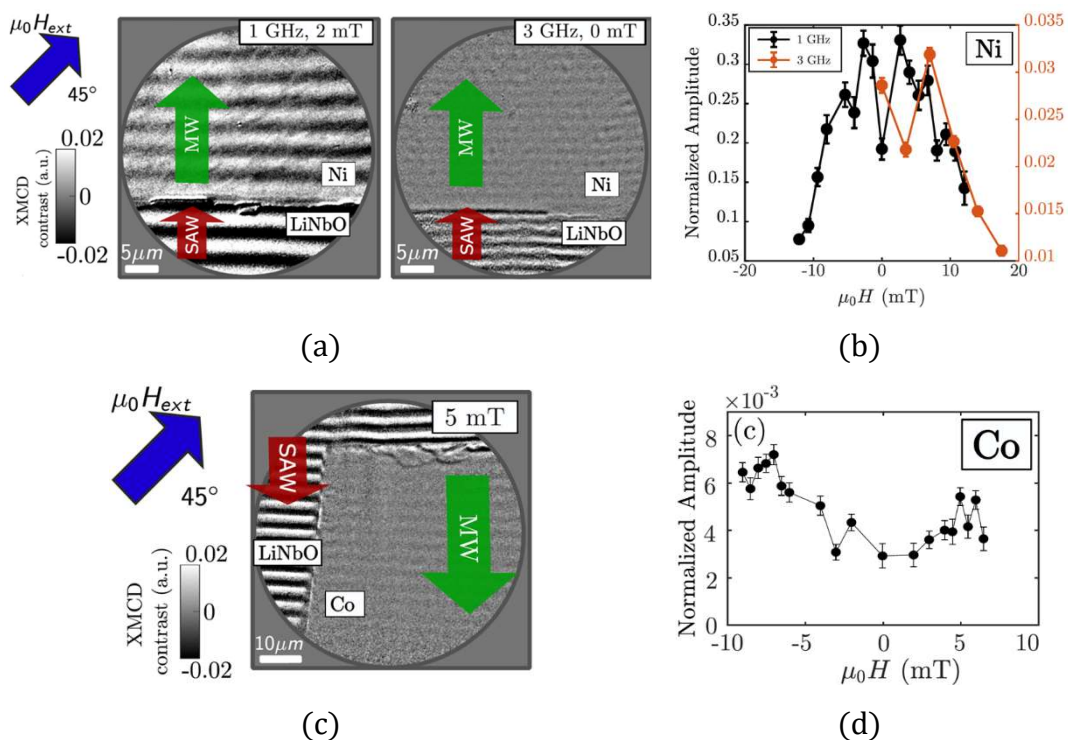


Figure 5.8. (a) 2-phase XMCD image of Ni showing the MAW driven at 1 GHz and 3 GHz. Both color scales are equal to visually see the difference in contrast and are expressed in XMCD contrast, which is the difference in absorption between light circularly polarized to the right or to the left. (b) Dependence of the MAW amplitude on the external magnetic field. The left axis represents the excitation at 1 GHz, while the right axis represents the excitation at 3 GHz. (c) 2-phase XMCD image showing the piezoelectric, LiNbO₃, with visible SAWs and the ferromagnetic sample, Co, with visible MAWs at an applied magnetic field of 5 mT. The color scale represents the XMCD contrast, which is the difference in absorption between light circularly polarized to the right or to the left. (d) MAW amplitude as a function of the applied magnetic field excited by a 1 GHz SAW.

The MAWs amplitude in the three experiments show considerable differences, although the strain values are similar. To understand this behavior, micromagnetic simulations including the magnetoelastic (ME) contribution were performed. The strength of the ME effect is expressed by the coupling constant B_1 . The data for Ni at 1 GHz is reproduced with a value for $B_1 = 11$ MJ/m³ which is compatible with the expected bulk (inverse) magnetostriction constant (Fig 5.9a). The simulation results for Ni show little sensitivity to the applied field angle at least in the range of 30–45 degree. However, in order to match data in Ni at 3 GHz, obtained in the same sample, it is needed to use a strongly reduced value for $B_1 = 0.3$ MJ/m³. We ascribe this decay to a reduced the efficiency of transmission of the SAW mechanical strain to the Ni thin film at high frequencies, thus hinting at the speed limit for practical applications of the ME effect. In contrast, in Co, we observe in the simulations a strong dependence of the expected MAW amplitude on the angle of the applied field and its strength, as seen in Fig. 5.9b. There is a sharp drop of the MAW resonance at low fields increasing angles. Therefore, experimental data for Co can be reproduced again by bulk like B_1 at 1 GHz.

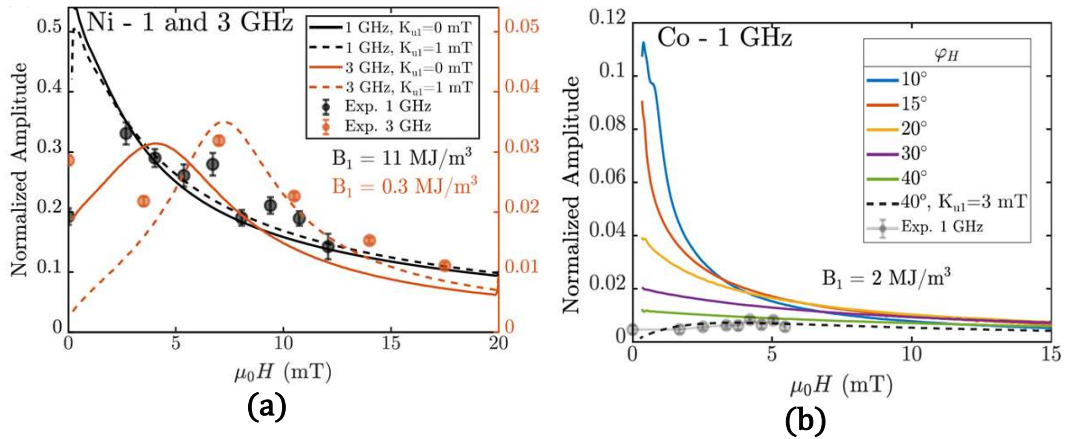


Figure 5.9. (a) Results of simulations. (a) Amplitude of MAW in Ni for excitation frequencies of 1 and 3 GHz with $\varphi_H = 45^\circ$ (solid black and orange curves, respectively). The dashed lines provide the same information including a small anisotropy, $K_{ij}^x = 1$ mT. The magnetoelastic constants used for each frequency are written in the same color as the simulation curves. The faint black and orange dots are the experimental results. (b) Amplitude of the MAW in Co for an excitation frequency of 1 GHz at several φ_H , from 10° to 40° . The dashed black line represents the simulation at 40° with a small anisotropy, $K_{ij}^x = 3$ mT, while the faint black dots correspond to the experimental results.

CHAPTER 6

ARTICLE – 6.1

Néel vector waves in antiferromagnetic CuMnAs excited by Surface Acoustic Waves

M. Waqas Khaliq^{1,2,*}, Oliver Amin³, Alberto Hernández-Mínguez⁴, Marc Rovirola^{1,5},
Blai Casals^{5,6}, Khalid Omari⁷, Sandra Ruiz-Gómez⁸, Simone Finizio⁹, Richard P.
Campion³, Kevin W. Edmonds³, Vít Novák¹⁰, Anna Mandziak¹¹, Lucía Aballe²,
Miguel Angel Niño², Joan Manel Hernández^{1,5}, Peter Wadley³, Ferran Macià^{1,5,†}, and
Michael Foerster^{2,‡}

¹ Dept. of Condensed Matter Physics, University of Barcelona, 08028-Barcelona, Spain

² ALBA Synchrotron Light Facility, 08290-Cerdanyola del Valles, Barcelona, Spain

³ School of Physics and Astronomy, University of Nottingham, NG7 2RD, UK

⁴ Paul Drude Institute for Solid State Electronics, 10117-Berlin, Germany

⁵ Institute of Nanoscience and Nanotechnology, University of Barcelona, 08028-Barcelona, Spain

⁶ Dept. of Applied Physics, University of Barcelona, 08028-Barcelona, Spain

⁷ Dept. of Electronic Engineering, Royal Holloway, University of London, TW20 0EX-Egham, UK

⁸ Max Planck Institute for Chemical Physics of Solids, 01187-Dresden, Germany

⁹ Swiss Light Source, Paul Scherrer Institute, 5232-Villigen, Switzerland

¹⁰ Institute of Physics AS CR, 16253-Prague, Czech Republic

¹¹ SOLARIS National Synchrotron Radiation Centre, 30-392-Kraków, Poland

<https://doi.org/10.48550/arXiv.2309.08893v1>

(Accepted in Physical Review Materials)

Néel vector waves in antiferromagnetic CuMnAs excited by Surface Acoustic Waves

M. Waqas Khaliq,^{1,2,*} Oliver Amin,³ Alberto Hernández-Mínguez,⁴ Marc Rovirola,^{1,5} Blai Casals,^{5,6} Khalid Omari,⁷ Sandra Ruiz-Gómez,⁸ Simone Finizio,⁹ Richard P. Campion,³ Kevin W. Edmonds,³ Vít Novák,¹⁰ Anna Mandziak,¹¹ Lucia Aballe,² Miguel Angel Niño,² Joan Manel Hernández,^{1,5} Peter Wadley,³ Ferran Macià,^{1,5,†} and Michael Foerster^{2,‡}

¹*Dept. of Condensed Matter Physics, University of Barcelona, 08028-Barcelona, Spain*

²*ALBA Synchrotron Light Facility, 08290-Cerdanyola del Valles, Barcelona, Spain*

³*School of Physics and Astronomy, University of Nottingham, NG7 2RD, UK*

⁴*Paul Drude Institute for Solid State Electronics, 10117-Berlin, Germany*

⁵*Institute of Nanoscience and Nanotechnology (IN2UB), University of Barcelona, 08028-Barcelona, Spain*

⁶*Dept. of Applied Physics, University of Barcelona, 08028-Barcelona, Spain*

⁷*Dept. of Electronic Engineering, Royal Holloway, University of London, TW20 0EX-Egham, UK*

⁸*Max Planck Institute for Chemical Physics of Solids, 01187-Dresden, Germany*

⁹*Swiss Light Source, Paul Scherrer Institute, 5232-Villigen, Switzerland*

¹⁰*Institute of Physics AS CR, 16253-Prague, Czech Republic*

¹¹*SOLARIS National Synchrotron Radiation Centre, 30-392-Kraków, Poland*

Magnetoelastic effects in antiferromagnetic CuMnAs are investigated by applying dynamic strain in the 0.01% range through surface acoustic waves in the GaAs substrate. The magnetic state of the CuMnAs/GaAs is characterized by a multitude of submicron-sized domains which we image by x-ray magnetic linear dichroism combined with photoemission electron microscopy. Within the explored strain range, CuMnAs shows magnetoelastic effects in the form of Néel vector waves with micrometer wavelength, which corresponds to an averaged overall spin-axis rotation up to 2.4° driven by the time-dependent strain from the surface acoustic wave. Measurements at different temperatures indicate a reduction of the wave amplitude when lowering the temperature. However, no domain wall motion has been detected on the nanosecond timescale.

Antiferromagnets (AFM) have become a focus of recent research in spintronics, mostly thanks to their potential advantages for future devices. Their low stray fields and robustness versus external magnetic fields are favorable for the further down-scaling of memory elements and their high-frequency internal resonances promise higher intrinsic speed limits for operation. However, together with these advantages also challenges arise, for example, related with the readout and mostly the writing process. Magnetic field control, although not completely impossible [1], is impractical due to the field magnitudes required ($\gtrsim 2$ T) in order to overcome exchange energy and modify the magnetization of the two sublattices existing in the AFM. Domain modification by electrical currents has been demonstrated through Spin transfer/orbit torque [2] as well as through thermoelastic effects [3]. Specifically for CuMnAs, the manipulation of antiferromagnetic domains in thin films has been studied by means of injecting current pulses [2, 4, 5] and defects [6]. Other approaches use the transitions to a ferromagnetic (FM) phase, like in FeRh [7], or the coupling with a FM [8], which compromise many of the potential advantages (stray fields, speed) of AFM materials for usage in a real device. On the other hand the appearance of closure domain-like features in patterned AFM samples has been attributed to

magnetoelastic effects caused by shape dependent strain [9, 10], which suggests that much smaller energies than the exchange energy may be enough to rotate the Néel vector.

Surface acoustic waves (SAW), are propagating elastic deformations in the upper micrometric layer of a crystal. SAW can be conveniently excited in piezoelectric materials by radiofrequency electrical signals applied to an antenna-like structure named interdigitated transducer (IDT). Typical strain amplitudes achieved under UHV conditions can reach the range of 2×10^{-4} for LiNbO₃ in the hundreds of MHz to GHz frequency regime [11]. There is a sizable interaction of SAW with FM systems in heterostructures, which is driven by the transfer of the space and time dependent strain state of the underlayer/substrate into the FM overlayer. The interaction is mediated by the magnetoelastic effect and has been investigated by a growing number of groups [12–24] (see review articles [25–27] and references therein). GaAs is a piezoelectric substrate suitable for SAW generation and propagation and allows for epitaxial growth of CuMnAs. This material has substantial applications in optoelectronic devices due to its outstanding photovoltaic properties [28] and robust piezoelectricity [29].

In this paper we generate Néel vector waves in collinear antiferromagnet CuMnAs induced by the time dependent strain from the supporting GaAs substrate. We use stroboscopic X-ray photoemission electron microscopy (XMLD-PEEM) combined with magnetic linear dichroism to image both dynamic strain and

* mkhaliq@cells.es

† ferran.macia@ub.edu

‡ mfoerster@cells.es

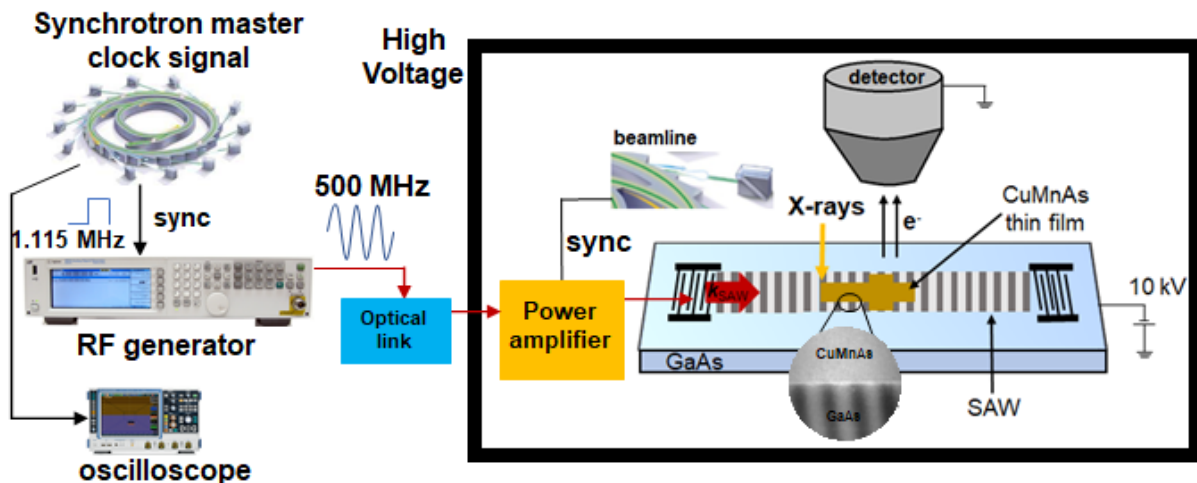


FIG. 1. Schematic illustration of the stroboscopic experiment. The CuMnAs thin film is patterned in the acoustic path of the SAW and analyzed in the PEEM microscope. SAWs are generated in the GaAs substrate by applying an electrical signal to the IDTs, which is synchronized with the synchrotron frequency (repetition rate time of the X-ray pulses). The microscope detector (XPEEM Objective) is operated at 10 kV with respect to the sample to accelerate low energy electrons kicked out by the X-rays. The PEEM image is formed by photoelectrons emitted from the sample under the X-ray illumination. The inset shows the XPEEM image of the edge of the CuMnAs in presence of SAW, which are visible in the GaAs substrate as they modify the surface potential (however, no signal appears in the CuMnAs as it shunts the electrical signal and keeps the surface at a constant voltage).

Néel vector oscillations. We quantify both strain and amplitude of the Néel vector rotation up to 2.4° . The overall amplitude of the observed Néel vector oscillations decreased with lowering temperature.

Experiments were carried out at the CIRCE beamline of the ALBA Synchrotron light source [30]. The CuMnAs epitaxial thin films with 45 nm thickness were grown on lattice-matched GaAs substrate by molecular beam epitaxy as described previously [31]. To generate SAWs with a frequency tuned to the synchrotron repetition rate (500 MHz), IDT with a finger periodicity of $5.73 \mu\text{m}$ (which determines the SAW wavelength) were patterned and deposited on the GaAs by electron beam lithography and metal evaporation. The sample was mounted on a printed circuit board (PCB) inside the sample holder and the IDT were contacted with wire bonds to apply electrical signals. The schematic illustration of the experiment is presented in Fig. 1. The radiofrequency signal applied to the IDT generates a SAW beam [32] traveling along the [110] crystalline direction of the GaAs substrate and confined to a depth in the order of the SAW wavelength [27]. The SAW causes a periodic in-plane, parallel to the SAW propagation direction, and out-of-plane change in the substrate lattice constant which is transferred as strain to the CuMnAs film.

In order to assess the structure of the CuMnAs thin film, X-ray diffraction (XRD) measurements were carried out on the sample using a laboratory diffractometer before the synchrotron experiment. The XRD pattern in Fig. 2a shows the peaks of both the CuMnAs

film (black) and the GaAs substrate (red) with respect to 2θ . The tetragonal crystal system ($P4/nmm$) and the planes (001), (002), (003), and (004) of the antiferromagnetic thin film were identified with the Powder Diffraction File 01-082-3986 from the Joint Committee on Powder Diffraction Standards-International Centre for Diffraction Data [33–35].

X-ray absorption spectroscopy (XAS) measurements of the CuMnAs were performed detecting low energy secondary electrons in the PEEM while scanning the photon energy. The beamline is equipped with an undulator that enables the control of the incoming X-ray polarization, for example between linear horizontal (electric field vector in the sample plane) and vertical (electric field vector under 16 degree to the sample normal) polarization directions. X-ray absorption spectra at the Mn $L_{3,2}$ edges, with both polarizations, and their difference (linear dichroism, XMLD), are depicted in Fig. 2b at $T \simeq 235$ K. The features of the XMLD spectrum (blue line), marked by black boxes, are similar to previously published data [36].

The imaging of antiferromagnetic domains in the CuMnAs thin film is performed by PEEM employing XMLD contrast. Such a contrast is obtained by subtracting different images taken with linear horizontal polarization at energies before and at the L_3 absorption peak (See details of the methodology in Supp. Mater. I). Fig. 2c shows the domains arrangement in the film at 223 K nominal temperature without any SAW applied. Equivalent images taken with linear vertical polarization (electric field vector 16° to the sample normal) did not show visible contrast, confirming a

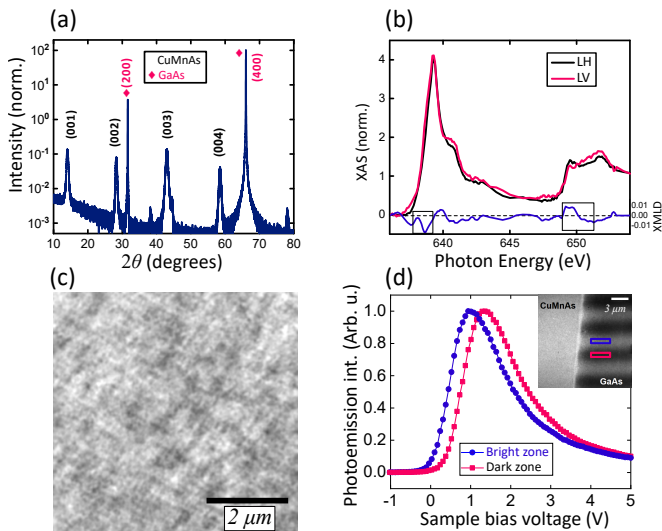


FIG. 2. (a) XRD measurements of 45 nm thin film of CuMnAs on GaAs showing the film (black) and substrate (red) peaks (b) XAS and XMLD spectra of CuMnAs/GaAs at the Mn $L_{3,2}$ edges, obtained with horizontal (black) and vertical (red) linear polarization. (c) An XMLD image of CuMnAs thin film at $T \simeq 223$ K without applying SAW signal. The magnetic contrast is clearly visible in CuMnAs. (d) Quantification of the SAW: Average intensity (number of emitted electrons) from the red and blue rectangles in the inset as a function of sample bias voltage. The inset shows the XPEEM image of the SAW in GaAs (at the edge with CuMnAs) at 0.7 V bias.

dominant in-plane Néel vector. In order to quantify the dynamic magnetoelastic effects in the CuMnAs film, it is necessary to determine first the amplitude of the SAW-induced strain. We cannot determine this quantity directly in the studied CuMnAs film because it is conductive and shunts the electrical component of the SAW, but instead we can do it in the GaAs substrate. The inset of Fig. 2d depicts an XPEEM image of the sample surface in presence of SAW, measured with 500 MHz pulsed synchrotron X-rays. An intensity contrast with a periodicity matching the SAW wavelength, i.e., $5.73 \mu\text{m}$, is evident in the sample region not covered by the CuMnAs film. This contrast originates from the oscillating piezoelectric potential accompanying the strain wave at the surface of the GaAs substrate. The photoelectron spectra displayed in Fig. 2d show the average intensity (number of detected electrons) at the areas marked by the red and blue rectangles in the inset image, recorded as a function of the bias voltage applied to the substrate for a fixed energy analyzer configuration. The voltage shift between these curves, obtained by selecting the positions of maximum slope in both spectra, amounts to 0.35 V and corresponds to the peak-to-peak amplitude of the oscillating piezoelectric potential. This value is used to calculate the amplitude of the strain field by numerically solving the coupled differential equations of the mechanical and electrical

displacement, obtaining values in the range of 0.01% at the sample surface. Details on stroboscopic XPEEM measurements with synchronized SAW can be found in [11].

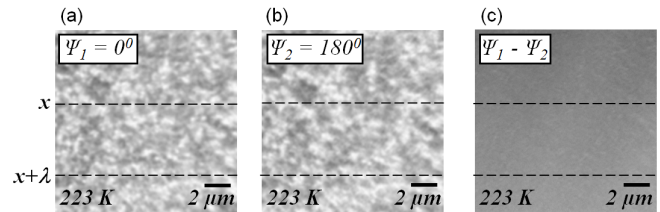


FIG. 3. XMLD images of CuMnAs with opposite electronic phases $\psi = 0^\circ$ in (a) and $\psi = 180^\circ$ in (b) of the SAW excitation at $T \simeq 223$ K. The direction of SAW propagation is perpendicular to the dashed lines which are separated by one wavelength of $5.73 \mu\text{m}$. (c) Image obtained by subtracting the images at opposite phases, at the same contrast scale. No evident variations in the domain boundaries can be observed.

Fig. 3 shows XMLD images at the CuMnAs taken while the SAW is applied. The bright and dark areas in Fig. 3 correspond to domains with spin axis parallel and perpendicular to the X-ray polarization, with a typical domain size below one micrometer. The presence of domains with continuously differing gray scale contrast indicates the absence of significant in-plane anisotropy for the spin axis in the sample. Between Fig. 3a and 3b, the phase of the radiofrequency signal exciting the SAW was shifted by 180° . Thus, the phase of the SAW in any given position is inverted for the stroboscopic measurement, i.e., when the X-rays hit the sample. A close inspection of the individual images shown in Figs. 3a and 3b as well as the difference image (Fig. 3c), same gray scale, does not show any observable change of the domain boundaries. The domain wall motion in the CuMnAs in the present experiment is thus either negligible or below the detection limit. The difference images are used to eliminate the static domain contrast and enhance the dynamic changes induced by the SAW.

Several difference images equivalent to the one shown in Fig. 3c, were recorded at different SAW phases (typically 15°) with a larger integration time to reduce noise. Fig. 4a is a difference image with a contrast enhanced about 100 times compared to Fig. 3c and shows the oscillatory component of the Néel vector. Line profiles along the direction of the SAW were extracted from each difference image taken at different SAW phases. The results are summarized in Fig. 4b–d and correspond to data sets at low temperature, $T = 223$ K and $T = 233$ K, and room temperature, $T = 296$ K. The plotted curves correspond to the averaged profiles over all SAW phases (see Supp. Mater. II for details on the data analysis) and green lines are best fits with sinusoidal functions, which are used to obtain the amplitude of the Néel vector signal at each temperature. The insets of Fig. 4b–d show the phase value from each difference image profile showing

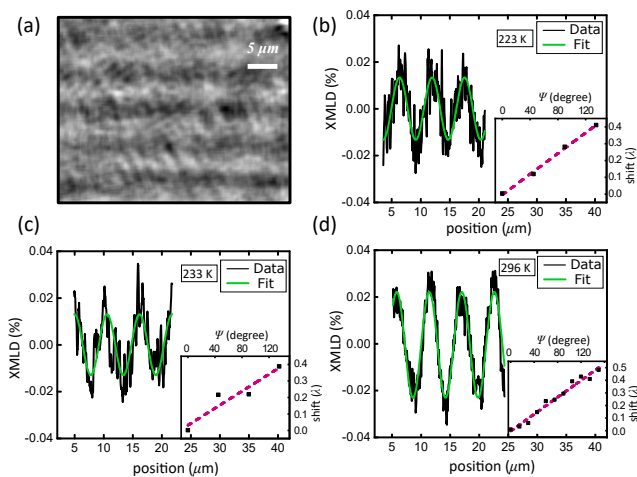


FIG. 4. Néel vector wave (spin axis rotation wave) in CuMnAs observed by XMLD-PEEM. a) Image obtained by subtracting the XMLD images at opposite phases of SAW. b-d) XMLD signal (in %) extracted from CuMnAs along the direction of the propagation of the SAW after averaging at $T \simeq 223$ K in b), $T \simeq 233$ K, in c) and $T \simeq 296$ K in d). The black line in each plot shows the data and the green line is the sinusoidal function curve fitted to the data points. Insets show the fitted phase shift as a function of the shift ψ in the SAW excitation.

the measured shift of the wave in units of the wavelength, λ . These values are in excellent agreement with the electronic phase ψ applied to the IDT, which demonstrates that the Néel vector oscillations are driven by SAW.

Now we turn to the quantitative analysis of the Néel vector rotation amplitudes for the three data sets at different temperatures, i.e., $T = 223$ K, $T = 233$ K, and $T = 296$ K. The results are summarized in Table I. Due to experimental constraints, the low-temperature data was taken with an angle of 65° between SAW and probing X-rays, while room temperature data was taken with a 90° angle. The conversion of XMLD amplitude to rotation in degrees as well as the correction factor for the reduced sensitivity under 65° is calculated in Supp. Mater. III. As mentioned above, the applied strain from the SAW has been calculated from the voltage shift of the secondary electron spectra detected in the PEEM (Fig. 2d). The typical strain amplitudes achieved in our experiments on GaAs are $(0.75 - 1) \times 10^{-4}$. The XMLD wave amplitude was determined from fits to the averaged line profiles in Fig. 4b-d. In order to convert those numbers into the corresponding rotation of the spin axis, we take first into account the temperature dependence of the XMLD contrast in CuMnAs. The XMLD wave amplitude is thus normalized to the maximum XMLD contrast for each temperature in the static domain image (see, Fig. 2c for example), taken as average in three different locations each. We then consider the film to be populated by an equal portion of domains in all direction, i.e., without net in-plane anisotropy and calculate for each domain i) the rotation angle as fraction of a

maximum angle ϕ_0 as explained in Supp. Mater. III and ii) the sensitivity of the XMLD signal to this rotation as function of the domain spin axis.

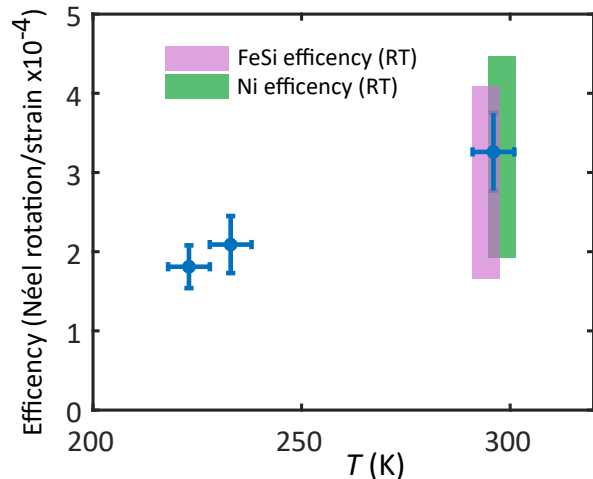


FIG. 5. Efficiency of the magnetoacoustic wave excitation in CuMnAs as a function of temperature in comparison with all data at 500 MHz SAW. The area for Ferromagnetic samples corresponds to Ni and FeSi at room temperature (RT) and covers the range between zero external field and resonance.

The numbers reported in Table I show that the Néel vector wave driven by SAW in CuMnAs can reach a sizable 2.44° at room temperature. We plotted in Fig. 5 the efficiency of the SAW induced Néel vector wave defined as the overall variation divided by the SAW strain for the three temperatures. A similar quantity is added into the graph for magnetoacoustic waves in ferromagnetic samples measured through XMCD [22, 37]. Values for ferromagnetic Ni [22] and Heusler alloy Fe_3Si [37] are shown as broad bands, because they depend on the external applied magnetic field, showing a resonance like peak (Ni showed an efficiency of 2 to 4.5 and FeSi from 1.6 to 4.1). These results indicate a sizable dynamic magneto-elastic effect in CuMnAs induced by SAW and a comparable efficiency like in FM materials. The space and time oscillating strain results in a modulation of the film's anisotropy, which in a FM can be understood as a modulation of the effective magnetic field generating a modulation of the magnetic moment. However, in AFM such a small effective magnetic field does not serve to modulate magnetic moment or to shift magnetic domains but instead it is capable to rotate the Néel vector with a similar efficiency. We notice here that detection of spin axis rotation in CuMnAs is more challenging compared to magnetoacoustic waves in ferromagnets mainly because the XMLD contrast is weaker and because the sample is in a multi-domain state.

A reduction of the Néel vector wave excitation efficiency when lowering temperature, i.e., from $3.3^\circ/10^{-4}$ strain at room temperature (296 K) to $1.8^\circ/10^{-4}$ at 223 K has been observed. While this apparent reduction

Temperature (K)	Max. XMLD Domain Contrast ($\times 10^{-3}$)	SAW orientation w.r.t. X-rays (degrees)	Strain Amplitude ($\times 10^{-4}$)	XMLD wave amplitude ($\times 10^{-4}$)	Néel vector rotation (degrees)	Efficiency (degrees/strain $\times 10^{-4}$)
223	7.6 ± 1.0	65	0.86 ± 0.05	1.33	1.56 ± 0.21	1.81 ± 0.27
233	6.4 ± 1.0	65	0.86 ± 0.05	1.29	1.80 ± 0.29	2.09 ± 0.36
296	5.3 ± 0.7	90	0.75 ± 0.05	2.26	2.44 ± 0.33	3.26 ± 0.49

TABLE I. Quantitative results of the Néel vector wave in CuMnAs at different temperatures.

needs further experiments to be confirmed [38, 39], it may indicate an increase of the energy barrier for the spin axis rotation as temperature lowers (a type of “freezing”), or an increase on the Néel vector anisotropy value.

In summary, we have investigated high frequency (500 MHz) magnetoelastic effects in antiferromagnetic CuMnAs excited by SAW in the GaAs substrate using XMLD-PEEM. An averaged magneto-acoustic wave signal can be detected in XMLD, corresponding to a rotation of the spin axis in the individual domains by up to $\pm 2.4^\circ$. The efficiency of the Néel vector excitation in CuMnAs is a proof that magnetoelastic effects are a viable way to manipulate antiferromagnetic systems, even on the sub-nanosecond time scale. Moreover, in static condition, the CuMnAs thin film is characterized by a multidomain configuration of submicron size. No SAW-induced motion of domain walls has been detected, which could be related to intrinsic pinning due the film microstructure. For the future, a combination of GaP substrates with ZnO based IDT can enable to study SAW driven effects

in high quality single domain patterns of CuMnAs.

ACKNOWLEDGMENTS

The authors are thankful to Spanish Ministry of Science, Innovation, Universities, and DOC-FAM who have received funding from the European Union’s Horizon 2020 research and innovation program under the Marie Skłodowska-Curie grant agreement No. 754397. MWK MF, MAN, and LA acknowledge the funding from MICINN through grant numbers RTI2018-095303-B-C53 and PID2021-122980OB-C54. FM, MR, BC, and JMH are grateful to funding from MCIN/AEI/10.13039/501100011033 through grant number: PID2020-113024GB-I00. OA, KO, KWE, RPC, and PW acknowledge funding from EU FET Open RIA Grant no 766566. VN is grateful to MEYS Grant No. LM2018110. This work has also been supported by the ALBA in House Research Program.

-
- [1] A. A. Sapozhnik, M. Filianina, S. Y. Bodnar, A. Lami-rand, M.-A. Mawass, Y. Skourski, H.-J. Elmers, H. Zabel, M. Kläui, and M. Jourdan, Direct imaging of antiferromagnetic domains in Mn₂Au manipulated by high magnetic fields, *Physical Review B* **97**, 134429 (2018).
- [2] P. Wadley, B. Howells, J. Železný, C. Andrews, V. Hills, R. P. Campion, V. Novák, K. Olejnik, F. Maccherozzi, S. S. Dhesi, *et al.*, Electrical switching of an antiferromagnet, *Science* **351**, 587 (2016).
- [3] H. Meer, F. Schreiber, C. Schmitt, R. Ramos, E. Saitoh, O. Gomonay, J. Sinova, L. Baldrati, and M. Kläui, Direct imaging of current-induced antiferromagnetic switching revealing a pure thermomagnetoelastic switching mechanism in NiO, *Nano Letters* **21**, 114 (2021).
- [4] P. Wadley, S. Reimers, M. J. Grzybowski, C. Andrews, M. Wang, J. S. Chauhan, B. L. Gallagher, R. P. Campion, K. W. Edmonds, S. S. Dhesi, *et al.*, Current polarity-dependent manipulation of antiferromagnetic domains, *Nat. Nanotechnol.* **13**, 362 (2018).
- [5] T. Janda, J. Godinho, T. Ostatnicky, E. Pfitzner, G. Ulrich, A. Hoehl, S. Reimers, Z. Soban, T. Metzger, H. Reichlova, *et al.*, Magneto-seebeck microscopy of domain switching in collinear antiferromagnet CuMnAs, *Phys. Rev. Mat.* **4**, 094413 (2020).
- [6] S. Reimers, D. Krieger, O. Gomonay, D. Carbone, F. Krizek, V. Novák, R. P. Campion, F. Maccherozzi, A. Björling, O. J. Amin, *et al.*, Defect-driven antiferromagnetic domain walls in CuMnAs films, *Nat. Commun.* **13**, 724 (2022).
- [7] I. Fina and J. Fontcuberta, Strain and voltage control of magnetic and electric properties of FeRh films, *J. Phys. D: Appl. Phys.* **53**, 023002 (2020).
- [8] B.-Y. Wang, C.-H. Hsiao, B.-X. Liao, C.-Y. Hsu, T.-H. Li, Y.-L. Hsu, Y.-M. Lai, M.-S. Tsai, T.-H. Chuang, and D.-H. Wei, Perpendicular magnetic anisotropy induced by nimm-based antiferromagnetic films with in-plane spin orientations: Roles of interfacial and volume antiferromagnetic moments, *Physical Review B* **104**, 024424 (2021).
- [9] H. Meer, O. Gomonay, C. Schmitt, R. Ramos, L. Schnitzspan, F. Kronast, M.-A. Mawass, S. Valencia, E. Saitoh, J. Sinova, *et al.*, Strain-induced shape anisotropy in antiferromagnetic structures, *Physical Review B* **106**, 094430 (2022).
- [10] J. A. Arregi, F. Ringe, J. Hajduček, O. Gomonay, T. Molnár, J. Jaskowiec, and V. Uhlíř, Magnetic-field-controlled growth of magnetoelastic phase domains in ferh, *Journal of Physics: Materials* **6**, 034003 (2023).
- [11] M. Foerster, N. Statuto, B. Casals, A. Hernández-Mínguez, R. Cicheler, P. Manshausen, A. Mandziak, L. Aballe, J. Hernández Ferràs, and F. Macià, Quantification of propagating and standing surface acoustic waves by stroboscopic X-ray photoemission electron microscopy, *J. Synchrotron Rad.* **26**, 184 (2019).

- [12] J. Hernandez, P. Santos, F. Macià, A. García-Santiago, and J. Tejada, Acoustomagnetic pulse experiments in $\text{LiNbO}_3/\text{Mn}_{12}$ hybrids, *Appl. Phys. Lett.* **88**, 012503 (2006).
- [13] S. Davis, A. Baruth, and S. Adenwalla, Magnetization dynamics triggered by surface acoustic waves, *Appl. Phys. Lett.* **97**, 232507 (2010).
- [14] M. Weiler, L. Dreher, C. Heeg, H. Huebl, R. Gross, M. S. Brandt, and S. T. Goennenwein, Elastically driven ferromagnetic resonance in nickel thin films, *Physical Review Letters* **106**, 117601 (2011).
- [15] M. Weiler, H. Huebl, F. S. Goerg, F. D. Czeschka, R. Gross, and S. T. Goennenwein, Spin pumping with coherent elastic waves, *Physical Review Letters* **108**, 176601 (2012).
- [16] L. Thevenard, I. S. Camara, S. Majrab, M. Bernard, P. Rovillain, A. Lemaître, C. Gourdon, and J.-Y. Duquesne, Precessional magnetization switching by a surface acoustic wave, *Physical Review B* **93**, 134430 (2016).
- [17] D. Labanowski, A. Jung, and S. Salahuddin, Power absorption in acoustically driven ferromagnetic resonance, *Appl. Phys. Lett.* **108**, 022905 (2016).
- [18] M. Foerster, F. Macià, N. Statuto, S. Finizio, A. Hernández-Mínguez, S. Lendínez, P. V. Santos, J. Fontcuberta, J. M. Hernández, M. Kläui, et al., Direct imaging of delayed magneto-dynamic modes induced by surface acoustic waves, *Nat. Commun.* **8**, 407 (2017).
- [19] P. Kuszewski, I. S. Camara, N. Biarrotte, L. Becerra, J. von Bardeleben, W. S. Torres, A. Lemaître, C. Gourdon, J.-Y. Duquesne, and L. Thevenard, Resonant magneto-acoustic switching: influence of rayleigh wave frequency and wavevector, *J. Phys. Condens. Matter* **30**, 244003 (2018).
- [20] M. Foerster, L. Aballe, J. M. Hernández, and F. Macià, Subnanosecond magnetization dynamics driven by strain waves, *MRS Bull.* **43**, 854 (2018).
- [21] A. Adhikari and S. Adenwalla, Surface acoustic waves increase magnetic domain wall velocity, *AIP Advances* **11**, 015234 (2021).
- [22] B. Casals, N. Statuto, M. Foerster, A. Hernández-Mínguez, R. Cicheler, P. Manshausen, A. Mandziak, L. Aballe, J. M. Hernández, and F. Macià, Generation and imaging of magnetoacoustic waves over millimeter distances, *Physical Review Letters* **124**, 137202 (2020).
- [23] C. Müller, P. Durdaut, R. B. Holländer, A. Kittmann, V. Schell, D. Meyners, M. Höft, E. Quandt, and J. McCord, Imaging of love waves and their interaction with magnetic domain walls in magnetoelectric magnetic field sensors, *Advanced Electronic Materials* **8**, 2200033 (2022).
- [24] K. M. Seemann, O. Gomonay, Y. Mokrousov, A. Hörner, S. Valencia, P. Klamser, F. Kronast, A. Erb, A. Hindmarch, A. Wixforth, et al., Magnetoelastic resonance as a probe for exchange springs at antiferromagnet-ferromagnet interfaces, *Physical Review B* **105**, 144432 (2022).
- [25] P. Delsing, A. N. Cleland, M. J. A. Schuetz, J. Knörzer, G. Giedke, J. I. Cirac, K. Srinivasan, M. Wu, et al., The 2019 surface acoustic waves roadmap, *Journal of Physics D: Applied Physics* **52**, 353001 (2019).
- [26] W.-G. Yang and H. Schmidt, Acoustic control of magnetism toward energy-efficient applications, *Applied Physics Reviews* **8**, 021304 (2021).
- [27] J. Puebla, Y. Hwang, S. Maekawa, and Y. Otani, Perspectives on spintronics with surface acoustic waves, *Appl. Phys. Lett.* **120**, 220502 (2022).
- [28] B. Dong and M. E. Zaghoul, Generation and enhancement of surface acoustic waves on highly doped p-type GaAs substrate, *Nanoscale Advances* **1**, 3537 (2019).
- [29] A. Rampal and R. N. Kleiman, Optical actuation of a micromechanical photodiode via the photovoltaic-piezoelectric effect, *Microsystems & Nanoengineering* **7**, 29 (2021).
- [30] L. Aballe, M. Foerster, E. Pellegrin, J. Nicolas, and S. Ferrer, The ALBA spectroscopic LEEM-PEEM experimental station: layout and performance, *J. Sync. Rad.* **22**, 745 (2015).
- [31] P. Wadley, V. Novák, R. P. Campion, C. Rinaldi, X. Marti, H. Reichlová, J. Železný, J. Gázquez, M. A. Roldan, M. Varela, D. D. Khalyavin, S. Langridge, D. Kriegner, F. Máca, J. D. I. Masek, R. Bertacco, V. Holý, A. W. Rushforth, K. W. Edmonds, B. L. Gallagher, C. T. Foxon, J. Wunderlich, and T. Jungwirth, Tetragonal phase of epitaxial room-temperature antiferromagnet CuMnAs , *Nature Communications* **4**, 2322 (2013).
- [32] B. von Boehn, M. Foerster, M. von Boehn, J. Prat, F. Macià, B. Casals, M. Khaliq, A. Hernández-Mínguez, L. Aballe, and R. Imbihl, On the promotion of catalytic reactions by surface acoustic waves, *Angew. Chem. Int. Ed.* **59**, 20224 (2020).
- [33] A. N. Nateprov, V. C. Kravtsov, V. Fritsch, and H. von Löhneysen, Structure and properties of the tetragonal phase of MnCuAs , *Surf. Engin. Appl. Electrochem.* **47**, 540 (2011).
- [34] V. Hills, P. Wadley, R. P. Campion, R. Beardsley, K. W. Edmonds, B. L. Gallagher, V. Novak, B. Ouladdiaf, and T. Jungwirth, Paramagnetic to antiferromagnetic transition in epitaxial tetragonal CuMnAs , *Journal of Applied Physics* **117**, 172608 (2015).
- [35] W. Wong-Ng, H. McMurdie, C. Hubbard, and A. Mighell, enJcpds-icdd research associateship (cooperative program with nbs/nist) (2001).
- [36] P. Wadley, V. Hills, M. Shahedkhah, K. Edmonds, R. Campion, V. Novák, B. Ouladdiaf, D. Khalyavin, S. Langridge, V. Saidl, P. Nemeč, A. Rushforth, B. Gallagher, S. Dhesi, F. Maccherozzi, J. Železný, and T. Jungwirth, Antiferromagnetic structure in tetragonal CuMnAs thin films, *Scientific Reports* **5**, 17079 (2015).
- [37] M. Rovirola, M. W. Khaliq, B. Casals, M. Foerster, M. A. Niño, J. Herfort, J. M. Hernández, F. Macià, and A. Hernández-Mínguez, Resonant and off-resonant magnetoacoustic waves in epitaxial $\text{Fe}_3\text{Si}/\text{GaAs}$ hybrid structures (2022), arXiv:2212.07994 [cond-mat.mtrl-sci].
- [38] V. Grigorev, M. Filianina, Y. Lytvynenko, S. Sobolev, A. R. Pokharel, A. Sapozhnik, A. Kleibert, S. Y. Bodnar, P. Grigorev, Y. Skourski, M. Kläui, H.-J. Elmers, M. Jourdan, and J. Demsar, Optically-triggered strain-driven Néel vector manipulation in a metallic antiferromagnet (2022), arXiv:2205.05411 [cond-mat.mtrl-sci].
- [39] T. P. Lyons, J. Puebla, K. Yamamoto, R. S. Deacon, Y. Hwang, K. Ishibashi, S. Maekawa, and Y. Otani, Acoustically driven magnon-phonon coupling in a layered antiferromagnet, *Phys. Rev. Lett.* **131**, 196701 (2023).

Supplementary Material

I. IMAGING OF DOMAINS

XMLD images are obtained by calculating the asymmetry, $[I(E_1)-I(E_2)]/[I(E_1)+I(E_2)]$, where $I(E_1)$ represents the intensity measured with x-ray energy at the Mn L_3 absorption edge peak and $I(E_2)$ the one at 0.9 eV before the peak [1]. The images at both energies, which correspond to the opposite peaks of the XMLD spectrum, are acquired with linear horizontal x-ray polarization (electric field vector in the sample plane). Thus, images referred to as XMLD image are employing opposite XMLD contrast at different photon energies, but are technically obtained with a single polarization in order to enhance the contrast.

II. DATA ANALYSIS AND IMAGING OF NÉEL VECTOR WAVES

We present now the detection of magnetoelastic effects in CuMnAs/GaAs as evidenced by a Spin rotation axis wave signal similar to waves of the overall magnetic moment observed in ferromagnets [2, 3], i.e., a phase dependent oscillation of the XMLD contrast averaged over the multidomain state.

For the measurement of the comparatively weak Néel vector (spin rotation axis) signal an elaborated data treatment process was needed. The scheme of our method is illustrated in Fig. S1. A single XMLD image (C) at specific electronic phase, ψ_1 (of the SAW excitation) was acquired by subtracting the images (A and B) obtained at 2 different energies around the Mn L_3 peak, both at linear horizontal polarization which is known to enhance the XMLD contrast for an image. A second XMLD image (D) at opposite phase ($\psi_1 + 180^\circ$) of the SAW with respect to the first is recorded in the same way. In the difference image C - D, called ψ_1 , the static (domain) XMLD contrast is eliminated and only the dynamic change due to the SAW is added up, enhancing the MAW signal in the film.

For the line profile plots presented in Fig. 4 of the main manuscript, a line profile for each single difference image was extracted. For each profile, a background is created by averaging over one wavelength and subsequently subtracted to eliminate the background from the data. The phase for each line profile as parameter of a sinusoidal fit is shown in the insets of Fig. 4, confirming the expected shift with the SAW phase. The final line profiles,

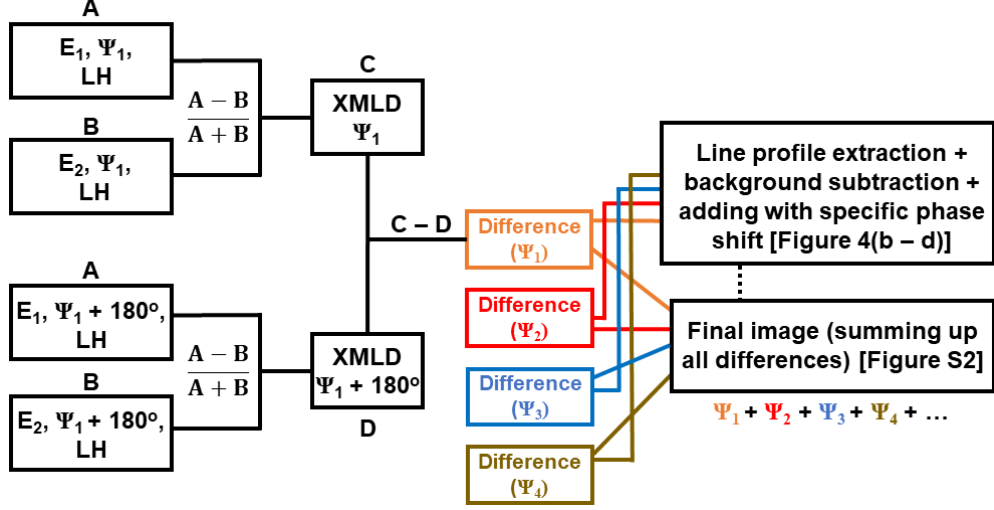


FIG. S1. Schematic diagram of the data treatment process. XMLD images for opposite electronic (SAW) phases (ψ and $\psi + 180$) are subtracted. For the data shown in Fig. 4b–d in the main manuscript, line profiles are extracted, and averaged with the corresponding phase shift after background subtraction. For the image shown in Fig. 5 in the main manuscript, all 11 difference images taken at room temperature are averaged with their corresponding phase shifts.

shown in the main panels are obtained by averaging all single profiles after shifting by the number of pixel corresponding to the nominal SAW phase ψ_i . The phase-distance (pixel) relation was determined by direct images of the SAW in GaAs.

Finally we can obtain an image of the Néel vector wave when directly averaging all the difference images after shifting them along the SAW propagation direction by the number of pixel corresponding to the nominal SAW phase ψ_i . Fig. S2 shows the resulting image for the data sets at room temperature, which shows the largest rotation and contains most individual data sets for improved statistics.

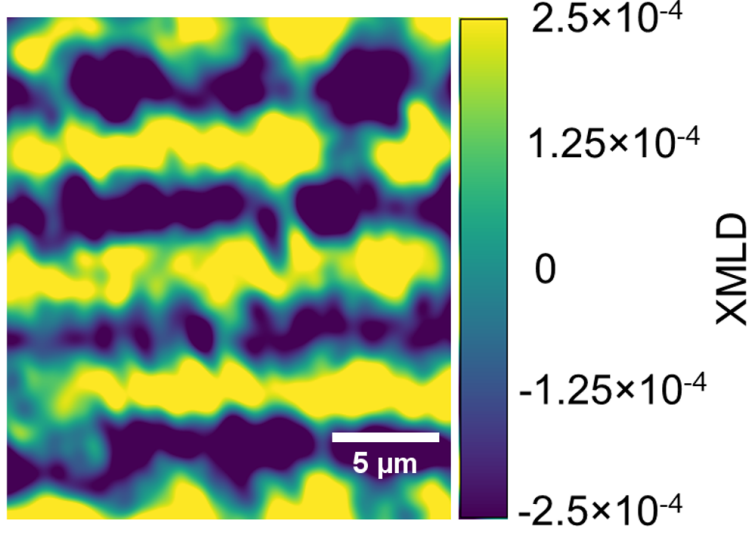


FIG. S2. Visualization of the Néel vector wave in CuMnAs: average of all XMLD phase difference images at room temperature after shifting them along the SAW propagation direction to accommodate for the electronic phase shift of the SAW. Yellow and purple colors denote a positive or negative dynamic XMLD as indicated by the color scale.

III. MODEL OF THE NÉEL VECTOR WAVE AND QUANTIFICATION OF THE ROTATION ANGLE

As illustrated in Fig. S3 for a random multidomain configuration the SAW is expected to cause a local oscillation ($\pm\phi$) of the Néel vector, depending on the initial domain state. Based on the derivative of the magnetoelastic energy $E = K \sin^2(\alpha)$, where α is the equilibrium angle of the AFM Néel vector with respect to the SAW propagation direction, and K an anisotropy constant determined by magnetostriction, we model the spin axis rotation by

$$\alpha' = \alpha + 2\phi_0 \sin \alpha \cos \alpha \cos(\omega t) \quad (1)$$

where (ωt) is the SAW phase in the given location of the domain. This means the rotation amplitude $2\phi_0 \sin \alpha \cos \alpha$ is proportional to the magnetoelastic contribution to the effective magnetic field ($H_{\text{eff}} = -\frac{dE}{d\alpha}$) in the LLG formalism. Here, we have supposed that only the in-plane strain of the SAW contributes to the magnetoelastic effects in the CuMnAs film. This function is shown in the lower part of Fig. S3 and takes extreme values $\pm\phi_0$ at 45° and 135° while being zero at 0° and 90° . The, maybe at first sight, surprising fact of zero rotation at the energy maxima (90°) can be understood from the absence of torque on the spin axis

and also follows from continuity requirements (smooth transition from positive to negative angle). The shape of this function is also in agreement with our previous experiments with the same phenomena on polycrystalline Ni, where the efficient magnetoacoustic wave excitation appears when the sample is in a single domain state under 45° with the SAW. For CuMnAs in a multidomain state, the spin axis rotation can be detected as a large-scale

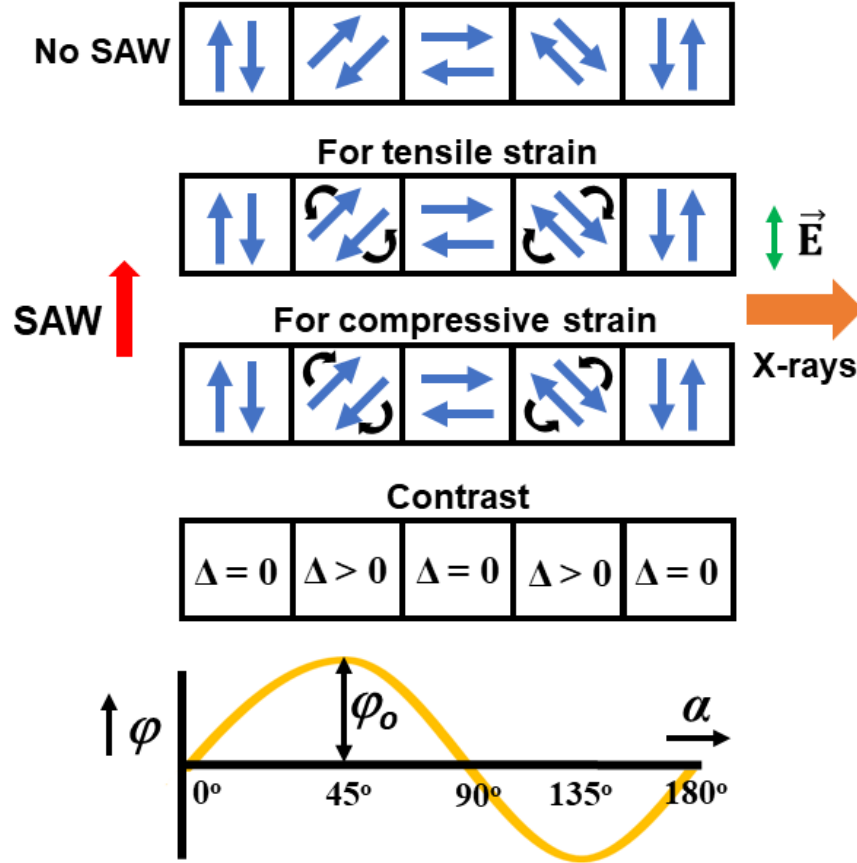


FIG. S3. Schematic illustration of the magneto-acoustic wave contrast formation in the multidomain state by XMLD imaging for five different initial domains corresponding to $\alpha = 0, 45, 90, 135,$ and 180 degrees. Different rows correspond to different strain states (zero, tensile or compressive) and show the Neel vector state depending on the SAW phase. Fourth row shows the difference in XMLD contrast between the two SAW phases (second and third row) which is zero in some cases but has the same sign in the others. Bottom: functional dependence of the spin axis rotation ϕ on the angle α between spin-axis and SAW.

averaged oscillation of the XMLD contrast when using a suitable angle between the incoming x-rays and the SAW. In short, in all the areas with the same phase of the SAW-induced

strain (tensile or compressive), all domains tend to rotate their spin axis towards the same direction determined by the magneto-elastic effect, even though the actual degree of rotation is different, as well as the sensitivity of the probing x-ray.

Thus, one needs to write the domain-averaged dynamic XMLD contrast as:

$$\Delta\text{XMLD}_{\text{avg}} = \int_0^\pi D(\alpha) \cdot \Delta\text{XMLD}(\alpha) d\alpha, \quad (2)$$

where $\Delta\text{XMLD}_{\text{avg}}$ is the average dynamic (wave) XMLD contrast, $\Delta\text{XMLD}(\alpha)$ is the wave contrast obtained in the presence of SAW for a domain with an angle α between the SAW and spin axis, and $D(\alpha)$ is the distribution of domains as a function of α , for an equal distribution it becomes $D(\alpha) = \frac{1}{\pi}$. Note that for the optimum conditions, i.e., 0° and 90° between SAW and x-rays, some averaging, but no compensation of the SAW-induced dynamic XMLD contrast occurs, i.e., all contrast changes indicated in the fourth row of Fig. S1 are zero or positive.

In order to calculate the amplitude of the wave like XMLD contrast under SAW for a given domain we start with XMLD contrast:

$$\text{XMLD} = A \sin^2(\theta) \quad (3)$$

where θ is the angle between the spin axis and x-ray (in-plane projection). If $\theta = 0^\circ$, $\text{XMLD} = 0$, if $\theta = 90^\circ$, $\text{XMLD} = A$. To determine A , we consider the static domain contrast. For the moment, we consider for 90° , i.e. $\theta = 90 + \alpha$. Since we are interested in the measured amplitude of the dynamic XMLD contrast we assume the maximum difference in eq. (1) by comparing

$$\alpha' = \alpha + 2\phi_0 \sin \alpha \cos \alpha \quad (4)$$

$$\alpha' = \alpha - 2\phi_0 \sin \alpha \cos \alpha \quad (5)$$

to calculate the dynamic XMLD contrast for a given domain by inserting into eq. (3):

$$\Delta\text{XMLD} = A \sin^2(90 + \alpha + 2\phi_0 \sin \alpha \cos \alpha) - A \sin^2(90 + \alpha - 2\phi_0 \sin \alpha \cos \alpha) \quad (6)$$

$$= A \cos^2(\alpha + 2\phi_0 \sin \alpha \cos \alpha) - A \cos^2(\alpha - 2\phi_0 \sin \alpha \cos \alpha) \quad (7)$$

Since the spin axis rotation amplitude is small, we develop for

$$\epsilon = 2\phi_0 \sin \alpha \cos \alpha \quad (8)$$

$$\begin{aligned}\cos(\alpha \pm \epsilon) &= \cos \alpha \pm \epsilon \left. \frac{d \cos \beta}{d\beta} \right|_{\beta=\alpha} \\ &= \cos \alpha \mp \epsilon \sin \alpha.\end{aligned}\tag{9}$$

Eq. (7) is therefore approximated by:

$$\Delta\text{XMLD} = A [(\cos \alpha - \epsilon \sin \alpha)^2 - (\cos \alpha + \epsilon \sin \alpha)^2]\tag{10}$$

Employing $(a + b)^2 - (a - b)^2 = -4ab$, eq. (10) reduces to

$$\Delta\text{XMLD} = -4A\epsilon \cos \alpha \sin \alpha.\tag{11}$$

Substituting eq.(11) and (8) as well as $D(\alpha) = \frac{1}{\pi}$ into eq. (2):

$$\begin{aligned}\Delta\text{XMLD}_{\text{avg}} &= \frac{A}{\pi} \int_0^\pi -4 \cos \alpha \sin \alpha \cdot 2\phi_0 \sin \alpha \cos \alpha d\alpha \\ &= -\frac{8A}{\pi} \phi_0 \int_0^\pi \sin^2 \alpha \cos^2 \alpha d\alpha\end{aligned}\tag{12}$$

After solving the integration we get for the wave amplitude, normalized to the domain contrast:

$$\frac{\Delta\text{XMLD}_{\text{avg}}}{A} = -\frac{8}{\pi} \phi_0 \left[\frac{\alpha}{8} - \frac{\sin(4\alpha)}{32} \right]_0^\pi = -\phi_0\tag{13}$$

where A is the difference in a simple XMLD image between 0° and 90° domains. For the experiments performed with a different X ray incidence angle, $\theta = 65^\circ$, the maximum dynamic XMLD contrast as in eq. (7) will now take the form:

$$\Delta\text{XMLD} = A \sin^2(65 - \alpha + \epsilon) - A \sin^2(65 - \alpha - \epsilon).\tag{14}$$

which is calculated in a similar manner as above. We use now:

$$\begin{aligned}\sin(65 - \alpha \pm \epsilon) &= \sin(65 - \alpha) \pm \epsilon \left. \frac{d \sin \beta}{d\beta} \right|_{\beta=65-\alpha} \\ &= \sin(65 - \alpha) \pm \epsilon \cdot \cos(65 + \alpha).\end{aligned}\tag{15}$$

Combining (14) and (15), we get:

$$\Delta\text{XMLD} = 4A\epsilon \cdot \sin(65 - \alpha) \cos(65 + \alpha).\tag{16}$$

Substituting eq. (16) and the value of ϵ into eq. (2), we get:

$$\frac{\Delta\text{XMLD}_{\text{avg}}}{A} = \frac{8}{\pi} \phi_0 \int_0^\pi \cos(65 + \alpha) \sin(65 - \alpha) \sin \alpha \cos \alpha d\alpha.\tag{17}$$

Using for the R.H.S.:

$$\cos(65 + \alpha) = \cos(65) \cos \alpha - \sin(65) \sin \alpha \quad (18)$$

$$\sin(65 - \alpha) = \sin(65) \cos \alpha - \cos(65) \sin \alpha. \quad (19)$$

Eq. (17) can be written as:

$$\begin{aligned} \frac{\Delta \text{XMLD}_{\text{avg}}}{A} &= \frac{8}{\pi} \phi_0 \int_0^\pi [\cos(65) \cos(\alpha) - \sin(65) \sin(\alpha)] \\ &\quad \times [\sin(65) \cos(\alpha) - \cos(65) \sin(\alpha)] \cdot \sin(\alpha) \cos(\alpha) d\alpha \\ &= \frac{8}{\pi} \phi_0 \int_0^\pi [\sin(\alpha) \cdot \cos^3(\alpha) \cos(65) \sin(65) + \sin^2(\alpha) \cos^2(\alpha) \cos^2(65) \\ &\quad - \sin^2(\alpha) \cos^2(\alpha) \sin^2(65) - \sin^3(\alpha) \cos(\alpha) \sin(65) \cos(65)] d\alpha \quad (20) \\ &= \frac{8}{\pi} \phi_0 \left[0.383 \frac{1}{4} \cos^4 \alpha \Big|_0^\pi + 0.179 \left(\frac{1}{8} \alpha - \frac{1}{32} \sin(4\alpha) \right) \Big|_0^\pi - 1 \right. \\ &\quad \left. + 0.821 \left(\frac{1}{8} \alpha - \frac{1}{32} \sin(4\alpha) \right) \Big|_0^\pi - 0.383 \frac{1}{4} \sin^4 \alpha \Big|_0^\pi \right] \\ &= 0.179 \phi_0 - 0.821 \phi_0 = -0.642 \phi_0. \end{aligned}$$

-
- [1] M. J. Grzybowski, P. Wadley, K. W. Edmonds, R. Beardsley, V. Hills, R. P. Champion, B. L. Gallagher, J. S. Chauhan, V. Novak, T. Jungwirth, F. Maccherozzi, and S. S. Dhesi, Imaging current-induced switching of antiferromagnetic domains in cumnas, *Phys. Rev. Lett.* **118**, 057701 (2017).
- [2] B. Casals, N. Statuto, M. Foerster, A. Hernández-Mínguez, R. Cichelero, P. Manshausen, A. Mandziak, L. Aballe, J. M. Hernández, and F. Macià, Generation and imaging of magnetoacoustic waves over millimeter distances, *Physical Review Letters* **124**, 137202 (2020).
- [3] M. Rovirola, M. W. Khaliq, B. Casals, M. Foerster, M. A. Niño, J. Herfort, J. M. Hernández, F. Macià, and A. Hernández-Mínguez, Resonant and off-resonant magnetoacoustic waves in epitaxial Fe₃Si/GaAs hybrid structures (2022), arXiv:2212.07994 [cond-mat.mtrl-sci].

ARTICLE – 6.2

GHz sample excitation at the ALBA-PEEM

M. Waqas Khaliq^{1,2,*}, José M. Álvarez¹, Antonio Camps¹, Nahikari González¹, José Ferrer¹, Ana Martinez-Carboneres³, Jordi Prat¹, Sandra Ruiz-Gómez⁴, Miguel Angel Niño¹, Ferran Macià^{2,5}, Lucia Aballe¹, and Michael Foerster^{1,*}

¹ ALBA Synchrotron Light Facility, Carrer de la Llum, 2 – 26, 08290 Cerdanyola del Valles, Barcelona, Spain.

² Department of Condensed Matter Physics, University of Barcelona, 08028 Barcelona, Spain.

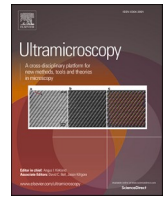
³ MAX IV Laboratory, Fotongatan 2, 224 84 Lund, Sweden

⁴ Max Planck Institute for Chemical Physics of Solids, Noethnitzer Str. 40, 01187 Dresden, Germany.

⁵ Institute of Nanoscience and Nanotechnology (IN2UB), University of Barcelona, 08028 Barcelona, Spain.

Ultramicroscopy **250** (2023) 113757

<https://doi.org/10.1016/j.ultramic.2023.113757>



GHz sample excitation at the ALBA-PEEM

Muhammad Waqas Khaliq^{a,b,*}, José M. Álvarez^a, Antonio Camps^a, Nahikari González^a, José Ferrer^a, Ana Martínez-Carboneres^c, Jordi Prat^a, Sandra Ruiz-Gómez^d, Miguel Angel Niño^a, Ferran Macià^{b,e}, Lucia Aballe^a, Michael Foerster^{a,*}

^a ALBA Synchrotron Light Facility, Carrer de la Llum, 2 – 26, Cerdanyola del Vallés, 08290 Barcelona, Spain

^b Department of Condensed Matter Physics, University of Barcelona, Barcelona, 08028 Spain

^c MAX IV Laboratory, Fotongatan 2, 224 84 Lund, Sweden

^d Max Planck Institute for Chemical Physics of Solids, Noethnitzer Str. 40, 01187 Dresden, Germany

^e Institute of Nanoscience and Nanotechnology (IN2UB), University of Barcelona, 08028 Barcelona, Spain

ARTICLE INFO

Keywords:

Cathode lens microscopy
LEEM-PEEM
Sample environment
High frequency electrical excitations
Electronic modules

ABSTRACT

We describe a setup that is used for high-frequency electrical sample excitation in a cathode lens electron microscope with the sample stage at high voltage as used in many synchrotron light sources. Electrical signals are transmitted by dedicated high-frequency components to the printed circuit board supporting the sample. Sub-miniature push-on connectors (SMP) are used to realize the connection in the ultra-high vacuum chamber, bypassing the standard feedthrough. A bandwidth up to 4 GHz with -6 dB attenuation was measured at the sample position, which allows to apply sub-nanosecond pulses. We describe different electronic sample excitation schemes and demonstrate a spatial resolution of 56 nm employing the new setup.

1. Introduction

Photoemission electron microscopy (PEEM) is a powerful surface characterization technique, especially when coupled to a synchrotron X-ray beamline (XPEEM mode) in order to excite electrons from the sample [1]. Many instruments in use around the world are based on a low energy electron microscope (LEEM) setup [2], where the sample stage is held at negative high voltage (extractor voltage) with respect to the cathode lens (at ground potential). The accelerating voltage is a requisite for the electron microscope operation, where the image resolution depends on the accelerating electric field. Although this scheme is the most common, other instruments keep the sample at ground potential and the electron optics at high positive potential to perform the imaging [3,4]. For this other type of instruments, i.e., sample stage at ground potential, electrical connections to the stage are arguably easier and high-frequency (HF) options have been already reported [5].

The PEEM at the CIRCE beamline of the ALBA Synchrotron is based on an Elmitec LEEM-III microscope with sample stage at high voltage and is in operation since 2012 [6]. The standard four electrical contacts to the sample in this instrument are normally used for heating and temperature readout (thermocouple) and are not optimized for high frequency signal up to the GHz range. The ALBA setup disposes of two

additional DC contacts, often used for electric sample excitation [7]. All electrical feedthroughs into the ultra-high vacuum (UHV), are integrated into a ceramic block permanently welded onto the sample stage. Although the external cables running from the supply rack to the instrument were upgraded to coaxial types [7], the UHV feedthroughs and the signal path inside the sample holder cartridge itself are not impedance-matched with the coaxial cables, and act as a bottleneck for the high frequency signal transmission.

There are two common experiments requiring high-frequency contacts to the sample: short (few nanoseconds and below) electrical pulses, and high-frequency continuous excitation. Short pulses are used either for static (before-after) or for time-resolved (pump-probe) measurements [8–11] generated either directly by pulse generators or from optically triggered switches close to the sample, while continuous signals are typically restricted to time- or phase- resolved experiments. For example, in order to observe current induced domain wall motion in magnetic nanowires [12,13] or Skyrmion motion in flat stripes [14], short high-current density pulses were applied in XPEEM using a setup similar to Ref. [15]. When comparing images taken before and after the pulse, shorter pulses permit a more precise measurement of the motion velocity because imperfections in the samples can act as pinning sites and lead to a systematic underestimation of the speed [12]. Even shorter

* Corresponding authors at: ALBA Synchrotron Light Facility, Carrer de la Llum, 2 – 26, Cerdanyola del Valles, Barcelona 08290, Spain
E-mail addresses: mkhaliq@cells.es (M.W. Khaliq), mfoerster@cells.es (M. Foerster).

<https://doi.org/10.1016/j.ultramic.2023.113757>

Received 8 December 2022; Received in revised form 14 April 2023; Accepted 8 May 2023

Available online 9 May 2023

0304-3991/© 2023 Elsevier B.V. All rights reserved.

current pulses are available in other techniques, for example, the generation and the dynamics of skyrmions have been illustrated with the nanosecond current pulses in symmetric bilayers employing AFM [16], and in chiral-lattice magnet by Lorentz Transmission Electron Microscope [17]. Time resolved STXM has been used to visualize the Skyrmion Hall effect [18]. Additionally, the orbit of a magnetic vortex under current excitation has been observed by ultrafast Lorentz microscopy [19].

Examples of continuous excitation, using periodical HF signals, are XPEEM experiments with surface acoustic waves (SAW) [20–24]. Some experiments are still possible using the standard feedthroughs up to 500 MHz, matching the ALBA X-ray repetition rate. Lower sub harmonics (125 MHz, 250 MHz) can be accessed in combination with a gating system in the electron beam path [20]. Although at 500 MHz, only few percent of the original RF power arrives to the sample, effects driven by the dynamic strain of the SAW like magnetic domain wall motion and their delay [21,22], magneto-acoustic waves [23] and work function oscillations in Pt [24] have been observed. However, dynamical effects at higher frequencies, like the intrinsic ferromagnetic resonance (FMR), have remained elusive due to the continued fast decay of transmission in that range [7].

In this manuscript we describe the design and operation of a high-frequency setup using additional cabling and bypassing the standard feedthrough in order to allow the use of dedicated high-frequency compatible components all the way to the printed circuit boards (PCBs) supporting the sample. The bandwidth extends well into the GHz range. In order to mitigate the pertinent issue of high-voltage arcs between sample and cathode lens, posing any electronics connected to the sample stage at risk of damage, modular and comparatively low-cost electronics are used. A spatial resolution of 56 nm has been demonstrated using the new setup and a reduced electric accelerating field (large distance between the objective lens and sample), as is typically used for this type of experiments. Furthermore, this work has also been granted as a patent in Spain [25].

2. High-Frequency (HF) setup

The new setup has been developed to be compatible with the existing XPEEM station at the CIRCE Beamline at the ALBA Synchrotron Facility. It constitutes a modular addition, i.e., it can be separately mounted and dismounted without breaking the chamber vacuum using a pumpable gate valve. A single permanent modification of the existing setup was the removal of a mu-metal shield around the objective lens. The setup comprises additional coaxial cables and SMP plugs to realize a connection to a printed circuit board integrated into the sample holder (Fig. 1), all made with UHV compatible materials. The design details and electrical characteristics are described below.

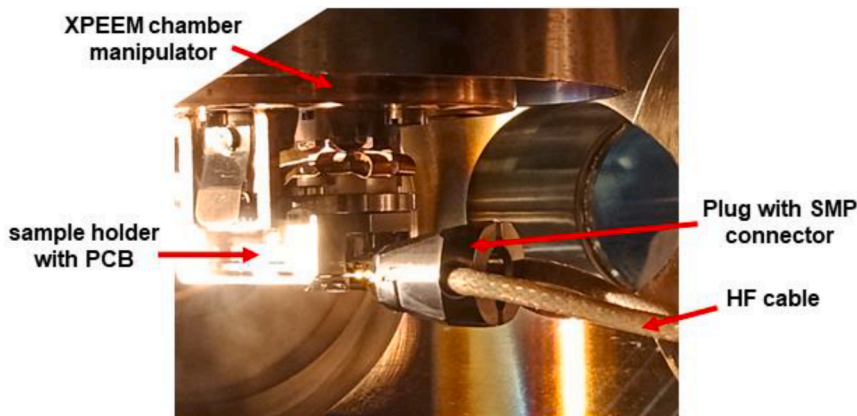


Fig. 1. Connection scheme between the sample holder and the high frequency cable inside the XPEEM chamber. The cable provides a signal path to the sample through a plug that contains two SMP connectors.

2.1. HF cable and plug

A schematic illustration of the HF setup together with pictures of the designed set up is depicted in Fig. 2. It is a long Y-shaped assembly using CF 40 UHV components. As can be seen in the picture, the opening on one side contains the electrical vacuum feedthrough (Sub-Miniature version A, SMA, standard) while the other is fitted with a wobble stick that serves to engage and disengage the plug, which connects the cables with the sample holder. The connection between feedthrough and plug is made by coaxial Teflon isolated cables (Allectra, model: 312-PTFE50-S). A thin (1.8 mm) version was selected due to its better flexibility despite having slightly higher electrical losses than the thicker versions. The central section of the setup comprises a vacuum bellow, which compensates the travel of the setup between the retracted position (behind the gate valve) and the position in contact with the sample stage. In this way the in-vacuum cabling does not fold or stretch, a critical point since the cable reference potential is the high voltage of the sample stage, while the outer assembly is at ground potential. A set of polyether ether keton (PEEK) insulators is placed inside the new setup at various points to further avoid the contact of the HF cable with the inner metallic walls of the system. On the other hand, the SMA feedthrough itself is also at high-voltage potential and electrically separated from the rest by a ceramic break.

2.2. Sample holder and compatible PCB design

In order to transmit the HF signal to the sample, dedicated PCBs compatible with UHV have been designed (See Fig. 3a). The SMP male connectors are directly soldered to the PCB. Samples are glued by silver paste onto the central area of the PCB and electrical contacts realized with ultrasonic wire bonds. The SMP counterpart is integrated into the plug at the end of the cable, shown in Fig. 2c. Fig. 3b shows a combined image of the sample holder with a mounted sample, without (left) and with (right) sample holder cap. The modified cap has cut-outs for the bulky SMP connectors and a central hole for imaging. Its lower surface has to be separated from the sample surface to avoid short circuits with the wire bonds, the same procedure as for low-frequency electrical sample connections [7]. The sample holder is compatible with the incorporation of a small electromagnet below the PCB.

2.3. Electrical characterization

Fig. 4 shows the electrical characterization of the HF connection in blue color compared to the old setup in black (standard vacuum feedthrough and sample holder, but with the same HF PCB and with coaxial cables on the air side). In panel a) of Fig. 4, the transmitted signals (S_{12}) measured with a network analyzer (Keysight FieldFox N9913A with -6

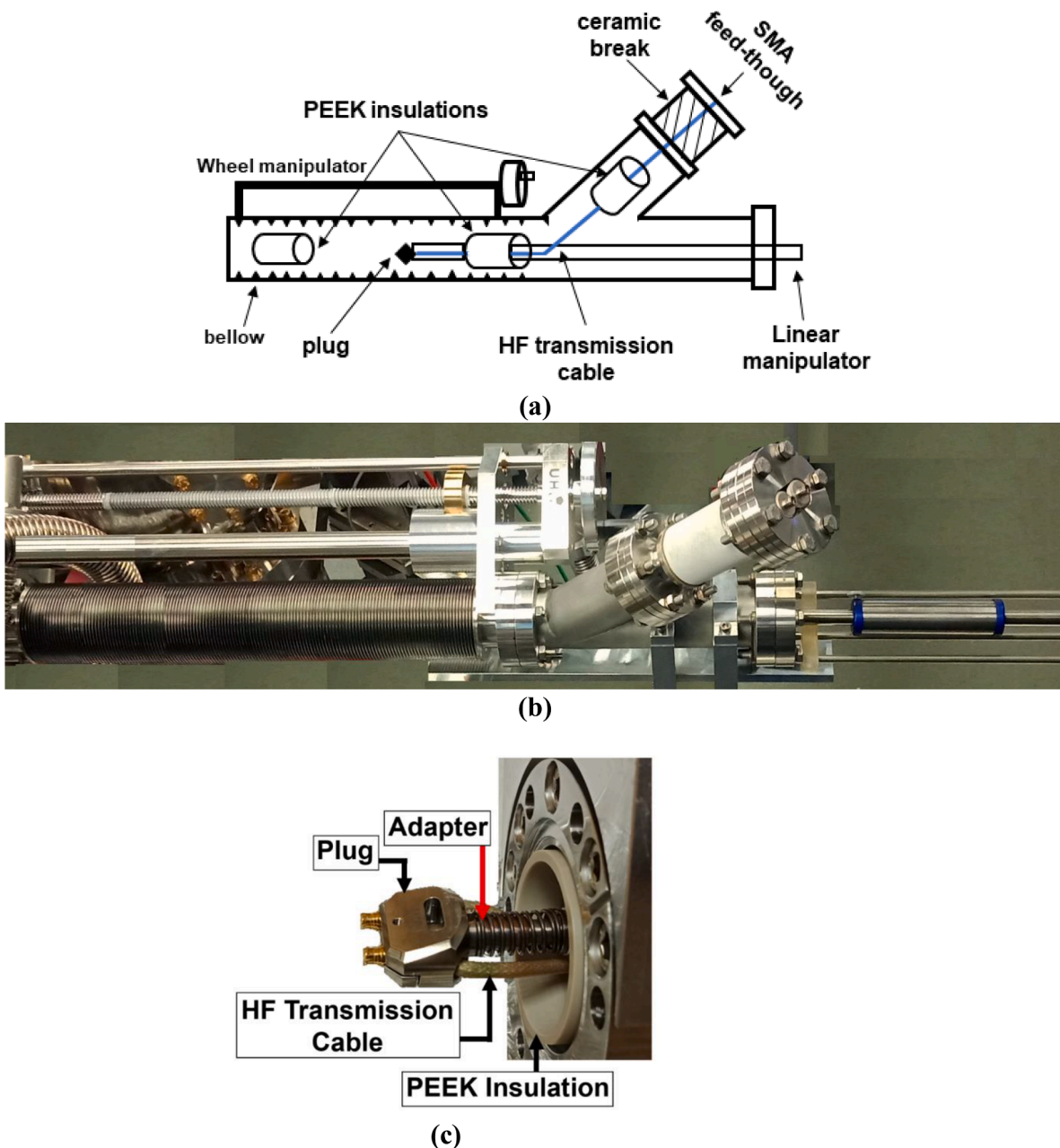


Fig. 2. a. Schematic illustration of the HF setup depicting the various components b. real view, c. side-view of the plug connected to linear manipulator through an adapter. The plug incorporates SMP connectors which link the cable to the printed circuit board in the sample holder.

dBm excitation power) are shown. For these measurements, the transmitted signal is passing directly through the coplanar electrode on the PCB (no sample or wirebonds) and includes two coaxial connections which can be used, for example, as an in and output of a signal (transmission). Thus, the signal attenuation at the sample level corresponds to about one half of the total attenuation of S_{12} . S_{ij} is defined as the ratio of signal power measured in port i of a network analyzer vs the signal power sourced from port j . This means that S_{12} corresponds to the transmission through our setup, where port 1 and port 2 are connected to two coaxial cable system. Both measurements were taken including the high voltage cable (depicted in Fig. 5 with black meshed structure) between the PEEM main HV rack and the microscope itself. While the old setup shows strong attenuation already in the MHz range, the useful bandwidth of the new setup is strongly improved, reaching into the low GHz range. We would like to stress that this is achieved by combining standard-of-the-shelf HF components into an assembly compatible with

the PEEM instrument operating conditions (HV and UHV). As an application example, in the inset of Fig. 4a the measurement of a LiNbO_3 sample with a SAW antenna and receiver (opposing interdigital transducers, IDTs) is shown. The characteristics of the sample with transmission peaks at the resonance frequencies of the IDTs are clearly visible. No comparable data can be obtained with the old setup, despite the fact that we have used it successfully in the past for experiments with SAW from 125 to 500 MHz. Concerning short electrical pulses, Fig. 4b depicts measurements performed with a pulse generator (as discussed in the next section) and oscilloscope. For a pulse of about 1 ns width, the new setup provides clearly improved transmission, although it still causes some attenuation and peak broadening. The results of the electrical characterization are summarized in Table 1.

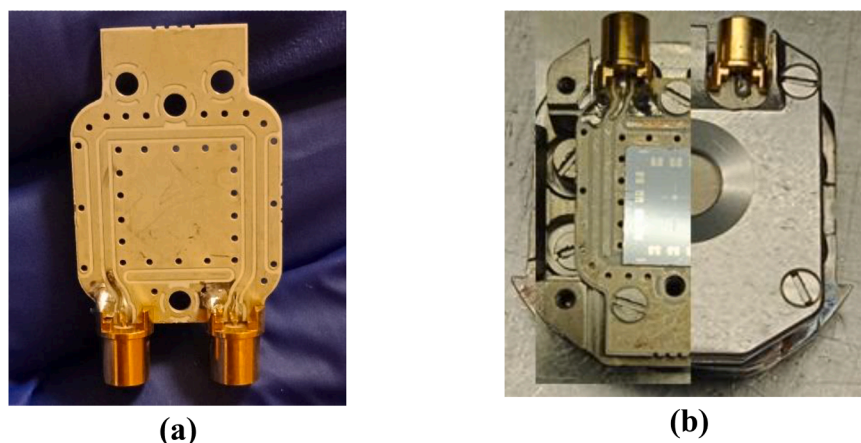


Fig. 3. a. PCB soldered with SMP connector through which the signal is transmitted to the sample, and b. Sample mounted on the PCB in the sample holder.

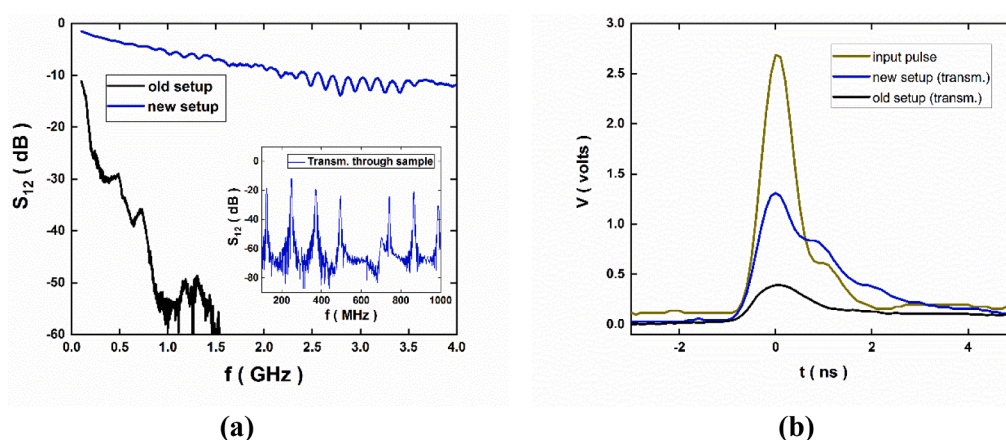


Fig. 4. a. HF signal transmission through the new (blue) and old (black) setup. Inset: characterization of a LiNbO_3 sample SAW transmission filter inside the PEEM sample stage. b. Output comparison of transmitted nanosecond current pulses through a 50 Ohm load for both setups.

3. Electronic equipment

Two different modular electronic systems are utilized to provide the high-frequency electric signals in the PEEM HV environment. Due to the pertinent risk of arcs in the PEEM microscope, which may cause damage to the electronics connected to the sample, a modular approach comprising simple electronic equipment has been adopted. Any connections from outside environment like a master clock into the HV rack need to provide galvanic separation of at least 10 kV and are therefore typically realized by optical fibers. The systems for synchronized sinusoidal signals and for single nanosecond pulses are illustrated in Figs. 5a and 5b, respectively.

The first system (see Fig. 5a) uses a Keysight EXG Vector signal generator model N5172B (RF generator) to capture the synchrotron master clock from a digital signal distributed to all ALBA beamlines by optical fiber [26,27]. The RF generator produces a phase-synchronized analog sinusoidal signals with adjustable phase and power between 1.115 MHz (ALBA orbit clock) and 1 GHz. The ALBA photon bunch repetition rate is around 500 MHz, determined by the radio frequency accelerating cavities. The analog signal from the RF generator is transmitted via an optical fiber link designed at ALBA [28] into the PEEM high-voltage rack, where it is converted back to an electrical signal. Depending on the desired signal, different treatment such as pre-amplification, filtering and frequency multiplication is performed at low level before the final, universal high-power amplifier (Mini-Circuits ZHL-5W-422+). For example, in order to generate a 3 GHz signal, a starting frequency of 750 MHz is used, which is then amplified and

doubled twice, with bandpass filters included after each doubling.

The system for applying short current pulses is shown in Fig. 5b. In its core, an AVTECH AVI-MP-P pulse generator provides short pulses (2-100 ns, 40 V) at an exceptional cost factor, at the expense of some flexibility (unipolar, fixed amplitude, and pulse width determined by the length of attached cable). The pulse generator is followed by either a fixed or a remote programmable attenuator (Mini-Circuits RCDAT-3000-63W2) which is controlled from a computer through an optical fiber. The pulse generator is controlled by an external trigger (here Keysight function generator 33220A) and needs an external power supply. The pulse transmitted through the sample can be analyzed by an oscilloscope.

4. Measurement examples and spatial resolution

As an example of data obtained using the high-frequency connection we present here the excitation of SAW of different frequencies in LiNbO_3 . SAW show a strong and detectable XPEEM signal in phase-synchronized measurements [29]. These waves are generated by interdigitated transducer electrodes (IDT) at the edge of the sample and can travel several millimeters until the PEEM field of view where the measurements are performed. We focus here on the SAW direct electric contrast in the LiNbO_3 substrate, i.e. the oscillation of the local surface potential. Fig. 6a and b show images of SAW at 1 GHz and 3 GHz with associated wavelengths of 4 μm and 1.3 μm , respectively. The electronic setup depicted in Fig. 5a was used, without/with frequency multiplier to yield a 1/3 GHz. 3 GHz signal is obtained by 2 steps of frequency

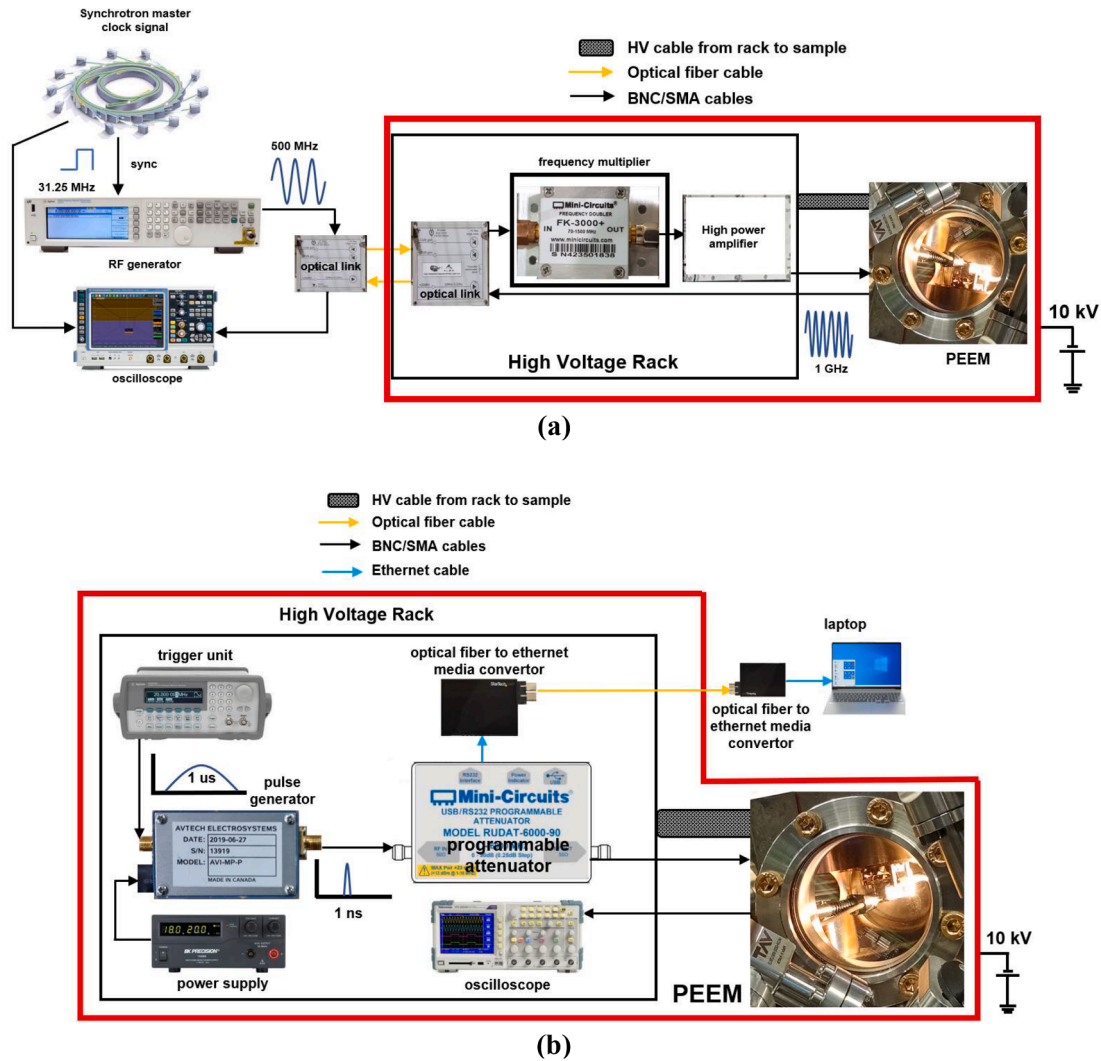


Fig. 5. a. Electronic system used for transmitting HF continuous sinusoidal signals into the sample in XPEEM, b. electronic system to apply single nanosecond pulse to the sample in XPEEM. The trigger unit can be operated manually or via optical fiber.

Table 1

Comparison of the signal attenuation in transmission through old and new setups. All measurements include cables from the rack to the microscope and use the same PCB as load.

Signal	New Setup S_{12} (dB)	Standard feedthrough with RG 178 cable in air S_{12} (dB)
0.5 GHz	-3.6	-30.0
1.0 GHz	-5.6	N/A
4.0 GHz	-11.9	N/A
1 ns pulse	-6.2	-16.3

doubling from 750 MHz signal. In order to measure the SAW electric amplitude, image sequences with varying sample bias voltage were acquired, which corresponds to the nominal kinetic energy of the detected photoemitted electrons. In particular, we scan around the low-energy photoelectron cutoff. For insulating samples, such as LiNbO_3 , a local shift of the sample surface potential, e.g. due to the SAW, will result in a shift of the full electron spectrum, visible as spatial intensity modulations in XPEEM images [24]. The spectra extracted for red and blue boxes depicted in Fig. 6a and b are plotted in Fig. 6c and d, showing a 1 V amplitude for 1 GHz and a smaller 0.09 V for 3 GHz, mainly due to the decreasing IDT efficiency (due to the nonlinear dispersion relation of

LiNbO_3 , the second harmonic at 3 GHz is no longer tuned to an exact multiple of the 500 MHz and thus the IDT has to be operated at the limit of its resonance).

We now analyze the performance of the new setup in terms of spatial resolution. The ultimate spatial resolution in XPEEM has been reported in the 20-30 nanometer range [6] and can be limited by several factors: quality of the electron optics, apertures and alignment, mechanical stability of the sample, detector sensitivity as well as the space charge of the electron bunches travelling inside the microscope [30,31]. In practice, experiments involving electrical contacts on the sample surface such as electrodes or IDTs, typically use a reduced accelerating field to avoid arcs. The reasoning for this compromise in image quality is twofold; on the one hand the inclusion of electrical contacts on the sample surface and the gap between the cap and the sample could increase the risk of arcs for a given setting. On the other hand, electrode structures on the sample are typically destroyed by the very first arc, making it even more crucial than for homogenous samples to avoid arcs. The accelerating field is usually reduced by a factor 3-4 with respect to high-resolution imaging in order to reduce the risks of arcs between sample holder and objective lens. This is done by reducing the high voltage to 10 kV and increasing the sample distance from objective lens. On the one hand, arcs are more likely for many functional sample environments due to non-flat surfaces, insulating regions and/or degassing elements such as small electromagnets. On the other hand, contacted

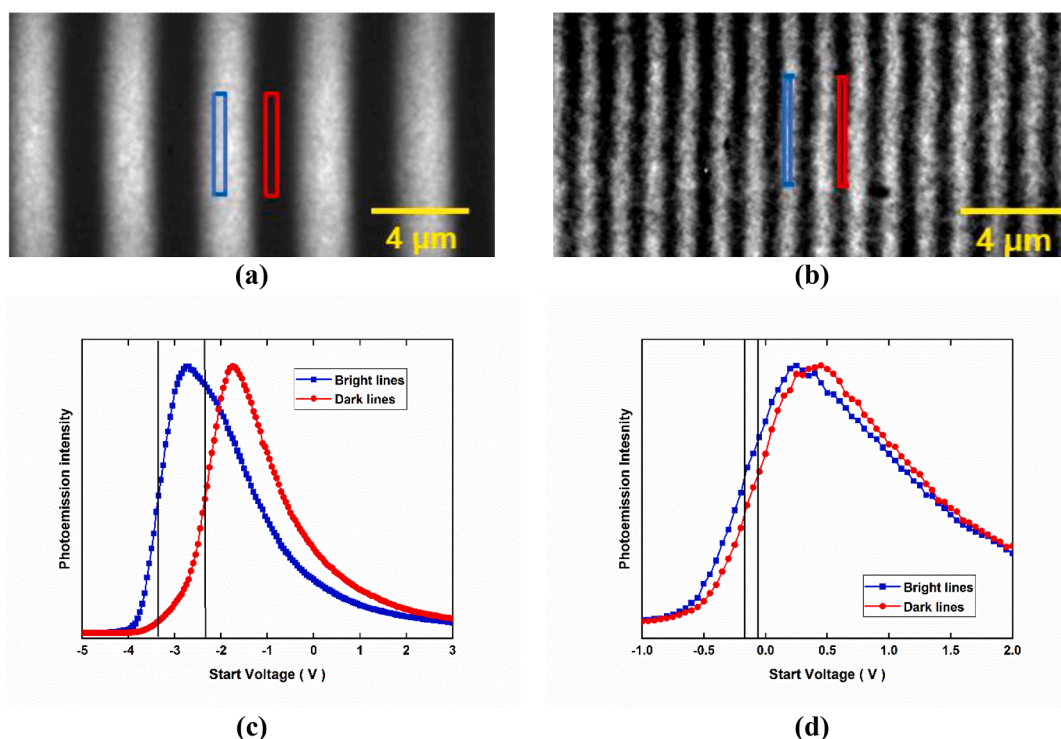


Fig. 6. a & b XPEEM images of SAW in LiNbO₃ at 1 GHz and 3 GHz, respectively. c & d Determination of the SAW electrical amplitude in the PEEM field of view. The average intensity (emitted electrons) of the red and blue boxes in (a) and (b) is shown as function of the sample bias (nominal electron kinetic energy). The shift between the spectra corresponds to the out of plane electrical amplitude of the SAW.

electrode structures on the sample are often destroyed by the very first arc event, probably due to the transient potential difference between different areas of the sample, which gives rise to equilibrating currents. Fig. 7a shows an XPEEM image of a defect in a Co layer on a Si substrate, measured with the high frequency cable connected, at 10 kV operating voltage, 60% increased sample-objective distance and a floating cap; which are the typical parameters for experiments with active electrodes on the sample surface. The spatial resolution defined as 15–85% edge jump was determined to be 56 nm from the line profile in Fig. 7b and was equal to the one obtained without the HF cable on the same day.

5. Conclusions

We presented a new setup to provide high-frequency electrical signals to the high-voltage sample stage of the ALBA XPEEM. The setup can be mounted and dismantled without modification of the main system or breaking the vacuum. The two lateral cable connections terminate in

SMP connectors making a contact with counterparts at the PCB integrated in the sample holder. The measured bandwidth extends up to 4 GHz (-5.9 dB for one pass). Modular electronic systems are used for the generation of continuous and pulsed signals. A lateral resolution of 56 nm has been demonstrated in a routine measurement with typical settings for experiments employing on-sample electrodes. The setup, together with the recently installed electron gating system [10], provides excellent conditions for time resolved XPEEM measurements, for example to study the interaction of magnetic systems with high frequency SAW [32–35]. In addition, the application of shorter current pulses is now possible in a static before-after scheme which allows, for example, to study the effect of these pulses to magnetic domain wall or skyrmion motion.

Declaration of Competing Interest

The authors declare that they have no known competing financial

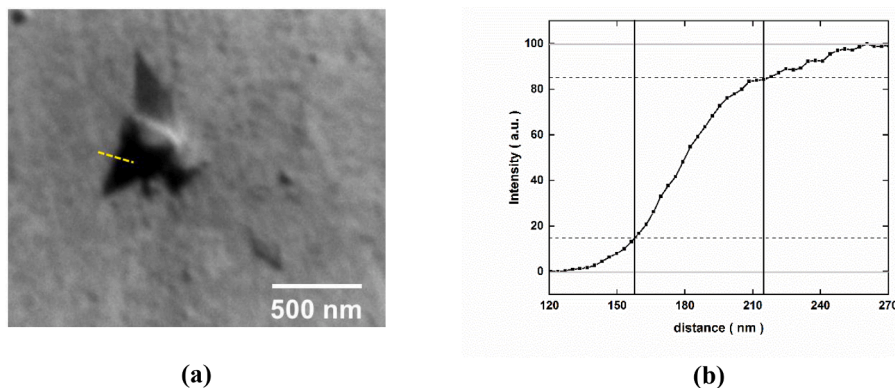


Fig. 7. a. XPEEM image of a defect on a Co/Si sample at reduced acceleration voltage (10 kV) and increased sample objective distance; typical for experiments with injected electrical signals, taken at 777.8 eV photon energy and 1 V start voltage. b. Profile along the dashed yellow line in (a). The width of the grey box is 56 nm.

interests or personal relationships that could have appeared to influence the work reported in this paper.

Data availability

Data will be made available on request.

Acknowledgments

We thank Bernat Molas and Bern Saló i Nevado from the ALBA electronics for their support in designing the PCBs and UHV fine soldering of SMP connectors to PCBs, respectively. Also, Alberto Hernández-Mínguez from Paul-Drude-Institut für Festkörperelektronik for providing lithium niobate samples with IDTs, prepared by Paul Seidel. We gratefully acknowledge the advice and help from the ALBA safety group, namely Ines Perez Renart, Jose Maria Roca, and Carme Mármol Moreno. The authors are also thankful to Spanish Ministry of Science, Innovation, Universities, and DOC-FAM who have received funding from the European Union's Horizon 2020 research and innovation program under the Marie Skłodowska-Curie grant agreement No. 754397. M.W.K., M.F., and M.A. Niño acknowledge the funding from MICINN through grant numbers RTI2018-095303-B-C53 and PID2021-122980OB-C54. F.M. is grateful to funding from MCIN/AEI/10.13039/501100011033 through grant number: PID2020-113024GB-I00. This work has also been supported by the ALBA in-House Research Program.

References

- Th. Schmidt, S. Heun, J. Slezak, J. Diaz, K.C. Prince, G. Lilienkamp, E. Bauer, SPELEEM: combining LEEM and spectroscopic imaging, *Surf. Rev. Lett.* 5 (1998) 1287–1296, <https://doi.org/10.1142/S0218625X98001626>.
- E. Bauer, *Surface Microscopy with Low Energy Electrons*, first ed., Springer, New York, 2014 <https://doi.org/10.1007/978-1-4939-0935-3>.
- R.M. Tromp, J.B. Hannon, A.W. Ellis, W. Wan, A. Berghaus, O. Schaff, A new aberration-corrected, energy-filtered LEEM/PEEM instrument. I. Principles and design, *Ultramicroscopy* 110 (2010) 852–861, <https://doi.org/10.1016/j.ultramic.2010.03.005>.
- E. Bauer, LEEM and UHV-PEEM: a retrospective, *Ultramicroscopy* 119 (2012) 18–23, <https://doi.org/10.1016/j.ultramic.2011.09.006>.
- A. Kaiser, (2009) Magnetization dynamics in magnetically coupled heterostructures (PhD Thesis), Forschungszentrum Jülich, ISBN 978-3-89336-577-7, Volume 5.
- L. Aballe, M. Foerster, E. Pellegrin, J. Nicolas, S. Ferrer, The ALBA spectroscopic LEEM-PEEM experimental station: layout and performance, *J. Sync. Rad.* 22 (2015) 745–752, <https://doi.org/10.1107/S1600577515003537>.
- M. Foerster, J. Prat, V. Massana, N. Gonzalez, A. Fontser, B. Molas, O. Matilla, E. Pellegrin, L. Aballe, Custom sample environments at the ALBA XPEEM, *Ultramicroscopy* 171 (2016) 63–69, <https://doi.org/10.1016/j.ultramic.2016.08.016>.
- J. Vogel, W. Kuch, M. Bonfim, J. Camarero, Y. Pennec, F. Offi, K. Fukumoto, J. Kirschner, A. Fontaine, S. Pizzini, Time-resolved magnetic domain imaging by x-ray photoemission electron microscopy, *Appl. Phys. Lett.* 82 (2003) 2299–2301, <https://doi.org/10.1063/1.1564876>.
- J. Raabe, C. Quitmann, C.H. Back, F. Nolting, S. Johnson, C. Buehler, Quantitative analysis of magnetic excitations in Landau flux-closure structures using synchrotron-radiation microscopy, *Phys. Rev. Lett.* 94 (2005), e217204, <https://doi.org/10.1103/PhysRevLett.94.217204>.
- G. Schönense, H.J. Elmers, S.A. Nepijko, C.M. Schneider, Time-resolved photoemission electron microscopy, *Adv. Imaging Electron Phys.* 142 (2006) 159–223, [https://doi.org/10.1016/S1076-5670\(05\)42003-0](https://doi.org/10.1016/S1076-5670(05)42003-0).
- J. Miguel, J. Sanchez-Barriga, D. Bayer, J. Kurde, B. Heitkamp, M. Piantek, F. Kronast, M. Aeschlimann, H.A. Dürr, W. Kuch, Time-resolved magnetization dynamics of cross-tie domain walls in permalloy microstructures, *J. Phys. Condens. Matter* 21 (2009), e496001, <https://doi.org/10.1088/0953-8984/21/49/496001>.
- M. Schöbitz, A. De Riz, S. Martin, S. Bochmann, C. Thirion, J. Vogel, M. Foerster, L. Aballe, T. O. Menteş, A. Locatelli, F. Genuzio, S. Le-Denmat, L. Cagnon, J. C. Toussaint, D. Gusakova, J. Bachmann, O. Fruchart, Fast domain wall motion governed by topology and crsted fields in cylindrical magnetic nanowires, *Phys. Rev. Lett.* 123 (2019) e21720, <https://doi.org/10.1103/PhysRevLett.123.21720>.
- L. Heyne, J. Rhensius, A. Bisig, S. Krzyk, P. Punke, M. Kläui, L.J. Heyderman, L. Le Guyader, F. Nolting, Direct observation of high velocity current induced domain wall motion, *Appl. Phys. Lett.* 96 (2010), e032504, <https://doi.org/10.1063/1.3291067>.
- R. Juge, S.-G. Je, D. de S. Chaves, L.D. Buda-Prejbeanu, J. Peña-García, J. Nath, I. M. Miron, K.G. Rana, L. Aballe, M. Foerster, F. Genuzio, T.O. Menteş, A. Locatelli, F. Maccherozzi, S.S. Dhesi, M. Belmeguenai, Y. Roussigné, S. Auffret, S. Pizzini, G. Gaudin, J. Vogel, O. Boule, Current-driven skyrmion dynamics and drive-dependent skyrmion Hall effect in an ultrathin film, *Phys. Rev. Appl.* 12 (2019), e044007, <https://doi.org/10.1103/PhysRevApplied.12.044007>.
- L. Heyne, M. Kläui, J. Rhensius, L. Le Guyader, F. Nolting, *In situ* contacting and current-injection into samples in photoemission electron microscopes, *Rev. Sci. Instrum.* 81 (2010), e113707, <https://doi.org/10.1063/1.3495967>.
- A. Hrabec, J. Sampaio, M. Belmeguenai, I. Gross, R. Weil, S.M. Chérif, A. Stashkevich, V. Jacques, A. Thiaville, S. Rohart, Current-induced skyrmion generation and dynamics in symmetric bilayers, *Nat. Commun.* 8 (2017) e15765, <https://doi.org/10.1038/ncomms15765>.
- L. Peng, K. Karube, Y. Taguchi, N. Nagaosa, Y. Tokura, X. Yu, Dynamic transition of current-driven single-skyrmion motion in a room-temperature chiral-lattice magnet, *Nat. Commun.* 12 (1) (2021) e6797, <https://doi.org/10.1038/s41467-021-27073-2>.
- K. Litzius, I. Lemesh, B. Krüger, P. Bassirian, L. Caretta, K. Richter, F. Büttner, K. Sato, O.A. Tretiakov, J. Förster, R.M. Reeve, M. Weigand, I. Bykova, H. Stoll, G. Schütz, G.S.D. Beach, M. Kläui, Skyrmion Hall effect revealed by direct time-resolved X-ray microscopy, *Nat. Phys.* 13 (2017) 170–175, <https://doi.org/10.1038/nphys4000>.
- M. Möller, J.H. Gaida, S. Schäfer, C. Ropers, Few-nm tracking of current-driven magnetic vortex orbits using ultrafast Lorentz microscopy, *Commun. Phys.* 3 (2020) e36, <https://doi.org/10.1038/s42005-020-0301-y>.
- L. Aballe, M. Foerster, M. Cabrejo, J. Prat, P. Pittana, R. Sergio, M. Lucian, M. Barnaba, T.O. Menteş, A. Locatelli, Pulse picking in synchrotron-based XPEEM, *Ultramicroscopy* 202 (2019) 10–17, <https://doi.org/10.1016/j.ultramic.2019.03.011>.
- M. Foerster, L. Aballe, J.M. Hernández, F. Macià, Subnanosecond magnetization dynamics driven by strain waves, *MRS Bull.* 43 (2018) 854–859, <https://doi.org/10.1557/mrs.2018.258>.
- M. Foerster, F. Macià, N. Statuto, S. Finizio, A. Hernández-Mínguez, S. Lendínez, P. V. Santos, J. Fontcuberta, J.M. Hernández, M. Kläui, L. Aballe, Direct imaging of delayed magneto-dynamic modes induced by surface acoustic waves, *Nat. Commun.* 8 (2017) e407, <https://doi.org/10.1038/s41467-017-00456-0>.
- B. Casals, N. Statuto, M. Foerster, A. Hernández-Mínguez, R. Cicheler, P. Manshausen, A. Mandziak, L. Aballe, J.M. Hernández, F. Macià, Generation and imaging of magnetoacoustic waves over millimeter distances, *Phys. Rev. Lett.* 124 (2020), e137202, <https://doi.org/10.1103/PhysRevLett.124.137202>.
- B. von Boehn, M. Foerster, M. von Boehn, J. Prat, F. Macià, B. Casals, M.W. Khaliq, L.A. Hernández-Mínguez, R. Imbihl, On the promotion of catalytic reactions by surface acoustic waves, *Angew. Chem. Int. Ed.* 59 (2020) 20224–20229, <https://doi.org/10.1002/anie.202005883>.
- M. Foerster, L. Aballe, J. Prat, M.W. Khaliq, J.M. Álvarez, and N. González. (2022). Removable connection device for excitation of samples with high-frequency electrical signals to high voltage in electron microscopes (Spanish Patent No. 202030930). Spanish Office of Patents and Trademarks. <http://invenes.oepm.es/InvenesWeb/detalle?referencia=P202030930>.
- O. Matilla, D. Beltran, D. Fernandez-Carreiras, J.J. Jamroz, J. Klor, J. Moldes, R. Sune, ALBA timing system - a known architecture with fast interlock system upgrade, in: *Proceedings of the Contributions to the Proceedings of ICALEPCS 2011*, 2012, p. 1423. France.
- J. Moldes, D. Beltran, D. Fernandez, J. Jamroz, J. Klor, O. Matilla, R. Sune, (2012). The MRF timing system. The complete control software integration in TANGO. *Proceedings of the Contributions to the Proceedings of ICALEPCS 2011*, (p. 1423). France.
- B. Molas, L. Aballe, M. Foerster, A. Fontser, O. Matilla, J. Moldes, Synchrotron master frequency reconstruction for sub-nanosecond time-resolved XMCD-PEEM experiments, *Proceedings of the ICALEPCS 2017*, Barcelona, Spain. 10.18429/JACO-W-ICALPCS2017-THPHA084.
- M. Foerster, N. Statuto, B. Casals, A. Hernández-Mínguez, S. Finizio, A. Mandziak, L. Aballe, J.M. Hernández Ferràs, F. Macià, Quantification of propagating and standing surface acoustic waves by stroboscopic X-ray photoemission electron microscopy, *J. Synchrotron Rad.* 26 (2019) 184–193, <https://doi.org/10.1107/S1600577518015370>.
- A. Locatelli, T.O. Menteş, M.A. Niño, E. Bauer, Image blur and energy broadening effects in XPEEM, *Ultramicroscopy* 111 (2011) 1447–1454, <https://doi.org/10.1016/j.ultramic.2010.12.020>.
- Th. Schmidt, A. Sala, H. Marchetto, E. Umbach, H.J. Freund, First experimental proof for aberration correction in XPEEM: resolution, transmission enhancement, and limitation by space charge effects, *Ultramicroscopy* 126 (2013) 23–32, <https://doi.org/10.1016/j.ultramic.2012.11.004>.
- A. Adhikari, S. Adenwalla, Surface acoustic waves increase magnetic domain wall velocity, *AIP Adv.* 11 (2021), e015234, <https://doi.org/10.1063/9.0000159>.
- J. Tejada, E.M. Chudnovsky, R. Zarzuela, N. Statuto, J. Calvo-de la Rosa, P. V. Santos, A. Hernández-Mínguez, Switching of magnetic moments of nanoparticles by Surface acoustic waves, *EPL* 118 (2017) e37005, <https://doi.org/10.1209/0295-5075/118/37005>.
- Y. Miyazaki, T. Yokouchi, Y. Shiomi, Trapping and manipulating skyrmions in two-dimensional films by surface acoustic waves, *Sci. Rep.* 13 (2023) e1922, <https://doi.org/10.1038/s41598-023-29022-z>.
- F. Guo, Z. Mao, Y. Chen, Z. Xie, J.P. Lata, P. Li, L. Ren, J. Liu, J. Yang, M. Dao, S. Suresh, T.J. Huang, Three-dimensional manipulation of single cells using surface acoustic waves, *Proc. Natl. Acad. Sci.* 113 (6) (2016) 1522–1527, <https://doi.org/10.1073/pnas.152481311>.

ARTICLE – 6.3

Study of the magnetoelastic effect in nickel and cobalt thin films at GHz range using X-ray microscopy

Marc Rovirola^{1,2,*}, **M. Waqas Khaliq**^{1,3,†}, Travis Gustafson⁴, Fiona Sosa¹, Blai Casals^{2,5}, Joan Manel Hernández^{1,2}, Sandra Ruiz-Gómez⁶, Miguel Angel Niño³, Lucía Aballe³, Alberto Hernández-Mínguez⁷, Michael Foerster³, and Ferran Macià^{1,2,‡}

¹ Dept. of Condensed Matter Physics, University of Barcelona, 08028-Barcelona, Spain

² Institute of Nanoscience and Nanotechnology, University of Barcelona, 08028-Barcelona, Spain

³ ALBA Synchrotron Light Facility, 08290-Cerdanyola del Valles, Barcelona, Spain

⁴ Department of Physics, Norwegian University of Science and Technology (NTNU), 7034 Trondheim, Norway

⁵ Dept. of Applied Physics, University of Barcelona, 08028-Barcelona, Spain

⁶ Max Planck Institute for Chemical Physics of Solids, 01187-Dresden, Germany

⁷ Paul Drude Institute for Solid State Electronics, 10117-Berlin, Germany

Physical Review Research **6** (2024) 023285

<https://doi.org/10.1103/PhysRevResearch.6.023285>.

Study of the magnetoelastic effect in nickel and cobalt thin films at GHz range using x-ray microscopy

Marc Rovirola ^{1,2,*} M. Waqas Khaliq ^{1,3,†} Travis Gustafson,⁴ Fiona Sosa-Barth,¹ Blai Casals ^{2,5}
Joan Manel Hernández ^{1,2} Sandra Ruiz-Gómez ⁶ Miguel Angel Niño,³ Lucía Aballe ³ Alberto Hernández-Mínguez ⁷
Michael Foerster ³ and Ferran Macià ^{1,2,‡}

¹Department of Condensed Matter Physics, *University of Barcelona*, 08028 Barcelona, Spain

²Institute of Nanoscience and Nanotechnology (IN2UB), *University of Barcelona*, 08028 Barcelona, Spain

³ALBA Synchrotron Light Source, 08290 Cerdanyola del Vallès, Spain

⁴Department of Physics, *Norwegian University of Science and Technology (NTNU)*, 7034 Trondheim, Norway

⁵Department of Applied Physics, *University of Barcelona*, 08028 Barcelona, Spain

⁶Max Planck Institute for Chemical Physics of Solids, 01187-Dresden, Germany

⁷Paul-Drude-Institut für Festkörperelektronik, Leibniz-Institut im Forschungsverbund Berlin e.V., 10117 Berlin, Germany



(Received 22 December 2023; accepted 8 May 2024; published 17 June 2024)

We use surface acoustic waves of 1 and 3 GHz in hybrid piezoelectric-magnetic systems with either nickel or cobalt as a magnetic layer to generate magnetoacoustic waves and directly image them using stroboscopic x-ray magnetic circular dichroism imaging. Our measurements visualize and quantify the amplitudes of both acoustic and magnetic components of the magnetoacoustic waves, which are generated in the ferromagnetic layer and can propagate over millimeter distances. Additionally, we quantified the magnetoelastic strain component for nickel and cobalt through micromagnetic simulations.

DOI: [10.1103/PhysRevResearch.6.023285](https://doi.org/10.1103/PhysRevResearch.6.023285)

I. INTRODUCTION

There is an increasing interest in manipulating magnetization dynamics to create low-power consumption devices capable of transmitting and encoding information efficiently [1]. A challenge lies in effectively creating and controlling magnetic excitations in nanodevices. The most common way to manipulate magnetization typically involves the use of magnetic fields. However, this approach has several downsides, including issues with nonlocality, and challenges with integrating controllable magnetic fields into micrometer-scale devices. Other approaches explore interactions of conducting electron's spin [2,3], lattice phonons [4,5], or ultrashort light pulses [6] with magnetic excitations. Promising alternatives have been proposed, such as the use of strain. The field of straintronics [4] studies strain-induced effects in solids and special attention is directed to magnetic materials as a promising alternative for reduced energy-consumption devices [7]. Strain couples to magnetic states through the magnetoelastic (ME) effect, which is the change of magnetic properties due to mechanical deformation. This effect has already been proposed and used in many applications [5] including the

reversing magnetization of patterned nanomagnets [8,9] or inducing a phase transition from antiferromagnetic ordering to ferromagnetic ordering [10].

The ME effect can be used to generate spin waves—collective excitations of magnetic order—through surface acoustic waves (SAWs) [11,12], which are strain waves propagating at the surface of a solid. SAWs generate an oscillating strain in both space and time which can create an oscillating magnetic anisotropy field on a magnetostrictive material [13,14]. This dynamic anisotropy field may induce a magnetization variation with the same wavelength and frequency as the SAWs and the excitation may propagate up to millimeter distances [15]. These hybrid waves are referred to as magnetoacoustic waves (MAWs) and have been studied in a wide range of materials by measuring acoustic attenuation as a function of the magnetic state [16–20] or by direct imaging using magneto-optic Kerr effect (MOKE) [20,21] or x-ray magnetic circular dichroism (XMCD) [15,22]. Using the same principles, more recently also Néel vector waves have been observed in antiferromagnetic CuMnAs [23] by x-ray linear dichroism (XLD).

SAWs are typically generated using interdigital transducers (IDTs) deposited on piezoelectric substrates [24]. IDTs are interlocking arrays of metallic electrodes that can excite SAWs up to GHz frequencies. IDTs are used in electronics as radio frequency delay lines and filters and their integration into micrometric devices is well established [25]. SAW-based technology can be efficiently integrated into low-power devices since the SAW amplitude depends on the amplitude of the oscillating voltage applied to the IDT instead of the current.

*marc.rovirola@ub.edu

†mkhaliq@cells.es

‡ferran.macia@ub.edu

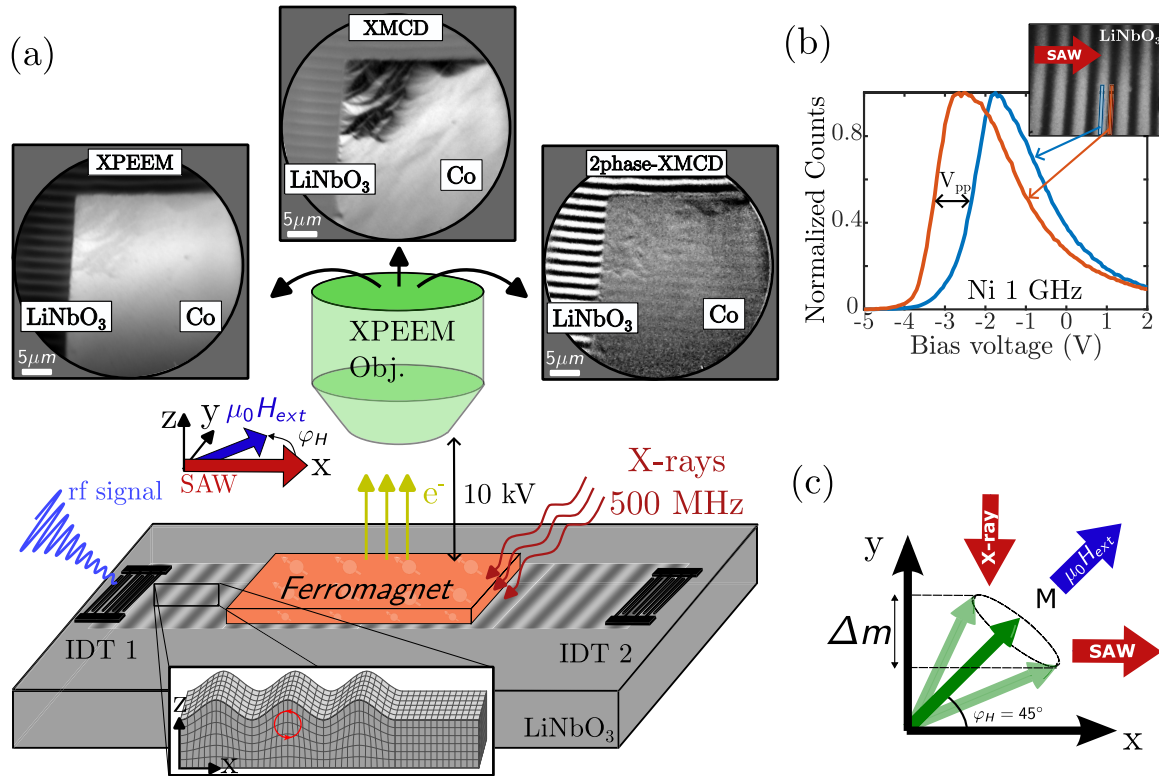


FIG. 1. (a) Schematic of the experimental setup. A thin film of either Ni or Co is grown in the middle of the acoustic path (x - y plane), where SAW propagate along the x direction. The Co sample can only be excited at 1 GHz by either IDT. The microscope (XPEEM Objective) is operated at 10 kV with respect to the sample to accelerate low energy electrons kicked out by the x rays (which are applied along the y axis). From this setup, we can obtain XPEEM and XMCD images. The magnetic field is applied in-plane at an angle $\varphi_H = 45^\circ$ relative to the SAW propagation direction. (b) Local photoelectron energy spectra measured at opposite SAW phases (tensile and compressive). The orange line represents the dark SAW phase, while the blue line represents the bright SAW phase. The x axis depicts the bias voltage applied between the sample and the XPEEM objective; voltage shift between both spectra corresponds to the peak-to-peak SAW piezoelectric voltage, V_{pp} . (c) Representation of the direction of SAW (x direction), magnetic field (45°), and x ray (y direction). In this experiment, the SAW and x ray are perpendicular to each other. The horizontal dashed lines represent the change in magnetization projection captured with the x rays.

Magnetic imaging techniques based on MOKE [26,27] or XMCD [15,22,28] provide the opportunity to directly measure MAWs and thus study the effect of the coupling between strain and spin waves in both space and time. Recent experiments have shown that the ME effect is as efficient in dynamic processes up to 500 MHz as in static processes [28], thus fueling the idea of using SAWs in magnonic applications. Furthermore, experiments on Fe_3Si with cubic anisotropy revealed both resonant and nonresonant MAWs [22] with a noticeable increase in amplitude at resonance. There is thus a need for working at the GHz frequency range where most ferromagnets have internal resonances and where miniaturization of MAWs might meet the requirements for modern technologies [25].

In this paper, we study MAWs at 1 and 3 GHz in nickel (Ni) and MAWs at 1 GHz in cobalt (Co) using stroboscopic x-ray photoemission electron microscopy (XPEEM) combined with XMCD imaging. Our analysis reveals that both Ni and Co exhibit MAWs across a wide range of magnetic fields, with each material displaying different profiles and amplitudes. With the help of micromagnetic simulations, we are able to quantify the strength of the magnetoelastic coupling for both magnetic materials at the studied frequencies.

II. EXPERIMENTAL METHODS

Thin films of polycrystalline Ni and Co with a thickness of 20 nm were grown on the acoustic path of several SAW delay lines by e-beam evaporation. The samples exhibit an in-plane anisotropy with a magnetization saturation of 490 kA/m^3 for Ni and 1510 kA/m^3 for Co. The delay lines consist of pairs of unidirectional IDTs deposited on piezoelectric lithium niobate (128Y-cut $LiNbO_3$) substrates; see Fig. 1. The IDTs are designed to generate SAWs with frequencies of 1 GHz and 3 GHz for the Ni sample and only 1 GHz for the Co sample. These frequencies are conveniently selected to match the synchrotron repetition rate (499.654 MHz), thus allowing for stroboscopic images. To generate SAWs, we excite the IDTs with an oscillating electrical signal of the appropriate frequency that is transformed into strain through the inverse piezoelectric effect [11]. Notice that SAWs are limited to a substrate depth of the order of the SAW wavelength [29], corresponding to $3.8 \mu\text{m}$ and $1.26 \mu\text{m}$ for 1 and 3 GHz, respectively. Within this depth region, the SAW causes a periodic modulation of the crystal lattice in the substrate and on any thin film deposited on its surface. If the thin film is magnetostrictive, then the periodic displacement of atoms caused by the SAWs produces a periodic effective magnetic field in

the thin film as a result of the inverse magnetostrictive effect, commonly referred to as the ME effect.

The experiment was performed at the XPEEM experimental station of the ALBA Synchrotron Light Facility [30]. A schematic representation of the setup is shown in Fig. 1(a). SAWs are emitted in the x direction and are synchronized with the repetition rate of the synchrotron x-ray bunches. This synchronization allows for stroboscopic images at a particular phase of the SAWs. The x rays from the synchrotron are directed onto the sample, knocking out secondary electrons (called photoelectrons). These photoelectrons are then pulled out of the sample by a 10 kV potential difference between the XPEEM objective and the sample. The kinetic energy of these photoelectrons is sensitive to the electrical field at the sample surface. By adjusting a bias voltage at the detector we can scan the photoelectron energy spectrum at the sample surface. Figure 1(b) shows the photoelectron energy spectra at different SAW phases. The shift in energy between phases is directly related to the electric potential generated by the SAWs. However, the metallic nature of the thin films of Ni and Co shields the piezoelectric field within the first nanometers at the bottom of the film and therefore the SAW's electric potential vanishes at the film's top surface. To obtain magnetic contrast, two XPEEM images with opposite circular light polarization (circular left and circular right) are subtracted to obtain an XMCD image. The energy of the x rays is specifically chosen at the L_3 edge of Ni and Co to provide information about the electrons responsible for the magnetization. More details on synchronized SAW stroboscopic XPEEM measurements and the upgraded setup to support >500 MHz excitations can be found elsewhere [31,32]. The insets of Fig. 1(a) display the three imaging modalities of the setup. The top-left corner depicts an XPEEM image with clear SAWs contrast on the LiNbO_3 , accompanied by a weak contrast of magnetic domains on the Co. The top-center depicts an XMCD image that highlights the magnetic contrast on the Co magnetic domains, accompanied by faint traces of residual SAWs on the LiNbO_3 due to thermal drifts in subsequent images (and thus slightly different SAW propagation velocities). The top-right corner depicts a two-phase-XMCD image, which consists of capturing two XPEEM images with a 180-phase shift in SAW for each x-ray helicity, followed by a subtraction between both phases and helicities. This method enhanced both the magnetic and piezoelectric contrast while eliminating static contrast such as magnetic domains, enabling a clearer measurement of MAWs. Figure 1(b) illustrates the local spectra detector counts for Ni at 1 GHz plotted against the bias voltage, which is applied between the sample and the XPEEM objective, at opposite SAW phases, highlighted in orange and blue. The voltage shift between both spectra (V_{pp}) corresponds to the peak-to-peak amplitude of the SAW piezoelectric potential at the surface of the LiNbO_3 substrate. Figure 1(c) shows the directions of the SAW, the magnetic field, and the x rays. The SAW and the magnetic field are at about 45° with respect to each other to exert maximum magnetoelastic torque [33], whereas the SAW and x rays are perpendicular to each other in order to detect the magnetization changes in the y direction as represented by the dashed lines in Fig. 1(c).

III. RESULTS

An initial characterization of the samples was performed to study the angular dependence of their acoustic-ferromagnetic resonance (a-FMR) at 1 GHz. The experiment consists of placing our hybrid device [see Fig. 1(a)] between the poles of an electromagnet and measuring the transmitted acoustic signal between IDT1 and IDT2, S_{21} , with a vector network analyzer at different angles between the SAWs and the in-plane magnetic field. In contrast to FMR, where an rf-magnetic field is used to drive the magnetization into resonance, a-FMR uses the periodic strain field of the SAW to induce magnetization precession by modulating the effective magnetic field of the sample. Additionally, the nonzero wave vector of the SAW must be taken into account in the determination of the resonance magnetic fields and frequencies [17].

The coupling between magnetization and SAWs can generate MAWs under certain conditions of the external magnetic field. At resonance, significant energy is transferred from the SAW to the magnetic system, resulting in SAW attenuation and phase shift that are detected in the S_{21} measurement [16]. The SAW attenuation as a function of the magnitude and angle of the applied magnetic field (in both cases, the magnetic field was swept from negative to positive values) is presented in Fig. 2. In both samples, a large attenuation is observed, regardless of the angle, at a fixed magnetic field that corresponds to the magnetization-switching field of the film. In addition, Ni [Fig. 2(a)] shows the typical fourfold shape with large attenuation between $\pm 30^\circ$ and $\pm 50^\circ$ and a maximum around 45° where the ME torque is the largest [16,33,34]. As the angle between SAW and the magnetic field exceeds 50° or drops below 30° , the attenuation decreases, reaching the minimum ME torque at 0° and 90° . In contrast, the SAW attenuation for Co [Fig. 2(b)] is strongest at magnetic field angles between -30° and 30° , above which the attenuation rapidly decays. Similar results for Co can be found in Ref. [35]. We can see an asymmetric attenuation in the Co sample for both positive and negative fields and positive and negative angles. This nonreciprocal behavior is typically determined by the effective magnetic fields associated with the SAW due to the magnetoelastic and magnetorotation couplings [36–38]. Insets in Figs. 2(a) and 2(b) show S_{21} attenuation at representative angles, where the nonreciprocal effect can be observed, especially for the Co sample.

Prior to capturing XMCD images of the magnetization, the IDTs are tested by measuring the amplitude of the SAW piezoelectric potential according to the method shown in Fig. 1(b). By solving the coupled elastic and electromagnetic equations, we can obtain the amplitude of the strain components, e_{xx} , e_{xz} , and e_{zz} , associated with the SAW images [39,40]. It is important to note that the strain components may vary depending on SAW frequency. Thus we measured the strain component in each sample at the same SAW excitation frequency and power that are employed for the XMCD imaging (see Table I).

In the following sections, we show the results obtained from the XMCD imaging and discuss the amplitude of the MAWs for the different samples and excitation frequencies. To normalize the MAW amplitude, we determine the M_s in units of XMCD contrast from an XMCD image featuring magnetic domains [see Fig. 1(a)]. The contrast difference

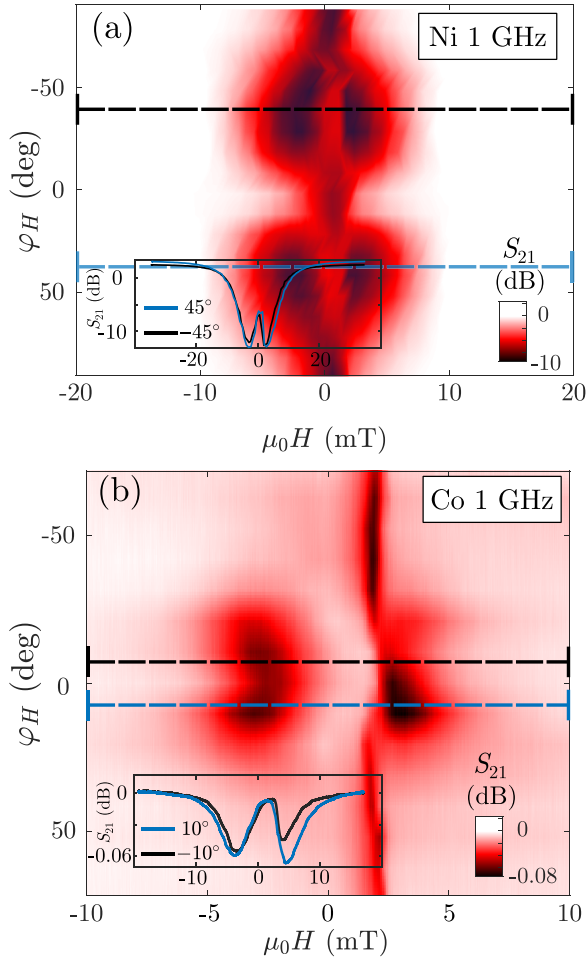


FIG. 2. (a) Ni S_{21} attenuation at 1 GHz for several angles between the SAW and the magnetic field showing different absorption values with a maximum close to 45° and minimums at 0° and above 60° . The inset shows a horizontal cut of S_{21} attenuation for $\varphi_H = 40^\circ$ (black curve) and $\varphi_H = 30^\circ$ (blue curve). (b) Co S_{21} attenuation at 1 GHz for several angles between the SAW and the magnetic field. Co shows absorption when the SAW and the magnetic field are at an angle between -30° and 30° . The insets show a horizontal cut of S_{21} for $\varphi_H = 40^\circ$ (black curve) and $\varphi_H = 30^\circ$ (blue curve).

between opposite magnetizations can be directly linked to the M_s component in the direction of the x rays.

A. MAWs in nickel

The Ni sample was studied for two SAW frequencies: 1 and 3 GHz. Figures 3(a) and 3(b) show two-phase XMCD images

TABLE I. Amplitudes of the SAW strain components for each sample and SAW frequency corresponding to the V_{pp} values obtained from the secondary photoelectron energy spectra.

Sample	$V_{pp}(V)$	$e_{xx}(10^{-5})$	$e_{xy}(10^{-5})$	$e_{zz}(10^{-5})$
Ni (1 GHz)	0.90	14.3	2.95	4.23
Ni (3 GHz)	0.40	19.0	3.93	5.64
Co (1 GHz)	1.05	16.6	3.44	4.93

of excitations of both signals (1 and 3 GHz, respectively). The bottom part of the images corresponds to LiNbO₃ and displays the SAWs and the top part corresponds to Ni and shows the MAWs as indicated. Both images are taken with the same field-of-view ($20 \times 20 \mu\text{m}$) and the same color scale to be able to distinguish the wavelength and the contrast difference. Figure 3(c) shows the MAW profile of both frequencies with their corresponding sinusoidal fit to show the large difference in amplitude (as well as the difference in wavelength). The sinusoidal fits use the amplitude and phase as fitting parameters, while the 1 GHz/3 GHz SAW excitation gives the frequency (and the wavelength). A summary of the normalized MAW amplitudes at different magnetic fields is presented in Fig. 3(d) for 1 GHz (black symbols, left axis) and 3 GHz (orange symbols, right axis). The overall magnetization precession amplitude at 1 GHz is one order of magnitude larger than that of 3 GHz, while the measured strain amplitude at the substrate was similar for the two frequencies; this will be explored in more detail in Sec. IV.

B. MAWs in cobalt

The Co sample was only studied at 1 GHz. Figure 4(a) displays a representative two-phase XMCD image with a field of view of $50 \times 50 \mu\text{m}$, where clear SAWs in LiNbO₃ and MAWs can be observed in Co at 1 GHz. The profile of this MAW is shown in Fig. 4(b) with the corresponding sinusoidal fit. Figure 4(c) collects results from different magnetic field values, without a clear trend but with different amplitudes for opposite magnetic field directions. This nonreciprocal behavior was seen as well in the SAW attenuation measurements shown in Fig. 2(b). We notice here that the studied range of fields is small and one may hint at a slight amplitude increase close to $\mu_0 H = \pm 7 \text{ mT}$. The amplitude of the MAW is two orders of magnitude smaller than Ni at 1 GHz (and even one order smaller than Ni at 3 GHz). We notice here that in both experiments the applied magnetic field formed an angle of $\sim 45^\circ$ with respect to the SAWs which could be outside the region of resonant coupling for Co [see Fig. 2(b)]; we will discuss it in Sec. IV.

IV. DISCUSSION

The experimental techniques employed here measured different quantities; a-FMR determines the attenuation of SAW energy under MAW resonance, while XMCD is a direct representation of the magnetization dynamics in the ferromagnetic film. By comparing our results with micromagnetic simulations, we can determine the efficiency of converting strain into a magnetization variation, thus obtaining the magnetoelastic constants.

The experimental results demonstrate a notable consistency in the behavior of Ni and Co at 1 GHz in both a-FMR and XMCD. Starting with Ni, when placed under a magnetic field at $\varphi_H = 45^\circ$ relative to the SAWs, the effect of the ME coupling is the strongest at approximately $\pm 4 \text{ mT}$ and it decays as the magnetic field strength increases. In the case of Co, the magnetic field that we could apply in XMCD imaging did not exceed 7 mT, limiting our knowledge at higher fields. However, a peak close to 5 mT is observed

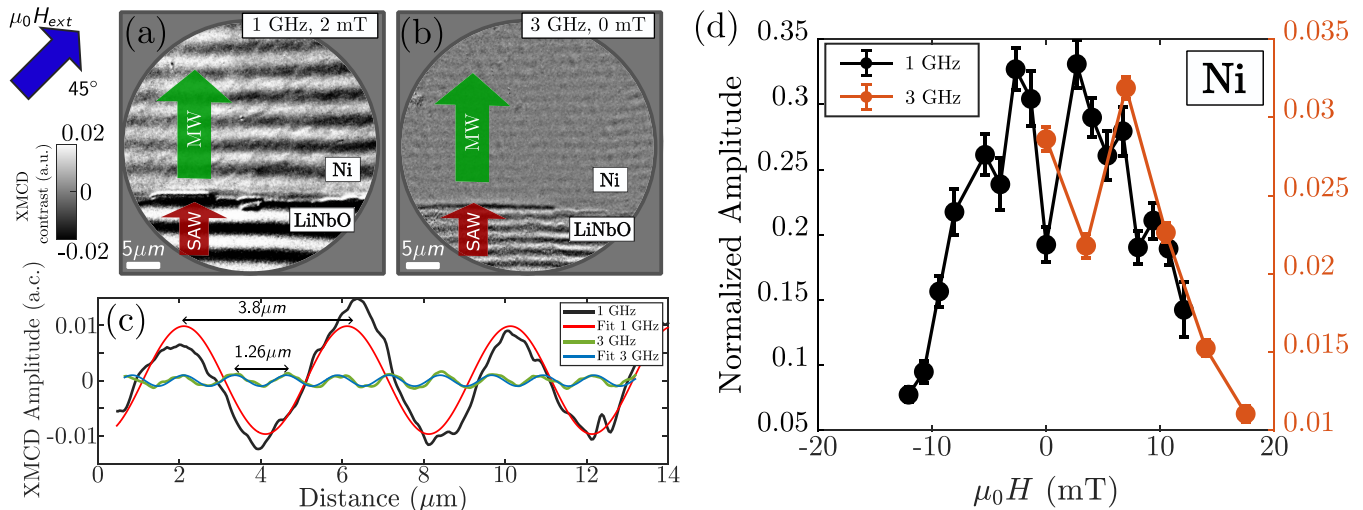


FIG. 3. (a) Two-phase XMCD image of Ni showing the MAW driven at 1 GHz. (b) Two-phase XMCD image of Ni showing the MAW driven at 3 GHz. Both color scales of (a) and (b) are equal to visually see the difference in contrast and are expressed in XMCD contrast, which is the difference in absorption between light circularly polarized to the right or to the left. (c) Experimentally determined MAW profiles at 1 GHz (black curve) and 3 GHz (green curve). The red and blue curves are fittings to a sinusoidal function. (d) Dependence of the MAW amplitude on the external magnetic field. The left axis represents the excitation at 1 GHz, while the right axis represents the excitation at 3 GHz.

in both a-FMR and XMCD experiments, with a decrease in amplitude when approaching 0 mT. Note that the amplitude of the MAWs of Co is one and two orders of magnitude lower than Ni at 3 and 1 GHz, respectively (also seen in acoustic attenuation in Fig. 2). This phenomenon could be due to the

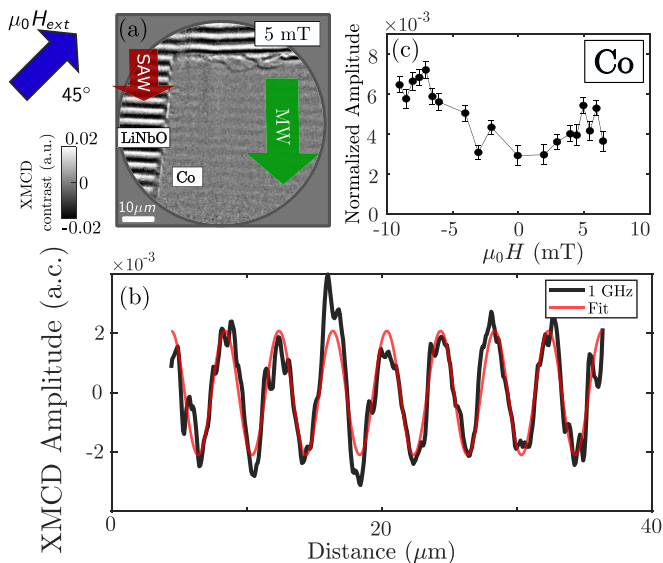


FIG. 4. (a) Two-phase XMCD image showing the piezoelectric, LiNbO₃, with visible SAWs and the ferromagnetic sample, Co, with visible MAWs at an applied magnetic field of 5 mT. The color scale represents the XMCD contrast, which is the difference in absorption between light circularly polarized to the right or to the left. (b) Experimentally determined MAW profile of the 5 mT XMCD image at 1 GHz excitation (black curve) with the corresponding sinusoidal fit (red curve). (c) MAW amplitude as a function of the applied magnetic field excited by a 1 GHz SAW.

high magnetization saturation of Co, which is three times larger than that of Ni. At 3 GHz frequency, the XMCD data of Ni display a trend with an applied magnetic field similar to that for the 1 GHz data, with a maximum of around 7 mT.

As discussed in Sec. III, we determined the strain amplitude for each frequency and sample using SAW XPEEM images on LiNbO₃ and employing the same power settings as in MAW imaging; see Table I. We observed similar relative values between the strain components for both samples at 1 GHz since identical IDTs were used on the same LiNbO₃ substrates. Notably, we also found that the strain at the sample surface measured at 3 GHz in the Ni sample was comparable and, even, slightly larger than those at 1 GHz. Therefore, the observed differences in the MAW amplitudes cannot be explained with strain values.

We performed micromagnetic simulations to evaluate the overall internal magnetic fields and determine the expected MAW amplitudes at each frequency for both materials. We used MuMax3 [41], which takes into account different magnetic contributions to the free energy, e.g., Zeeman, dipolar, exchange, and magnetoelastic to calculate an effective magnetic field. The effect of each contribution depends on the parameters of the experiment (SAW frequency and wavelength, external magnetic field, and magnetization saturation). In particular, for the ME contribution, the following free-energy expression is used:

$$F_{\text{me}} = B_1[\varepsilon_{xx}m_x^2 + \varepsilon_{yy}m_y^2 + \varepsilon_{zz}m_z^2] + 2B_2[\varepsilon_{xy}m_xm_y + \varepsilon_{xz}m_xm_z + \varepsilon_{yz}m_y m_z], \quad (1)$$

where B_1 and B_2 are the magnetoelastic constants and are taken as parameters in our simulations, m_i are the normalized magnetization components, and ε_{ij} are the strain components simulated as plane waves with the following expression:

$$\varepsilon_{ij} = e_{ij} \exp\{i(kx - \omega t)\}, \quad (2)$$

TABLE II. Sample properties used in the micromagnetic simulations. M_s is the saturation magnetization, A_{ex} the exchange, and α the Gilbert damping.

Sample	M_s (kA/m)	A_{ex} (J/m)	α
Ni	490	10^{-11}	0.03
Co	1510	10^{-11}	0.007

where e_{ij} are the strain amplitudes of Table I, k is the wave vector of the SAW traveling in the x direction, and $\omega = 2\pi f$ is the angular frequency of the SAWs. Since the SAW excited in the LiNbO₃ substrate is a Rayleigh mode, only the strain amplitudes e_{xx} , e_{zz} , and e_{xz} are nonzero in our experiment. For the magnetic anisotropy we considered the following expression for the free energy:

$$F_{anis} = -K_{u1}(\mathbf{u} \cdot \mathbf{m})^2, \quad (3)$$

where K_{u1} is the first order uniaxial anisotropy constant and \mathbf{u} is the anisotropy direction. (See Table IV.)

The simulations consist of sweeping the magnetic field gradually from 20 to 0 mT, mirroring the experimental procedure, and recording the magnetization values in time and space in the presence of SAW. The choice of larger to lower magnetic fields is made to avoid magnetic switching and the formation of magnetic domains. The simulation parameters of each material are shown in Table II. Figure 5 shows the amplitude of the MAWs determined by calculating the mean oscillating amplitude over time for each magnetic field [42].

The results for Ni with SAW at 1 GHz and 3 GHz are presented in Fig. 5(a). The black curves depict simulations at 1 GHz considering no anisotropy (continuous line) and a small in-plane anisotropy of 1 mT in the x direction. Both curves have similar amplitudes with a clear decay when increasing field. The curve without anisotropy has a large increase at zero applied field because the sample's effective field also tends to zero, which is unrealistic. Therefore, we include a small in-plane uniaxial anisotropy field to better reproduce our experiments (black and orange dots in the graph). The simulations that better adjust to the experimental data correspond to a magnetoelastic constant of $B_1 = 11 \text{ MJ/m}^3$ and a magnetic anisotropy of $K_{u1} = 1 \text{ mT}$. The orange curves correspond to the 3 GHz simulations with the same conditions of anisotropy. In this case, the simulations with a magnetoelastic constant of about $B_1 = 0.3 \text{ MJ/m}^3$ (and the same magnetic anisotropy, $K_{u1} = 1 \text{ mT}$) are the ones most accurately matching the experimental results. The magnetoelastic constant is over 30 times smaller for 3 GHz compared with 1 GHz. Simulations show that the amplitude of MAW is proportional to the magnetoelastic constant in the range of 2 – 11 MJ/m³. An additional figure showing this effect and the effect of a magnetic anisotropy can be seen in Supplemental Material [43].

Figure 5(b) illustrates the simulated curves for the MAW amplitude of the Co sample when subjected to a 1 GHz excitation. Here we plot different angles, φ_H , between the applied field and SAW propagation, ranging from 10° to 40° (from blue to green curves) to show the huge decay of the MAW amplitude with increasing the angle [as shown in SAW

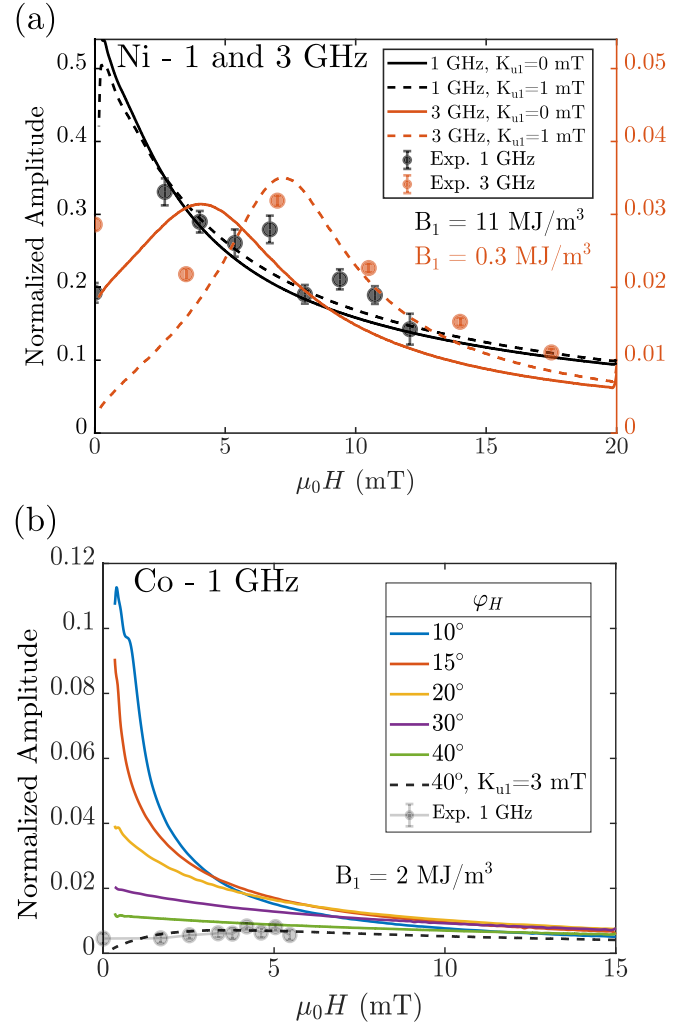


FIG. 5. Results of simulations. (a) Amplitude of MAW in Ni for excitation frequencies of 1 and 3 GHz with $\varphi_H = 45^\circ$ (solid black and orange curves, respectively). The dashed lines provide the same information including a small anisotropy, $K_{u1} = 1 \text{ mT}$. The magnetoelastic constants used for each frequency are written in the same color as the simulation curves. The faint black and orange dots are the experimental results. (b) Amplitude of the MAW in Co for an excitation frequency of 1 GHz at several φ_H , from 10° to 40°. The dashed black line represents the simulation at 40° with a small anisotropy, $K_{u1} = 3 \text{ mT}$, while the faint black dots correspond to the experimental results.

attenuation, Fig. 2(b)]. The misalignment between MAW and applied field has a more drastic impact on Co reducing the overall MAW amplitude. This occurs because the resonant frequency is shifted above the SAW frequency as $\varphi_H > 10^\circ$, resulting in no resonance. This same behavior is displayed in the a-FMR experiment (see Fig. 2). A curve for $\varphi_H = 40^\circ$ and an in-plane anisotropy of 3 mT in the x direction is added with black dashed lines, showing, as in the case of Ni, an additional decay at zero field. The value for the magnetoelastic constant that adjusts better the simulations to the experimental data (gray dots in the graph) corresponds to a $B_1 = 2 \text{ MJ/m}^3$ (see Table III).

TABLE III. Magnetoelastic constant values for each sample obtained through the simulations.

Sample	B_1 (MJ/m ³)
Ni (1 GHz)	11
Ni (3 GHz)	0.3
Co (1 GHz)	2

We now focus on the experimental results showing a drop in efficiency at 3 GHz for Ni (see Fig. 3). To account for the lower MAW amplitude, we varied the magnetoelastic constant, B_1 , until the MAW amplitude matched the experimental values. For a 1 GHz excitation, a magnetoelastic constant of $B_1 = 11$ MJ/m³ matched the experimental amplitude, while for a 3 GHz excitation, a reduced magnetoelastic constant of $B_1 = 0.3$ MJ/m³ was needed to reproduce the experimental results. This loss in magnetoelastic energy appeared unexpected to us, given that experiments are done in the same Ni layer and that physical processes involved in magnetoelasticity are expected to respond easily at the nanosecond scale. We notice that the measured strain amplitudes were obtained at the piezoelectric surface and not at the ferromagnetic film. It could be possible that the reduced magnetic response at 3 GHz is related to a lower transmission of the SAW strain to the polycrystalline thin layer under high SAW frequencies and short wavelengths. We measured AFM in our Ni films and the observed grains at the top of the film were smaller than a few tens of nanometers, a value much shorter than the SAW wavelengths used in our experiment. However, the interface between LiNbO₃ and Ni has not been characterized.

Overall, the results of our simulations agree quantitatively well with the XMCD and a-FMR experiments for both Ni and Co. At 1 GHz SAW excitation we obtained a value of B_1 for Ni of ~ 11 MJ/m³, which is slightly larger than previous experimental studies [15,28,44–46]. In Co, we obtained a magnetoelastic constant of ~ 2 MJ/m³, which is over 4–5 times smaller than the Ni one at 1 GHz (and also up to 8 times smaller if compared to the bulk value [47]). However, the simulations indicate that Co at smaller angles may achieve amplitudes approximately equal to 0.1, comparable to Ni, which could make Co an interesting material for straintronics, due to its low damping and high magnetization saturation. At 3 GHz SAW excitation, we found a reduction in the amplitude

of the MAWs in Ni that requires decreasing the magnetoelastic constant (to ~ 0.3 MJ/m³) approximately a factor of 30 compared to 1 GHz excitation. Although our model does not account for the direct transfer of the phonon angular momentum to magnetization [34,48], which might be dependent on frequency, we consider that a plausible explanation for the drop in efficiency at 3 GHz could be related to a frequency dependence of the strain transfer efficiency between LiNbO₃ and the Ni film.

V. CONCLUSIONS

We have studied the magnetoelastic effect in Ni and Co at 1 and 3 GHz using hybrid piezoelectric/ferromagnetic devices and SAWs. Our direct XPEEM-XMCD imaging shows that large amplitude MAWs in Ni and Co at frequencies of 1 and 3 GHz can be directly imaged and quantified. We found a significant difference in MAW amplitude between Ni and Co at 1 GHz excitations—a difference that cannot be explained only by the larger magnetization saturation value of Co compared with the value of Ni. Thus a lower magnetoelastic constant is obtained for Co. The found values for the magnetoelastic constants at 1 GHz are similar to those reported in the literature [15,28,44–46]. Additional measurements at 3 GHz SAW excitations show a clear decay in MAW efficiency suggesting a drop in the phonon coupling between SAW at the piezoelectric substrate and SAW at the ferromagnetic thin film. Our study provides valuable insights into the coupling between strain and magnetization dynamics at the GHz frequency and may guide the development of more efficient acoustic spintronic (straintronic) devices.

ACKNOWLEDGMENTS

The authors would like to thank N. Volkmer for their technical support in the preparation of the samples. M.W.K. acknowledges Marie Skłodowska-Curie Grant Agreement No. 754397 (DOC-FAM) from EU Horizon 2020. M.R., B.C., J.M.H., and F.M. acknowledge funding from MCIN/AEI/10.13039/501100011033 through Grant No. PID2020-113024GB-100. M.W.K., M.F., and M.A.N. acknowledge funding from MCIN through Grant No. PID2021-122980OB-C54. L.A., M.F., and S.R.G. acknowledge funding from MCIN through Grant No. RTI2018-095303. S.R.G. also acknowledges funding from Marie Skłodowska-Curie Grant No. REP-101061612-1.

- [1] N. Locatelli, V. Cros, and J. Grollier, Spin-torque building blocks, *Nat. Mater.* **13**, 11 (2014).
- [2] D. Ralph and M. Stiles, Spin transfer torques, *J. Magn. Magn. Mater.* **320**, 1190 (2008).
- [3] A. Brataas, A. D. Kent, and H. Ohno, Current-induced torques in magnetic materials, *Nat. Mater.* **11**, 372 (2012).
- [4] A. A. Bukharaev, A. K. Zvezdin, A. P. Pyatakov, and Y. K. Fetisov, Straintronics: A new trend in micro- and nanoelectronics and materials science, *Phys. Usp.* **61**, 1175 (2018).
- [5] M. Foerster and F. Macià, Preface to special issue on magneto-elastic effects, *J. Phys.: Condens. Matter* **31**, 190301 (2019).
- [6] C.-H. Lambert, S. Mangin, B. S. D. C. S. Varaprasad, Y. K. Takahashi, M. Hehn, M. Cinchetti, G. Malinowski, K. Hono, Y. Fainman, M. Aeschlimann, and E. E. Fullerton, All-optical control of ferromagnetic thin films and nanostructures, *Science* **345**, 1337 (2014).
- [7] M. Barangi and P. Mazumder, Straintronics: A leap toward ultimate energy efficiency of magnetic random access memories, *IEEE Nanotechnol. Mag.* **9**, 15 (2015).
- [8] Z. Wang, Y. Zhang, Y. Wang, Y. Li, H. Luo, J. Li, and D. Viehland, Magnetolectric assisted 180° magnetization switching for electric field addressable writing in magnetoresistive random-access memory, *ACS Nano* **8**, 7793 (2014).

- [9] H. B. Huang, J. M. Hu, T. N. Yang, X. Q. Ma, and L. Q. Chen, Strain-assisted current-induced magnetization reversal in magnetic tunnel junctions: A micromagnetic study with phase-field microelasticity, *Appl. Phys. Lett.* **105**, 122407 (2014).
- [10] J. Cenker, S. Sivakumar, K. Xie, A. Miller, P. Thijssen, Z. Liu, A. Dismukes, J. Fonseca, E. Anderson, X. Zhu, X. Roy, D. Xiao, J.-H. Chu, T. Cao, and X. Xu, Reversible strain-induced magnetic phase transition in a van der Waals magnet, *Nat. Nanotechnol.* **17**, 256 (2022).
- [11] A. K. Ganguly, K. L. Davis, D. C. Webb, and C. Vittoria, Magnetoelastic surface waves in a magnetic film–piezoelectric substrate configuration, *J. Appl. Phys.* **47**, 2696 (1976).
- [12] I.-a. Feng, M. Tachiki, C. Krischer, and M. Levy, Mechanism for the interaction of surface waves with 200-Å nickel films, *J. Appl. Phys.* **53**, 177 (1982).
- [13] W.-G. Yang and H. Schmidt, Acoustic control of magnetism toward energy-efficient applications, *Appl. Phys. Rev.* **8**, 021304 (2021).
- [14] J. Puebla, Y. Hwang, S. Maekawa, and Y. Otani, Perspectives on spintronics with surface acoustic waves, *Appl. Phys. Lett.* **120**, 220502 (2022).
- [15] B. Casals, N. Statuto, M. Foerster, A. Hernández-Mínguez, R. Cicheler, P. Manshausen, A. Mandziak, L. Aballe, J. M. Hernández, and F. Macià, Generation and imaging of magnetoacoustic waves over millimeter distances, *Phys. Rev. Lett.* **124**, 137202 (2020).
- [16] M. Weiler, L. Dreher, C. Heeg, H. Huebl, R. Gross, M. S. Brandt, and S. T. B. Goennenwein, Elastically driven ferromagnetic resonance in nickel thin films, *Phys. Rev. Lett.* **106**, 117601 (2011).
- [17] P. G. Gowtham, T. Moriyama, D. C. Ralph, and R. A. Buhrman, Traveling surface spin-wave resonance spectroscopy using surface acoustic waves, *J. Appl. Phys.* **118**, 233910 (2015).
- [18] D. Labanowski, A. Jung, and S. Salahuddin, Power absorption in acoustically driven ferromagnetic resonance, *Appl. Phys. Lett.* **108**, 022905 (2016).
- [19] K. M. Seemann, O. Gomonay, Y. Mokrousov, A. Hörner, S. Valencia, P. Klamser, F. Kronast, A. Erb, A. T. Hindmarch, A. Wixforth, C. H. Marrows, and P. Fischer, Magnetoelastic resonance as a probe for exchange springs at antiferromagnet-ferromagnet interfaces, *Phys. Rev. B* **105**, 144432 (2022).
- [20] P. Kuszewski, I. S. Camara, N. Biarrotte, L. Becerra, J. von Bardeleben, W. S. Torres, A. Lemaître, C. Gourdon, J.-Y. Duquesne, and L. Thevenard, Resonant magneto-acoustic switching: influence of rayleigh wave frequency and wavevector, *J. Phys.: Condens. Matter* **30**, 244003 (2018).
- [21] C. Müller, P. Durdaut, R. B. Holländer, A. Kittmann, V. Schell, D. Meyners, M. Höft, E. Quandt, and J. McCord, Imaging of love waves and their interaction with magnetic domain walls in magnetoelectric magnetic field sensors, *Adv. Electron. Mater.* **8**, 2200033 (2022).
- [22] M. Rovirola, M. Waqas Khaliq, B. Casals, M. Foerster, M. A. Niño, L. Aballe, J. Herfort, J. M. Hernández, F. Macià, and A. Hernández-Mínguez, Resonant and off-resonant magnetoacoustic waves in epitaxial Fe₃Si/GaAs hybrid structures, *Phys. Rev. Appl.* **20**, 034052 (2023).
- [23] M. W. Khaliq, O. Amin, A. Hernández-Mínguez, M. Rovirola, B. Casals, K. Omari, S. Ruiz-Gómez, S. Finizio, R. P. Campion, K. W. Edmonds, V. Novak, A. Mandziak, L. Aballe, M. A. Niño, J. M. Hernández, P. Wadley, F. Macià, and M. Foerster, Magneto-acoustic waves in antiferromagnetic CuMnAs excited by surface acoustic waves, [arXiv:2309.08893](https://arxiv.org/abs/2309.08893).
- [24] R. M. White and F. W. Voltmer, Direct piezoelectric coupling to surface elastic waves, *Appl. Phys. Lett.* **7**, 314 (1965).
- [25] P. Delsing, A. N. Cleland, M. J. A. Schuetz, J. Knörzer, G. Giedke, J. I. Cirac, K. Srinivasan, M. Wu, K. C. Balram, C. Bäuerle, T. Meunier, C. J. B. Ford, P. V. Santos, E. Cerda-Méndez, H. Wang, H. J. Krenner, E. D. S. Nysten, M. Weiß, G. R. Nash, L. Thevenard *et al.*, The 2019 surface acoustic waves roadmap, *J. Phys. D* **52**, 353001 (2019).
- [26] D.-L. Zhang, J. Zhu, T. Qu, D. M. Lattery, R. H. Victora, X. Wang, and J.-P. Wang, High-frequency magnetoacoustic resonance through strain-spin coupling in perpendicular magnetic multilayers, *Sci. Adv.* **6**, eabb4607 (2020).
- [27] H. Qin, R. B. Holländer, L. Flajšman, F. Hermann, R. Dreyer, G. Woltersdorf, and S. van Dijken, Nanoscale magnonic Fabry-Pérot resonator for low-loss spin-wave manipulation, *Nat. Commun.* **12**, 2293 (2021).
- [28] M. Foerster, F. Macià, N. Statuto, S. Finizio, A. Hernández-Mínguez, S. Lendínez, P. V. Santos, J. Fontcuberta, J. M. Hernández, M. Kläui, and L. Aballe, Direct imaging of delayed magneto-dynamic modes induced by surface acoustic waves, *Nat. Commun.* **8**, 407 (2017).
- [29] A. Slobodnik, Surface acoustic waves and saw materials, *Proc. IEEE* **64**, 581 (1976).
- [30] L. Aballe, M. Foerster, E. Pellegrin, J. Nicolas, and S. Ferrer, The ALBA spectroscopic LEEM-PEEM experimental station: layout and performance, *J. Synchrotron Radiat.* **22**, 745 (2015).
- [31] M. Foerster, N. Statuto, B. Casals, A. Hernández-Mínguez, R. Cicheler, P. Manshausen, A. Mandziak, L. Aballe, J. Hernández Ferràs, and F. Macià, Quantification of propagating and standing surface acoustic waves by stroboscopic x-ray photoemission electron microscopy, *J. Synchrotron Radiat.* **26**, 184 (2019).
- [32] M. W. Khaliq, J. M. Álvarez, A. Camps, N. González, J. Ferrer, A. Martínez-Carboneres, J. Prat, S. Ruiz-Gómez, M. A. Niño, F. Macià, L. Aballe, and M. Foerster, Ghz sample excitation at the ALBA-PEEM, *Ultramicroscopy* **250**, 113757 (2023).
- [33] L. Dreher, M. Weiler, M. Pernpeintner, H. Huebl, R. Gross, M. S. Brandt, and S. T. B. Goennenwein, Surface acoustic wave driven ferromagnetic resonance in nickel thin films: Theory and experiment, *Phys. Rev. B* **86**, 134415 (2012).
- [34] J. Puebla, M. Xu, B. Rana, K. Yamamoto, S. Maekawa, and Y. Otani, Acoustic ferromagnetic resonance and spin pumping induced by surface acoustic waves, *J. Phys. D* **53**, 264002 (2020).
- [35] M. Weiler, H. Huebl, F. S. Goerg, F. D. Czeschka, R. Gross, and S. T. B. Goennenwein, Spin pumping with coherent elastic waves, *Phys. Rev. Lett.* **108**, 176601 (2012).
- [36] A. Hernández-Mínguez, F. Macià, J. M. Hernández, J. Herfort, and P. V. Santos, Large nonreciprocal propagation of surface acoustic waves in epitaxial ferromagnetic/semiconductor hybrid structures, *Phys. Rev. Appl.* **13**, 044018 (2020).
- [37] M. Xu, K. Yamamoto, J. Puebla, K. Baumgaertl, B. Rana, K. Miura, H. Takahashi, D. Grundler, S. Maekawa, and Y. Otani, Nonreciprocal surface acoustic wave propagation via magneto-rotation coupling, *Sci. Adv.* **6**, eabb1724 (2020).
- [38] P. J. Shah, D. A. Bas, I. Lisenkov, A. Matyushov, N. X. Sun, and M. R. Page, Giant nonreciprocity of surface acoustic waves

- enabled by the magnetoelastic interaction, *Sci. Adv.* **6**, eabc5648 (2020).
- [39] L. Rayleigh, On waves propagated along the plane surface of an elastic solid, *Proc. London Math. Soc.* **s1-17**, 4 (1885).
- [40] B. A. Auld, Acoustic fields and waves in solids, *Acoustic Fields and Waves in Solids* (John Wiley and Sons, New York, 1973), Vol. 2.
- [41] A. Vansteenkiste, J. Leliaert, M. Dvornik, M. Helsen, F. Garcia-Sanchez, and B. Van Waeyenberge, The design and verification of MuMax3, *AIP Adv.* **4**, 107133 (2014).
- [42] See Supplemental Material at <http://link.aps.org/supplemental/10.1103/PhysRevResearch.6.023285> for the micromagnetic simulation code.
- [43] See Supplemental Material at <http://link.aps.org/supplemental/10.1103/PhysRevResearch.6.023285> for the results on the effect of B1 and Ku1 in the micromagnetic simulations.
- [44] O. Song, C. A. Ballentine, and R. C. O'Handley, Giant surface magnetostriction in polycrystalline Ni and NiFe films, *Appl. Phys. Lett.* **64**, 2593 (1994).
- [45] B. Cullity and C. Graham, *Introduction to Magnetic Materials* (John Wiley & Sons, Ltd, New York, 2008), Chap. 8, pp. 241–273.
- [46] X. Li, D. Labanowski, S. Salahuddin, and C. S. Lynch, Spin wave generation by surface acoustic waves, *J. Appl. Phys.* **122**, 043904 (2017).
- [47] R. C. O'Handley, *Modern Magnetic Materials: Principles and Applications* (John Wiley & Sons, Ltd, New York, 2000).
- [48] R. Sasaki, Y. Nii, and Y. Onose, Magnetization control by angular momentum transfer from surface acoustic wave to ferromagnetic spin moments, *Nat. Commun.* **12**, 2599 (2021).

CHAPTER 7

Chapter 7

CONCLUSIONS AND FUTURE PERSPECTIVES

In this thesis, the focus is on the observation of magnetization dynamics in the X-ray photoemission electron microscope (XPEEM) driven by surface acoustic waves (SAW) in the GHz frequency regime. We developed a new setup to ensure its compatibility with the existing PEEM setup, enabling us to excite magnetic samples at higher frequencies with minimal attenuation of electrical signals. We employed various magnetic systems to comprehend the coupling mechanism between magnetization and strain waves, utilizing simulations and models.

We studied the magnetoelastic effect in both ferromagnetic and antiferromagnetic systems by inducing surface acoustic waves (SAWs) in piezoelectric substrates. In the case of the antiferromagnetic CuMnAs, Néel vector waves were generated by exciting the SAW in the GaAs substrate at various temperatures, reaching the maximum amplitude at room temperature. However, SAWs showed no noticeable effect on the domain walls in the system. Nevertheless, this antiferromagnetic (AFM) system exhibited a significant interaction between strain and magnetization compared to ferromagnetic and Heusler systems at similar frequency signals. Furthermore, we exploited a

newly developed setup in order to reach higher frequency signals with minimum attenuation. We performed angular dependence acousto-ferromagnetic resonance measurements in Ni and Co samples, showing maximum SAW attenuation in the range of 30–45 degrees. Magnetoelastic coupling in ferromagnetic samples of Ni and Co, deposited on LiNbO₃ substrates, was studied at higher frequencies, revealing strong coupling of strain waves and magnetization as magnetoacoustic waves (MAWs) in the Ni film at 1 GHz, which substantially weakened at 3 GHz. In Co, the amplitude of the MAWs was found to be weaker than in Ni at 1 GHz due to the higher saturation magnetization in the Co film. Simulations were performed to estimate the values of magnetoelastic coupling, with Ni at 1 GHz exhibiting the maximum coupling.

In conclusion, we explored an alternative and novel approach to generate propagating waves in magnetic thin films and observing them at sub-nanosecond timescales. These waves result from the coupling of strain components in the lattice with magnetization/Néel vector, extending up to distances of millimeters with low energy consumption compared to other methods of inducing dynamics in materials. However, the amplitude of the excited waves (MAWs) weakens at higher frequencies, a phenomenon that warrants further exploration. Therefore, this work provides insight into devices where MAWs could serve as an alternative for storing carrier signals. Consequently, this thesis holds great interest from both fundamental and potentially technological perspectives.

For future perspectives, an open question persists if the SAW can induce domain wall motions in AFM system. Since the magnetization dynamics have been induced and magnetization waves have been excited in ferromagnetic system, we expect to induce dynamics in magnetic nanostructures as well in AFM by SAW. This could be attained by preparing new samples with minimum defects in the system, and exciting the samples with higher frequency signals by employing newly developed setup. We observed MAWs in different ferromagnetic systems at higher frequencies but with different amplitudes at a specific frequency. This has been surprising since the same substrates have been used for both systems, implying that the magnetization interacts with the

strain waves differently. Furthermore, the amplitude of the MAWs weakens with higher frequency, therefore, needs to be assessed the limit up to which it persists the higher amplitude. Moreover, the new setup provides excellent conditions for time resolved XPEEM measurements, in magnetization dynamics, as well as domain wall and skyrmions motion by applying ultra-short current pulses. Such systems can further be explored in future that can allow us to explore the possibilities of creating new nanomagnetic devices for data storage applications in future.

BIBLIOGRAPHY

- [1] S. Blundell. (2001). *Magnetism in Condensed Matter*, Oxford University Press.
- [2] A. A. Timopheev, R. Sousa, M. Chshiev, H. T. Nguyen, and B. Dieny, Second order anisotropy contribution in perpendicular magnetic tunnel junctions, *Scientific Reports* **6** (2016) 26877. <https://doi.org/10.1038/srep26877>.
- [3] F. Bloch, Zur Theorie des Austauschproblems und der Remanenzerscheinung der Ferromagnetika, *Zeitschrift für Physik* **74** (1932) 295–335. <https://doi.org/10.1007/BF01337791>.
- [4] B. Heinrich and J. F. Cochran, Ultrathin metallic magnetic films: magnetic anisotropies and exchange interactions, *Advances in Physics* **42** (5) (1993) 523–639. <https://doi.org/10.1080/00018739300101524>.
- [5] J. H. E. Griffiths, Anomalous high-frequency resistance of ferromagnetic metals, *Nature* **158** (4019) (1946) 670–671. <https://doi.org/10.1038/158670a0>.
- [6] S. S. Kalarickal, P. Krivosik, M. Wu, C. E. Patton, M. L. Schneider, P. Kabos, T. J. Silva, and J. P. Nibarger, Ferromagnetic resonance linewidth in metallic thin films: Comparison of measurement methods, *Journal of Applied Physics* **99** (2006) 093909. <https://doi.org/10.1063/1.2197087>.
- [7] J. Joule, On a new class of magnetic forces, *Annals of Electricity, Magnetism, and Chemistry* **8** (1842) 219–224.

-
- [8] E. Villari, Change of magnetization by tension and by electric current, *Annual Review of Physical Chemistry* **126** (1865) 87–122. <https://doi.org/10.1002/andp.18652020906>.
- [9] B. D. Cullity and C. D. Graham. (2008). Magnetostriction and the Effects of Stress. In: Introduction to Magnetic Materials. John Wiley & Sons, Ltd. <https://doi.org/10.1002/9780470386323>.
- [10] S. Finizio, S. Wintz, S. Gliga, E. Kirk, A. K. Suszka, P. Wohlhüter, K. Zeissler, and J. Raabe, Unexpected field-induced dynamics in magnetostrictive microstructured elements under isotropic strain, *Journal of Physics: Condensed Matter* **30** (31) (2018) 314001. <https://doi.org/10.1088/1361-648X/aacddd>.
- [11] R. C. O'Handley. (2000). Modern Magnetic Materials: Principles and Applications. John Wiley & Sons, Inc., New York.
- [12] F. Vanderveken, F. Ciubotaru, and C. Adelman, (2021). Magnetoelastic Waves in Thin Films. In: E. Kamenetskii, (eds) Chirality, Magnetism and Magnetoelectricity. Topics in Applied Physics, **138**. Springer, Cham. https://doi.org/10.1007/978-3-030-62844-4_12.
- [13] M. Foerster, F. Macià, N. Statuto, S. Finizio, A. Hernández-Mínguez, S. Lendínez, P. V. Santos, J. Fontcuberta, J. M. Hernández, M. Kläui, and L. Aballe, Direct imaging of delayed magneto-dynamic modes induced by surface acoustic waves, *Nature Communications* **8** (2017) e407. <https://doi.org/10.1038/s41467-017-00456-0>.
- [14] M. Rovirola, M. W. Khaliq, B. Casals, M. Foerster, M. A. Niño, L. Aballe, J. Herfort, J. M. Hernández, F. Macià, and A. Hernández-Mínguez, Resonant and Off-Resonant Magnetoacoustic Waves in Epitaxial Fe₃Si/GaAs Hybrid Structures, *Physical Review Applied* **20** (2023) 034052. <https://doi.org/10.1103/PhysRevApplied.20.034052>.
- [15] H. Ahmad, J. Atulasimha, and S. Bandyopadhyay, Reversible strain-induced magnetization switching in FeGa nanomagnets: pathway to a rewritable, non-volatile, non-toggle, extremely low energy straintronic memory, *Scientific Reports* **5** (2015) 18264. <https://doi.org/10.1038/srep18264>.

-
- [16] L. Fecova, K. Richter, and R. Varga, Manipulation of individual domain walls by axial rotation in transverse magnetic field, *Journal of Magnetism and Magnetic Materials* **538** (2021) 168274. <https://doi.org/10.1016/j.jmmm.2021.168274>.
- [17] I. M. Miron, T. Moore, H. Szambolics, L. D. Buda-Prejbeanu, S. Auffret, B. Rodmacq, S. Pizzini, J. Vogel, M. Bonfim, A. Schuhl and G. Gaudin, Fast current-induced domain-wall motion controlled by the Rashba effect, *Nature Materials* **10** (2011) 419–423. <https://doi.org/10.1038/nmat3020>.
- [18] M. Hayashi, L. Thomas, R. Moriya, C. Rettner, and S. S. P. Parkin, Current-Controlled Magnetic Domain-Wall Nanowire Shift Register, *Science* **320** (2008) 209–211. <https://doi.org/10.1126/science.1154587>.
- [19] D. Chiba, G. Yamada, T. Koyama, K. Ueda, H. Tanigawa, S. Fukami, T. Suzuki, N. Ohshima, N. Ishiwata, Y. Nakatani and T. Ono, Control of Multiple Magnetic Domain Walls by Current in a Co/Ni Nano-Wire, *Appl. Phys. Express* **3** (2010) 073004. <https://doi.org/10.1143/APEX.3.073004>.
- [20] J. Chen and S. Dong, Manipulation of Magnetic Domain Walls by Ferroelectric Switching: Dynamic Magnetoelectricity at the Nanoscale, *Physical Review Letters* **126** (2021) 117603. <https://doi.org/10.1103/PhysRevLett.126.117603>.
- [21] D. Chiba, M. Kawaguchi, S. Fukami, N. Ishiwata, K. Shimamura, K. Kobayashi and T. Ono, Electric-field control of magnetic domain-wall velocity in ultrathin cobalt with perpendicular magnetization, *Nature Communications* **3** (2012) 888. <https://doi.org/10.1038/ncomms1888>.
- [22] U. Parlak, R. Adam, D. E. Bürgler, T. Duchoň, S. Nemšák, F. Wang, C. Greb, S. Heitfeld, and C. M. Schneider, Ferromagnetic domain wall manipulation using optically induced thermal gradients, *Journal of Magnetism and Magnetic Materials* **560** (2022) 169441. <https://doi.org/10.1016/j.jmmm.2022.169441>.
- [23] J-Y. Duquesne, C. Hepburn, P. Rovillain, M. Marangolo, Magnetocrystalline and magnetoelastic constants determined by magnetization dynamics

-
- under static strain, *Journal of Physics: Condensed Matter* **30** (39) (2018) 394002. <https://doi.org/10.1088/1361-648X/aadc2f>.
- [24] P. Willmott. (2011). An Introduction to Synchrotron Radiation: Techniques and Applications. <https://doi.10.1002/9781119970958.Ch.1>.
- [25] S. Lewis, J. Gelb, S. H. Lau, W. Yun, D. Vine, B. Stripe and S. Seshadri, Recent Developments in Laboratory X-ray Microanalytical Techniques for Electronic Structure, Chemical Composition, and Microstructure of Metals and Materials, *Microscopy and Microanalysis* **26** (2020) 516 (Suppl 2) <https://doi.org/10.1017/S1431927620014919>.
- [26] J.-E. Rubensson. (2016). Synchrotron radiation: an everyday application of special relativity (Ch. 1). Morgan & Claypool, Britain. <https://doi.org/10.1088/978-1-6817-4115-4>.
- [27] A. Balerna and S. Mobilio. (2015). Introduction to Synchrotron Radiation, In: S. Mobilio, F. Boscherini, and C. Meneghini (eds) Synchrotron Radiation. Springer, Berlin, Heidelberg. https://doi.org/10.1007/978-3-642-55315-8_1.
- [28] P. Willmott. (2011). An Introduction to Synchrotron Radiation: Techniques and Applications. <https://doi.10.1002/9781119970958.Ch.3>.
- [29] S. Hüfner (2003). Photoelectron Spectroscopy: Principles and Applications. Advanced Texts in Physics. Springer, Berlin.
- [30] S. Anders, H. A. Padmore, R. M. Duarte, T. Renner, T. Stammer, A. Scholl, M. R. Scheinfein, J. Stöhr, L. Seve, and B. Sinkovic, Photoemission electron microscope for the study of magnetic materials, *Review of Scientific Instruments* **70** (1999) 3973–3981. <https://doi.org/10.1063/1.1150023>.
- [31] M. J. Prieto and T. Schmidt, LEEM and PEEM as Probing Tools to Address Questions in Catalysis, *Catalysis Letters* **147** (2017) 2487–2497. <https://doi.org/10.1007/s10562-017-2162-x>.
- [32] E. Bauer, A brief history of PEEM, *Journal of Electron Spectroscopy and Related Phenomena* **185**(10) (2012) 314–322. <https://doi.org/10.1016/j.elspec.2012.08.001>.

-
- [33] E. Bauer, Low energy electron microscopy, *Reports on Progress in Physics* **57**(9) (1994) 895. <https://doi.org/10.1088/0034-4885/57/9/002>.
- [34] E. Bauer, LEEM Basics, *Surface Review and Letters* **5**(6) (1998) 1275–1286. <https://doi.org/10.1142/S0218625X98001614>.
- [35] J. de la Figuera and K. F. McCarty. (2013). Low-Energy Electron Microscopy, In: G. Bracco, B. Holst (eds) *Surface Science Techniques*. Springer Berlin, Heidelberg. <https://doi.org/10.1007/978-3-642-34243-1>.
- [36] T. Schmidt, A. Sala, H. Marchetto, E. Umbach, H. -J. Freund, First experimental proof for aberration correction in XPEEM: Resolution, transmission enhancement, and limitation by space charge effects, *Ultramicroscopy* **126** (2013) 23–32. <https://doi.org/10.1016/j.ultramic.2012.11.004>.
- [37] E. Bauer, Surface electron microscopy: the first thirty years, *Surface Science* **299–300** (1994) 102–115. [https://doi.org/10.1016/0039-6028\(94\)90649-1](https://doi.org/10.1016/0039-6028(94)90649-1).
- [38] Th. Schmidt, S. Heun, J. Slezak, J. Diaz, K. C. Prince, G. Lilienkamp, and E. Bauer, SPELEEM: Combining LEEM and Spectroscopic Imaging, *Surface Review and Letters* **5**(6) (1998) 1287–1296. <https://doi.org/10.1142/S0218625X98001626>.
- [39] B. P. Tonner and D. Dunham, Sub-micron spatial resolution of a micro-XAFS electrostatic microscope with bending magnet radiation: Performance assessments and prospects for aberration correction, *Nuclear Instruments and Methods in Physics Research Section A: Accelerators, Spectrometers, Detectors and Associated Equipment* **347** (1994) 436–440. [https://doi.org/10.1016/0168-9002\(94\)91923-2](https://doi.org/10.1016/0168-9002(94)91923-2).
- [40] F. Nolting. (2010). Magnetic Imaging with X-rays. In: E. Beaurepaire, H. Bulou, F. Scheurer, K. Jean-Paul, (eds) *Magnetism and Synchrotron Radiation*. Springer Proceedings in Physics, **vol 133**. Springer, Berlin, Heidelberg. https://doi.org/10.1007/978-3-642-04498-4_12.

-
- [41] A. Locatelli, T. O. Montes, M. Á. Niño, and E. Bauer, Image blur and energy broadening effects in XPEEM, *Ultramicroscopy* **111** (2011) 1447–1454. <https://doi.org/10.1016/j.ultramic.2010.12.020>.
- [42] T. Schmidt, U. Groh, R. Fink, E. Umbach, O. Schaff, W. Engel, B. Richter, H. Kuhlenbeck, R. Schlogl, H. -J. Freund, A.M. Bradshaw, D. Preikszas, P. Hartel, R. Spehr, H. Rose, G. Lilienkamp, E. Bauer, G. Benner, XPEEM with energy-filtering: advantages and first results from the SMART project, *Surface Review and Letters* **09**(01) (2002) 223–232. <https://doi.org/10.1142/S0218625X02001811>.
- [43] T. O. Montes and A. Locatelli, Angle-Resolved X-Ray Photoemission Electron Microscopy, *Journal of Electron Spectroscopy and Related Phenomena* **185**(10) (2012) 323–329. <https://doi.org/10.1016/j.elspec.2012.07.007>.
- [44] B. P. Tonner and G. R. Harp, Photoelectron microscopy with synchrotron radiation, *Review of Scientific Instruments* **59**(6) (1988) 853–858. <http://doi.org/10.1063/1.1139792>.
- [45] P. Carra, B. T. Thole, M. Altarelli, and X. Wang, X-ray circular dichroism and local magnetic field, *Physical Review Letters* **70** (1993) 694. <http://doi.org/10.1103/PhysRevLett.70.694>.
- [46] G. van der Laan and T. Hesjedal, X-ray detected ferromagnetic resonance techniques for the study of magnetization dynamics, *Nuclear Instruments and Methods in Physics Research B* **540** (2023) 85–93. <https://doi.org/10.1016/j.nimb.2023.04.005>.
- [47] H. Ramanantoanina, M. Studniarek, N. Daffé, and J Dreiser, Non-empirical calculation of X-ray magnetic circular dichroism in lanthanide compounds, *Chemical Communications* **55** (2019) 2988. <https://doi.org/10.1039/c8cc09321k>.
- [48] G. Aquilanti, L. Vaccari, J. R. Plaisier and A.a Goldoni. (2015) Instrumentation at Synchrotron Radiation Beamlines, In: S. Mobilio, F. Boscherini, C. Meneghini (eds) Synchrotron Radiation. Springer Berlin, Heidelberg. https://doi.org/10.1007/978-3-642-55315-8_3.
- [49] <https://www.cells.es/>

-
- [50] L. Aballe, M. Foerster, E. Pellegrin, J. Nicolas, and S. Ferrer, The ALBA spectroscopic LEEM-PEEM experimental station: layout and performance, *Journal of Synchrotron Radiation* **22**(3) (2015) 745–752. <https://doi.org/10.1107/S1600577515003537>.
- [51] P. Kirkpatrick and A. V. Baez, Formation of optical images by X-rays, *Journal of the Optical Society of America* **38**(9) (1948) 766–774. <https://doi.org/10.1364/josa.38.000766>.
- [52] M. W. Khaliq, J. M. Álvarez, A. Camps, N. González, J. Ferrer, A. Martínez-Carboneres, J. Prat, S. Ruiz-Gómez, M. A. Niño, F. Macià, L. Aballe, M. Foerster, GHz sample excitation at the ALBA-PEEM, *Ultramicroscopy* **250** (2023) 113757. <https://doi.org/10.1016/j.ultramic.2023.113757>.
- [53] <https://www.3ds.com/products-services/simulia/products/opera/>.
- [54] B. Dieny, I. L. Prejbeanu, K. Garello, P. Gambardella, P. Freitas, R. Lehndorff, W. Raberg, U. Ebels, S. O. Demokritov, J. Akerman, A. Deac, P. Pirro, C. Adelman, A. Anane, A. V. Chumak, A. Hirohata, S. Mangin, Sergio O. Valenzuela, M. Cengiz Onbaşlı, M. d'Aquino, G. Prenat, G. Finocchio, L. Lopez-Diaz, R. Chantrell, O. Chubykalo-Fesenko & P. Bortolotti, Opportunities and Challenges for Spintronics in the Microelectronics Industry, *Nature Electronics* **3**(8) (2020) 446–459. <https://doi.org/10.1038/s41928-020-0461-5>.
- [55] E. Y. Vedmedenko, R. K. Kawakami, D. D. Sheka, P. Gambardella, A. Kirilyuk, A. Hirohata, C. Binck, O. Chubykalo-Fesenko, S. Sanvito, B. J. Kirby, J. Grollier, K. Everschor-Sitte, T. Kampfrath, C-Y. You and A. Berger, The 2020 Magnetism Roadmap, *Journal of Physics D: Applied Physics* **53**(2017) 453001. <https://doi.org/10.1088/1361-6463/ab9d98>.
- [56] D.C. Ralph and M.D. Stiles, Spin transfer torques, *Journal of Magnetism and Magnetic Materials* **320** (2008) 1190–1216. <https://doi.org/10.1016/j.jmmm.2007.12.019>.
- [57] A. Brataas, A.D. Kent, and H. Ohno, Current-induced torques in magnetic materials, *Nature Materials* **11** (2012) 372–381. <https://doi.org/10.1038/nmat3311>.

-
- [58] I. M. Miron, K. Garello, G. Gaudin, Pierre-J. Zermatten, M. V. Costache, S. Auffret, S. Bandiera, B. Rodmacq, A. Schuhl and P. Gambardella, Perpendicular switching of a single ferromagnetic layer induced by in-plane current injection, *Nature* **476** (2011) 189–193. <https://doi.org/10.1038/nature10309>.
- [59] A. Manchon, H.C. Koo, J. Nitta, S.M. Frolov, and R.A. Duine, New Perspectives for Rashba Spin-Orbit Coupling, *Nature Materials* **14** (9) (2015) 871–882. <https://doi.org/10.1038/nmat4360>.
- [60] S. Ruiz-Gómez, R. Guerrero, M. W. Khaliq, C. Fernández-González, Jordi Prat, A. Valera, S. Finizio, P. Perna, J. Camarero, Lucas Perez, L. Aballe, and M. Foerster, Direct X-ray detection of Spin Hall Effect in CuBi, *Physical Review X* **12** (2022) 031032. <https://doi.org/10.1103/PhysRevX.12.031032>.
- [61] K. Garello, F. Yasin, and G.S. Kar, IEEE, Spin-orbit torque MRAM for ultrafast embedded memories: from fundamentals to large scale technology integration, in: IEEE 11th International Memory Workshop (IMW), Monterey, CA (2019) 101–104. <https://doi.org/sire.ub.edu/10.1109/IMW.2019.8739466>.
- [62] X. Wang, C. Wan, W. Kong, X. Zhang, Y. Xing, C. Fang, B. Tao, W. Yang, L.i. Huang, H. Wu, M. Irfan, and X. Han, Field-free programmable spin logics via chirality-reversible spin-orbit torque switching, *Advanced Materials* **30** (2018) 1801318. <https://doi.org/10.1002/adma.201801318>.
- [63] T. Chen, R.K. Dumas, A. Eklund, P.K. Muduli, A. Houshang, A.A. Awad, P. Durrenfeld, B.G. Malm, A. Rusu, and J. Akerman, Spin-torque and spin-Hall nano-oscillators, *Proceedings IEEE* **104** (2016) 1919–1945. <https://doi.org/10.1109/JPROC.2016.2554518>.
- [64] J. Ho, F. C. Khanna, and B. C. Choi, Radiation-spin interaction, Gilbert damping, and spin torque, *Physical Review Letters* **92**(9) (2004) 097601. <https://doi.org/10.1103/PhysRevLett.92.097601>.
- [65] Y. Xu and S. Mangin, Magnetization manipulation using ultra-short light pulses, *Journal of Magnetism and Magnetic Materials* **564** (2022) 170169. <https://doi.org/10.1016/j.jmmm.2022.170169>.

-
- [66] C.-H. Lambert, S. Mangin, B. S. D. C. S. Varaprasad, Y. K. Takahashi, M. Hehn, M. Cinchetti, G. Malinowski, K. Hono, Y. Fainman, M. Aeschlimann, and E. E. Fullerton, All-optical control of ferromagnetic thin films and nanostructures, *Science* **345** (2014) 1337. <https://doi.org/10.1126/science.1253493>.
- [67] I. V. Savochkin, M. Jäckl, V. I. Belotelov, I. A. Akimov, M. A. Kozhaev, D. A. Sylgacheva, A. I. Chernov, A. N. Shaposhnikov, A. R. Prokopov, V. N. Berzhansky, D. R. Yakovlev, A.K. Zvezdin, and M. Bayer, Generation of spin waves by a train of fs-laser pulses: a novel approach for tuning magnon wavelength, *Scientific Reports* **7** (2017) 5668. <https://doi.org/10.1038/s41598-017-05742-x>.
- [68] F. Matsukura, Y. Tokura, and H. Ohno, Control of magnetism by electric fields, *Nature Nanotechnology* **10** (2015) 209–220. <https://doi.org/10.1038/nnano.2015.22>.
- [69] H. Ohno, D. Chiba, F. Matsukura, T. Omiya, E. Abe, T. Dietl, Y. Ohno, and K. Ohtani, Electric-field control of ferromagnetism, *Nature* **408** (2000) 944–946. <https://doi.org/10.1038/35050040>.
- [70] D. Chiba, M. Yamanouchi, F. Matsukura, and H. Ohno, Electrical manipulation of magnetization reversal in a ferromagnetic semiconductor, *Science* **301** (2003) 943–945. <https://doi.org/10.1126/science.1086608>.
- [71] W. Eerenstein, N. D. Mathur, and J. F. Scott, Multiferroic and magnetoelectric materials, *Nature* **442** (2006) 759–765. <https://doi.org/10.1038/nature05023>.
- [72] J. Okabayashi, Y. Miura and T. Taniyama, Strain-induced reversible manipulation of orbital magnetic moments in Ni/Cu multilayers on ferroelectric BaTiO₃, *npj Quantum Materials* **4** (2019) 21. <https://doi.org/10.1038/s41535-019-0159-y>.
- [73] A. Bur, T. Wu, J. Hockel, C.-Jui Hsu, H. K. D. Kim, T.-Kan Chung, K. Wong, K. L. Wang, and G. P. Carman, Strain-induced magnetization change in patterned ferromagnetic nickel nanostructures, *Journal of Applied Physics* **109** (2011) 123903. <https://doi.org/10.1063/1.3592344>.

-
- [74] X. Chen, X. Zhou, R. Cheng, C. Song, J. Zhang, Y. Wu, Y. Ba, H. Li, Y. Sun, Y. You, Y. Zhao, and F. Pan, Electric field control of Néel spin-orbit torque in an antiferromagnet, *Nature Materials* **18** (2019) 931–935. <https://doi.org/10.1038/s41563-019-0424-2>.
- [75] V. Grigorev, M. Filianina, Y. Lytvynenko, S. Sobolev, A. R. Pokharel, A. Sapozhnik, A. Kleibert, S. Yu. Bodnar, P. Grigorev, Y. Skourski, M. Kläui, H.-Joachim Elmers, M. Jourdan, and J. Demsar, Optically Triggered Néel Vector Manipulation of a Metallic Antiferromagnet Mn₂Au under Strain, *ACS Nano* **16** (12) (2022) 20589–20597. <https://doi.org/10.1021/acsnano.2c07453>.
- [76] Y. Niimi, Y. Kawanishi, D. H. Wei, C. Deranlot, H. X. Yang, M. Chshiev, T. Valet, A. Fert, and Y. Otani, Giant Spin Hall Effect Induced by Skew Scattering from Bismuth Impurities inside Thin Film CuBi Alloys, *Physical Review Letters* **109** (2012) 156602. <https://doi.org/10.1103/PhysRevLett.109.156602>.
- [77] C. Stamm, C. Murer, M. Berritta, J. Feng, M. Gabureac, P. M. Oppeneer, and P. Gambardella, Magneto-Optical Detection of the Spin Hall Effect in Pt and W Thin Films, *Physical Review Letters* **119** (2017) 087203. <https://doi.org/10.1103/PhysRevLett.119.087203>.
- [78] L. Álvaro-Gómez, S. Ruiz-Gómez, C. Fernández-González, M. Schöbitz, N. Mille, J. Hurst, D. Tiwari, A. De Riz, I. M. Andersen, J. Bachmann, L. Cagnon, M. Foerster, L. Aballe, R. Belkhou, J.-C. Toussaint, C. Thirion, A. Masseboeuf, D. Gusakova, L. Pérez, and O. Fruchart, Micromagnetics of magnetic chemical modulations in soft-magnetic cylindrical nanowires, *Physical Review B* **106** (2022) 054433. <https://doi.org/10.1103/PhysRevB.106.054433>.
- [79] M. F. Lewis. (1985). On Rayleigh waves and related propagating acoustic waves, In: Rayleigh-Wave Theory and Application, E. A. Ash et al. (eds) Springer-Verlag Berlin Heidelberg. https://doi.org/10.1007/978-3-642-82621-4_4.
- [80] B. von Boehn, M. Foerster, M. von Boehn, J. Prat, F. Macià, B. Casals, M. W. Khaliq, A. Hernández-Mínguez, L. Aballe, and R. Imbihl, On the Promotion

-
- of Catalytic Reactions by Surface Acoustic Waves, *Angewandte Chemie-International Edition* **59**(45) (2020) 20224–20229.
<https://doi.org/10.1002/anie.202005883>.
- [81] L. Rayleigh, On waves propagated along the plane surface of an elastic solid, *Proceedings of the London Mathematical Society* **1** (1885) 4–11.
<https://doi.org/10.1112/plms/s1-17.1.4>
- [82] R. M. White and F. W. Voltmer, Direct piezoelectric coupling to surface elastic waves, *Applied Physics Letters* **7** (1965) 314–316.
<https://doi.org/10.1063/1.1754276>
- [83] I. D. Avramov, A. Voigt, and M. Rapp, Rayleigh SAW resonators using gold electrode structure for gas sensor applications in chemically reactive environments, *Electronics Letters* **41** (2005) 450–452.
<https://doi.org/10.1049/el:20050432>.
- [84] F. Martin, M. I. Newton, G. McHale, K. A. Melzak, and E. Gizeli, Pulse mode shear horizontal-surface acoustic wave (SH-SAW) system for liquid-based sensing applications, *Biosensors and Bioelectronics* **19** (2004) 627–632.
[https://doi.org/10.1016/S0956-5663\(03\)00257-4](https://doi.org/10.1016/S0956-5663(03)00257-4).
- [85] C. M. Lin, T. T. Yen, Y. J. Lai, V. V. Felmetzger, M. A. Hopcroft, J. H. Kuypers, and A. P. Pisano, Temperature-compensated aluminum nitride lamb wave resonators, *IEEE Transactions on Ultrasonics, Ferroelectrics, and Frequency Control* **57**(3) (2010) 524–532.
<https://doi.org/10.1109/TUFFC.2010.1443>.
- [86] Y. Lei and H. Hu, SAW-driven droplet jetting technology in microfluidic: A review, *Biomicrofluidics* **14** (2020) 061505.
<https://doi.org/10.1063/5.0014768>.
- [87] J. Zhou, Y. H. Liu, Z. J. Zhan, F. L. Zhuo, Z. B. Ji, Y. J. Zheng, Y. Q. Fu, and H. G. Duan, Strategies for Giant Mass Sensitivity Using Super-High-Frequency Acoustic Waves, *IEEE Sensors Journal* **22** (2022) 20336–20345.
<https://doi.org/10.1109/JSEN.2022.3208242>.
- [88] K.-ya Hashimoto. (2000). *Surface Acoustic Wave Devices in Telecommunications*. Springer Berlin, Heidelberg, Germany.
<https://doi.org/10.1007/978-3-662-04223-6>.

-
- [89] Y. Q. Fu, J. Luo, N.-T. Nguyen, A. Walton, A. J. Flewitt, X.-T. Zu, Y. Li, G. McHale, A. Matthews, and E. Iborra, Advances in piezoelectric thin films for acoustic biosensors, acoustofluidics and lab-on-chip applications, *Progress in Materials Science* **89** (2017) 31–91. <https://doi.org/10.1016/j.pmatsci.2017.04.006>.
- [90] D. Mandal and S. Banerjee, Surface Acoustic Wave (SAW) Sensors: Physics, Materials, and Applications, *Sensors* **22**(3) (2022) 820. <https://doi.org/10.3390/s22030820>.
- [91] P. Kuszewski, J.-Y. Duquesne, L. Becerra, A. Lemaître, S. Vincent, S. Majrab, F. Margailan, C. Gourdon, and L. Thevenard, Optical probing of rayleigh wave driven magnetoacoustic resonance, *Physical Review Applied* **10** (2018) 034036. <https://doi.org/10.1103/PhysRevApplied.10.034036>.
- [92] M. Foerster, L. Aballe, J. M. Hernández, and F. Macià, Subnanosecond magnetization dynamics driven by strain waves, *MRS Bulletin* **43** (2018) 854–859. <https://doi.org/10.1557/mrs.2018.258>.
- [93] I. Bertelli, J. J. Carmiggelt, T. Yu, B. G. Simon, C. C. Pothoven, G. E. W. Bauer, Y. M. Blanter, J. Aarts, and T. van der Sar, Magnetic resonance imaging of spin-wave transport and interference in a magnetic insulator, *Science Advances* **6** (46) (2020) eabd3556. <https://doi.org/10.1126/sciadv.abd3556>.
- [94] B. Casals, N. Statuto, M. Foerster, A. Hernández-Mínguez, R. Cichelero, P. Manshausen, A. Mandziak, L. Aballe, J. Manel Hernández, and F. Macià, Generation and Imaging of Magnetoacoustic Waves over Millimeter Distances, *Physical Review Letters* **124** (2020) 137202. <https://doi.org/10.1103/PhysRevLett.124.137202>.
- [95] M. Kramia, P. Kuszewski, J.-Y. Duquesne, A. Lemaître, F. Margailan, C. Gourdon, and L. Thevenard, Time- and space-resolved nonlinear magnetoacoustic dynamics, *Physical Review B* **101** (2020) 144425. <https://doi.org/10.1103/PhysRevB.101.144425>.
- [96] D. Labanowski, V. P. Bhallamudi, Q. Guo, C. M. Purser, B. A. McCullian, P. C. Hammel, and S. Salahuddin, Voltage-driven, local, and efficient excitation

-
- of nitrogen-vacancy centers in diamond, *Science Advances* **4** (2018) eaat6574. <https://doi.org/10.1126/sciadv.aat6574>.
- [97] J. M. Hernández, P. V. Santos, F. Macià, A. García-Santiago, and J. Tejada, Acoustomagnetic pulse experiments in LiNbO₃/Mn₁₂ hybrids, *Applied Physics Letters* **88** (2006) 012503. <https://doi.org/10.1063/1.2158705>.
- [98] S. Davis, A. Baruth, and S. Adenwalla, Magnetization dynamics triggered by surface acoustic waves, *Applied Physics Letters* **97** (2010) 232507. <https://doi.org/10.1063/1.3521289>.
- [99] M. Weiler, L. Dreher, C. Heeg, H. Huebl, R. Gross, M. S. Brandt, and S. T. B. Goennenwein, Elastically Driven Ferromagnetic Resonance in Nickel Thin Films, *Physical Review Letters* **106** (2011) 117601. <https://doi.org/10.1103/PhysRevLett.106.117601>.
- [100] M. Weiler, H. Huebl, F. S. Goerg, F. D. Czeschka, R. Gross, and S. T. B. Goennenwein, Spin pumping with coherent elastic waves, *Physical Review Letters* **108** (2012) 176601. <https://doi.org/10.1103/PhysRevLett.108.176601>.
- [101] P. G. Gowtham, T. Moriyama, D. C. Ralph, and R. A. Buhrman, Traveling surface spin-wave resonance spectroscopy using surface acoustic waves, *Journal of Applied Physics* **118** (2015) 233910. <https://doi.org/10.1063/1.4938390>.
- [102] D. Labanowski, A. Jung, and S. Salahuddin, Power absorption in acoustically driven ferromagnetic resonance *Applied Physics Letters* **108** (2016) 022905. <https://doi.org/10.1063/1.4939914>.
- [103] L. Thevenard, I. S. Camara, S. Majrab, M. Bernard, P. Rovillain, A. Lemaître, C. Gourdon, and J.-Y. Duquesne, Precessional magnetization switching by a surface acoustic wave, *Physical Review B* **93** (2016) 134430. <https://doi.org/10.1103/PhysRevB.93.134430>.
- [104] P. Kuszewski, I. S. Camara, N. Biarrotte, L. Becerra, J. von Bardeleben, W. S. Torres, A. Lemaître, C. Gourdon, J.-Y. Duquesne, and L. Thevenard, Resonant magneto-acoustic switching: influence of Rayleigh wave frequency and wavevector, *Journal of Physics: Condensed Matter* **30** (2018) 244003. <https://doi.org/10.1088/1361-648X/aac152>.

-
- [105] M. Foerster and F. Macià, Preface to Special Issue on Magneto-Elastic Effects, *Journal of Physics: Condensed Matter* **31** (2019) 190301. <https://doi.org/10.1088/1361-648X/ab067c>.
- [106] J. Puebla, Y. Hwang, S. Maekawa, and Y. Otani, Perspectives on spintronics with surface acoustic waves, *Applied Physics Letters* **120** (2022) 220502 (2022), <https://doi.org/10.1063/5.0093654>.
- [107] P. G. Gowtham, D. Labanowski, and S. Salahuddin, Mechanical back-action of a spin-wave resonance in a magnetoelastic thin film on a surface acoustic wave, *Physical Review B* **94** (2016) 014436. <https://doi.org/10.1103/PhysRevB.94.014436>.
- [108] P. Rovillain, Jean-Yves Duquesne, L. Christienne, M. Eddrief, M. G. Pini, A. Rettori, S. Tacchi, and M. Marangolo, Impact of Spin-Wave Dispersion on Surface-Acoustic-Wave Velocity, *Physical Review Applied* **18** (2022) 064043. <https://doi.org/10.1103/PhysRevApplied.18.064043>.
- [109] M. Xu, K. Yamamoto, J. Puebla, K. Baumgaertl, B. Rana, K. Miura, H. Takahashi, D. Grundler, S. Maekawa, and Y. Otani, Nonreciprocal surface acoustic wave propagation via magneto-rotation coupling, *Science Advances* **6** (2020) eabb1724. <https://doi.org/10.1126/sciadv.abb1724>.
- [110] C. Cai, Xi-Han Zhou, W. Yu, and T. Yu, Acoustic frequency multiplication and pure second-harmonic generation of phonons by magnetic transducers, *Physical Review B* **107** (2023) L100410. <https://doi.org/10.1103/PhysRevB.107.L100410>.
- [111] A. Hernández-Mínguez, F. Macià, J. M. Hernández, J. Herfort, and P. V. Santos, Large Nonreciprocal Propagation of Surface Acoustic Waves in Epitaxial Ferromagnetic/Semiconductor Hybrid Structures, *Physical Review Applied* **13** (2020) 044018. <https://doi.org/10.1103/PhysRevApplied.13.044018>.
- [112] P. J. Shah, D. A. Bas, I. Lisenkov, A. Matyushov, N. X. Sun, and M. R. Page, Giant nonreciprocity of surface acoustic waves enabled by the magnetoelastic interaction, *Science Advances* **6** (2020) eabc5648. <https://doi.org/10.1126/sciadv.abc5648>.

-
- [113] H. Matsumoto, T. Kawada, M. Ishibashi, M. Kawaguchi and M. Hayashi, Large surface acoustic wave nonreciprocity in synthetic antiferromagnets, *Appl. Phys. Express* **15** (2022) 063003. <https://doi.org/10.35848/1882-0786/ac6da1>.
- [114] W. Edrington, U. Singh, M. A. Dominguez, J. R. Alexander, R. Nepal, and S. Adenwalla, SAW assisted domain wall motion in Co/Pt multilayers, *Applied Physics Letters* **112** (2018) 052402. <https://doi.org/10.1063/1.5000080>.
- [115] T. Yokouchi, S. Sugimoto, B. Rana, S. Seki, N. Ogawa, S. Kasai and Y. Otani, Creation of magnetic skyrmions by surface acoustic waves, *Nature Nanotechnology* **15** (2020) 361–366. <https://doi.org/10.1038/s41565-020-0661-1>.
- [116] R. Nepal, U. Güngördü, and A. A. Kovalev, Magnetic skyrmion bubble motion driven by surface acoustic waves, *Applied Physics Letters* **112** (2018) 112404. <https://doi.org/10.1063/1.5013620>.
- [117] R. Khoshlahni, S. Lepadatu, M. Kouhi, and M. Mohseni, Skyrmion dynamics induced by surface acoustic waves in antiferromagnetic systems, *Physical Review B* **107** (2023) 144421. <https://doi.org/10.1103/PhysRevB.107.144421>.
- [118] V. Sampath, N. D'Souza, D. Bhattacharya, G. M. Atkinson, S. Bandyopadhyay, and J. Atulasimha, Acoustic-Wave-Induced Magnetization Switching of Magnetostrictive Nanomagnets from Single-Domain to Nonvolatile Vortex States, *Nano Letters* **16** (9) (2016) 5681–5687. <https://doi.org/10.1021/acs.nanolett.6b02342>.
- [119] S. Davis, J. A. Borchers, B. B. Maranville, and S. Adenwalla, Fast strain wave induced magnetization changes in long cobalt bars: Domain motion versus coherent rotation, *Journal of Applied Physics* **117** (2015) 063904. <https://doi.org/10.1063/1.4907580>.
- [120] W. Li, B. Buford, A. Jander and P. Dhagat, Acoustically Assisted Magnetic Recording: A New Paradigm in Magnetic Data Storage, *IEEE Transactions on Magnetics* **50** (3) (2014) 37–40. <https://doi.org/10.1109/TMAG.2013.2285018>.

-
- [121] V. Schell, E. Spetzler, N. Wolff, L. Bumke, L. Kienle, J. McCord, E. Quandt and D. Meyners, Exchange biased surface acoustic wave magnetic field sensors, *Scientific Reports* **13** (2023) 8446. <https://doi.org/10.1038/s41598-023-35525-6>.
- [122] P. Pirro, V. I. Vasyuchka, A. A. Serga, and B. Hillebrands, Advances in coherent magnonics, *Nature Reviews Materials* **6** (2021) 1114–1135. <https://doi.org/10.1038/s41578-021-00332-w>.
- [123] W. Sauer, M. Streibl, T. H. Metzger, A. G. C. Haubrich, S. Manus, A. Wixforth, and J. Peis, X-ray imaging and diffraction from surface phonons on GaAs, *Applied Physics Letters* **75** (1999) 1709. <https://doi.org/10.1063/1.124797>.
- [124] R. Whatmore, P. Goddard, B. Tanner, G. Clark, Direct imaging of travelling Rayleigh waves by stroboscopic X-ray topography, *Nature* **299** (1982) 44–46. <https://doi.org/10.1038/299044A0>.
- [125] G. Eberharter and H. P. Feuerbaum, Scanning electron microscope observation of propagating acoustic waves in surface acoustic wave devices, *Applied Physics Letters* **37** (1980) 698–699. <https://doi.org/10.1063/1.92044>
- [126] L. Zheng, D. Wu, X. Wu, and K. Lai, Visualization of Surface-Acoustic-Wave Potential by Transmission-Mode Microwave Impedance Microscopy, *Physical Review Applied* **9** (2018) 061002. <https://doi.org/10.1103/PhysRevApplied.9.061002>.
- [127] M. Foerster, N. Statuto, B. Casals, A. Hernández-Mínguez, S. Finizio, A. Mandziak, L. Aballe, J. M. H. Ferràs, and F. Macià, Quantification of propagating and standing surface acoustic waves by stroboscopic X-ray photoemission electron microscopy, *Journal of Synchrotron Radiation* **26** (2019) 184–193. <https://doi.org/10.1107/S1600577518015370>.
- [128] M. Reimer, S. Niemeier, D. Laumann, C. Denz and S. Heusler, An acoustic teaching model illustrating the principles of dynamic mode magnetic force microscopy, *Nanotechnology Reviews* **6** (2017) 221–232. <https://doi.org/10.1515/ntrev-2016-0060>.

-
- [129] N. Träger, P. Gruszecki, F. Lisiecki, J. Förster, M. Weigand, S. Wintz, H. Stoll, H. Głowiński, P. Kuświk, M. Krawczyk, and J. Gräfe, Direct Imaging of High-Frequency Multimode Spin Wave Propagation in Cobalt-Iron Waveguides Using X-Ray Microscopy beyond 10 GHz, *Physica Status Solidi Rapid Research Letters* **14** (2020) 2000373. <https://doi.org/10.1002/pssr.202000373>.
- [130] <https://www.roditi.com/SingleCrystal/LiNbO3/liNBO3-Black-Wafers.html>.
- [131] B. Molas, L. Aballe, M. Foerster, A. Fontserè Recuenco, O. Matilla, J. Moldes, Synchrotron Master Frequency Reconstruction for Sub-Nanosecond Time-Resolved XMCD-PEEM Experiments, Proceedings of ICALEPCS2017, Spain (2017). <https://doi.org/10.18429/JACoW-ICALEPCS2017-THPHA084>.
- [132] R. Munoz Horta, G. Benedetti, D. Lanaia, J. Moldes, F. Perez, M. Pont, and L. Torino, "Single bunch bucket selection injection-modes in the Alba storage ring," Proceedings of the 8th Int. Particle Accelerator Conf., vol. IPAC2017, Denmark, 2017.
- [133] L. Aballea, M. Foerster, M. Cabrejo, J. Prat, P. Pittana, R. Sergo, M. Lucian, M. Barnaba, T. O. Menteş, A. Locatelli, Pulse picking in synchrotron-based XPEEM, *Ultramicroscopy* **202** (2019) 10–17. <https://doi.org/10.1016/j.ultramic.2019.03.011>.
- [134] B. A. Auld (1973). Acoustic Fields and Waves in Solids. New York: Wiley.
- [135] P. Wadley, V. Novák, R.P. Champion, C. Rinaldi, X. Martí, H. Reichlová, J. Železný, J. Gazquez, M. A. Roldan, M. Varela, D. Khalyavin, S. Langridge, D. Kriegner, F. Máca, J. Mašek, R. Bertacco, V. Holý, A. W. Rushforth, K. W. Edmonds, B. L. Gallagher, C. T. Foxon, J. Wunderlich, and T. Jungwirth, Tetragonal phase of epitaxial room-temperature antiferromagnet CuMnAs, *Nature Communications* **4** (2013) 2322. <https://doi.org/10.1038/ncomms3322>.
- [136] P. Wadley, V. Hills, M. R. Shahedkhah, K. W. Edmonds, R. P. Champion, V. Novák, B. Ouladdiaf, D. Khalyavin, S. Langridge, V. Saidl, P. Nemeč, A. W. Rushforth, B. L. Gallagher, S. S. Dhesi, F. Maccherozzi, J. Železný, and T.

Jungwirth, Antiferromagnetic structure in tetragonal CuMnAs thin films, *Scientific Reports* **5** (2015) 17079. <https://doi.org/10.1038/srep17079>.

LIST OF ARTICLES

Publications directly related with the thesis:

- **M. Waqas Khaliq**, Oliver Amin, Alberto Hernández-Mínguez, Marc Rovirola, Blai Casals, Khalid Omari, Sandra Ruiz-Gómez, Simone Finizio, Richard P. Campion, Kevin W. Edmonds, Vít Novák, Anna Mandziak, Lucía Aballe, Miguel Ángel Niño, Joan Manel Hernández, Peter Wadley, Ferran Macià, and Michael Foerster, Néel vector waves in antiferromagnetic CuMnAs excited by Surface Acoustic Waves. <https://doi.org/10.48550/arXiv.2309.08893v1>. (Accepted in Physical Review Materials)
- Marc Rovirola, **M. Waqas Khaliq**, Travis Gustafson, Fiona Sosa, Blai Casals, Joan Manel Hernández, Sandra Ruiz-Gómez, Miguel Ángel Niño, Lucía Aballe, Alberto Hernández-Mínguez, Michael Foerster, and Ferran Macià, Study of the magnetoelastic effect in nickel and cobalt thin films at GHz range using X-ray microscopy, *Physical Review Research* **6** (2024) 023285. <https://doi.org/10.1103/PhysRevResearch.6.023285>.
- **M. Waqas Khaliq**, José M. Álvarez, Antonio Camps, Nahikari González, José Ferrer, Ana Martínez-Carboneres, Jordi Prat, Sandra Ruiz-Gómez, Miguel Ángel Niño, Ferran Macià, Lucía Aballe, and Michael Foerster, GHz sample excitation at the ALBA-PEEM, *Ultramicroscopy* **250** (2023) 113757. <https://doi.org/10.1016/j.ultramic.2023.113757>.

-
- Marc Rovirola, **M. Waqas Khaliq**, Blai Casals, Michael Foerster, Miguel Ángel Niño, Lucía Aballe, Jens Herfort, Joan Manel Hernández, Ferran Macià, and Alberto Hernández-Mínguez, Resonant and Off-Resonant Magnetoacoustic Waves in Epitaxial Fe₃Si/GaAs Hybrid Structures, *Physical Review Applied* **20** (2023) 034052. <https://doi.org/10.1103/PhysRevApplied.20.034052>.
 - Bernhard von Boehn, Michael Foerster, Moritz von Boehn, Jordi Prat, Dr. Ferran Macià, Blai Casals, **M. Waqas Khaliq**, Alberto Hernández-Mínguez, Lucía Aballe, and Ronald Imbihl, On the Promotion of Catalytic Reactions by Surface Acoustic Waves, *Angewandte Chemie International Edition* **59** (2020) 20224–20229. <https://doi.org/10.1002/anie.202005883>.

Publications in related fields:

- Adrian Begué, **M. Waqas Khaliq**, Noelia Cotón, Alejandro Cabrera, Miguel Ángel Niño, Michael Foerster, and Rocio Ranchal, Reversible out-of-plane to in-plane magnetic transition by electrical and thermal cycling in Ni₉₀Fe₁₀/BaTiO₃(001). <https://doi.org/10.48550/arXiv.2401.13487>.
- Johannes H. Jensen, Anders Strømberg, Ida Breivik, Arthur Penty, Miguel Angel Niño, **M. Waqas Khaliq**, Michael Foerster, Gunnar Tufte, and Erik Folven, Clocked dynamics in artificial spin ice, *Nature Communications* **15** (2024) 964. <https://doi.org/10.1038/s41467-024-45319-7>.
- Sandra Ruiz-Gómez, Eva María Trapero, Claudia Fernández González, Adolfo del Campo, Cecilia Granados-Miralles, José Emilio Prieto, **M. Waqas Khaliq**, Miguel Ángel Niño, Michael Foerster, Lucía Aballe, and Juan de la Figuera, A platform for addressing individual magnetite islands grown epitaxially on Ru (0001) and manipulating their magnetic domains, *Crystal Growth and Design* **23** (2023) 5785–5791. <https://doi.org/10.1021/acs.cgd.3c00388>.
- Jorge Trasobares, Juan Carlos Martín-Romano, **M. Waqas Khaliq**, Sandra Ruiz-Gómez, Michael Foerster, Miguel Ángel Niño, Patricia Pedraz, Yannick. J. Dappe, Marina Calero de Ory, Julia García-Pérez, María Acebrón, Manuel Rodríguez Osorio, María Teresa Magaz, Alicia Gomez, Rodolfo Miranda and Daniel Granados, Hybrid molecular graphene transistor as an operando and

optoelectronic platform, *Nature Communications* **14** (2023) 1381. <https://doi.org/10.1038/s41467-023-36714-7>.

- Sandra Ruiz-Gómez, Rubén Guerrero, **M. Waqas Khaliq**, Claudia Fernández-González, Jordi Prat, Andrés Valera, Simone Finizio, Paolo Perna, Julio Camarero, Lucas Pérez, Lucía Aballe, and Michael Foerster, Direct X-Ray Detection of the Spin Hall Effect in CuBi, *Physical Review X* **12** (2022) 031032. <https://doi.org/10.1103/PhysRevX.12.031032>.

List of Figures

No.	Caption	Page
2.1	Schematic illustrating the arrangements of magnetic moments for ferromagnets and antiferromagnets materials in the absence of an external magnetic field	8
2.2	Breaking down of ferromagnetic material into magnetic domains .	12
2.3	Configuration of domain walls	12
2.4	Depiction of LL equation without damping	16
3.1	Schematic display of vital componenets of modern synchrotron source	21
3.2	Schematic illustration of storage ring depicting main components like bending magnets, undulators, wigglers, quadrupoles, and RF cavity	23
3.3	The main difference between wigglers and undulators is only the excursion size which electrons are forced to experience from straight path	23
3.4	The Spectrum of Electromagnetic radiations	25
3.5	Depiction of polarization of synchrotron radiations with respect to viewer's frame of reference relative to the electron's orbital plane	26
3.6	Type and process of emitted electrons by X-ray absorption in PEEM	28
3.7	Simplified schematic demonstration of a LEEM setup	29
3.8	Schematic illustration of the XPEEM	30
3.9	Various operation modes of LEEM-PEEM microscope with respective optical configurations	32
3.10	Side- and top view of the XPEEM experimental station	36
3.11	Types of sample holder available at the XPEEM beamline	38
3.12	Display of modified parts to be employed for higher frequency signals	40
3.13	In-plane/out-of-plane sample holder with its characterization	41

4.1	Schematic depiction with regions of compressive and tensile strain during propagation of a SAW through piezoelectric material	46
4.2	IDTs with their characterizations	50
4.3	Sample mounting in sample holder and electrostatic lens effect	52
4.4	Illustration of the scheme to apply electrical excitation (SAW) to the samples in the XPEEM synchronized with x-rays beam	54
4.5	XPEEM image of SAW with electrical amplitude	55
4.6	Schematic illustration of the in-plane strain induced modulation in the LiNbO ₃ caused by the SAW	56
5.1	XRD and XMLD plots of CuMnAs on GaAs	59
5.2	Néel vector wave (spin axis rotation wave) in CuMnAs at different temperatures	60
5.3	Efficiency of the Néel vector wave excitation in CuMnAs as a function of temperature in comparison with all data at 500 MHz SAW	61
5.4	Connection scheme between the sample holder and the high frequency cable inside the XPEEM chamber	62
5.5	Characterization of HF setup in comparison to old setup	63
5.6	Spatial resolution	64
5.7	Angular measurements of transmission signals for SAW attenuation in Ni and Co at 1 GHz frequency	65
5.8	XMCD images and MAWs amplitudes of Ni at 1 and 3 GHz and Co at 1 GHz	66
5.9	Simulations for determining magnetoelastic constant values for Ni and Co at various angles	68

LIST OF SYMBOLS AND ABBREVIATIONS

Symbols

SAW	Surface acoustic waves
XPEEM	X-ray photoemission electron microscope
XMCD	X-ray magnetic circular dichroism
μ_l	Angular magnetic moment
γ_e	Gyromagnetic ratio of an electron
\hbar	Angular momentum
μ_s	Spin magnetic moment
g_e	Gyromagnetic splitting factor of an electron
T_C	Curie temperature
T_N	Néel temperature
α	Gilbert damping parameter
H_{eff}	Effective magnetic field
LLG	Landau-Lifshitz-Gilbert
FMR	Ferromagnetic resonance
K_{ME}	Magnetoelastic anisotropy

M_s	Saturation magnetization
XPS	X-ray photoemission spectroscopy
XAS	X-ray absorption spectroscopy
LINAC	linear accelerator
RF	Radio frequency
MeV	Million/mega electron volt
GeV	Giga electron volt
IDs	Insertion devices
γ	Lorentz factor
Φ	Work function
E_b	Binding energy
LEEM	Low energy electron microscope
LEED	Low energy electron diffraction
XANES	X-ray absorption near edge structure
UV	Ultraviolet
BFP	Back focal plane
AC	Aberration correction
MEM	Mirror electron microscope
XMLD	X-ray magnetic linear dichroism
σ^+	Circular right polarization
σ^-	Circular left polarization
$\hat{\mathbf{k}}$	Beam projection vector
$\mu_{ }$	Parallel polarization
μ_{\perp}	Perpendicular polarization
\mathbf{E}	Electric field vector
V_{start}	Bias voltage
ARPES	Angular resolved photoemission spectroscopy
SPELEEM	Spectroscopic photoemission and low energy electron microscopy
NAPP	Near ambient pressure photoemission
KB	Kirkpatrick-Baez
W/Re	Tungsten/Rhenium

PCB	Printed circuit board
SMP	Sub-miniature push-on
UHV	Ultrahigh vacuum
STT	Spin transfer torque
SOT	Spin orbit torque
AMR	Anisotropic magnetoresistance
MOKE	Magneto-Optical Kerr Effect
IDT	interdigital transducers
S_{11}	Reflected electrical signal
S_{12}	Transmitted electrical signal
SMA	Sub-miniature version A
PEEK	Polyether ether keton
a-FMR	Acoustic ferromagnetic resonance
ME	Magnetoelastic
MAW	Magnetoacoustic waves